UNIVERSITÀ DEGLI STUDI
DI MODENA E REGGIO EMILIA

Dottorato di ricerca in
INGEGNERIA INDUSTRIALE E DEL TERRITORIO
"ENZO FERRARI"

Ciclo XXXV

Introduction of Additive Manufacturing Laser Powder Bed Fusion technology for automotive components: from process investigation to boost industrial application

Candidato: CAMILLA CAPPELLETTI

Relatore (Tutor): Prof. ELENA BASSOLI

Coordinatore del Corso di Dottorato: Prof.
ALBERTO MUSCIO

Acknowledgements

First of all, I would like to express my gratitude to my supervisor, Prof. Elena Bassoli who gave me this great opportunity and supported me in the key moments of this PhD.

A huge acknowledgement goes to my colleagues in Ferrari S.p.A. for the constant collaboration that led to the writing of this thesis. Among these I would like to thank Ing. Fabrizio Fabbri who accompanied me in these three years of study and research and from whom I had the opportunity to learn and grow from a technical point of view. Thanks also to Ulisse Millefanti, colleague and friend with whom I had the pleasure to work and compare myself in a daily and lively exchange of knowledge and opinions.

A special thanks also to my university colleagues, Emanuele Tognoli and Silvio De Fanti, for the precious advice and help.

My biggest gratitude goes to my family, “fuel” all along this route. Thanks for accompanying me towards every achievement, helping me overcome the various difficulties met. If, today, looking back I could say to be proud of my path I owe it to them.

Last but not least, thank you Matteo, for always being by my side.

ABSTRACT

Additive Manufacturing (AM) processes as Laser-powder Bed Fusion (L-PBF) are gaining increasing attention in industries thanks to the possibility of producing customizable products with complex geometries not otherwise feasible with traditional technologies.

L-PBF exploits the main principle of AM, adding material instead of removing it, to build components layer by layer. This gives the freedom to completely re-think parts in terms of functionality or weight saving. Moreover, it becomes possible to design components in prototyping phase at lower cost and in less time, since no production equipment has to be designed or manufactured, as is the case with casting, for example.

These are some of the reasons behind the growing interest for AM in sectors as the automotive one.

This thesis was developed in Ferrari S.p.A where I had the opportunity to witness the steps made for L-PBF introduction inside the company, with the aim of prototypes as well as production. The alloy chosen was AlSi10Mg, one of the most common aluminum alloys used in Additive Manufacturing since it represents a good compromise between mechanical characteristic and material cost.

This study deals with the overall evaluation of the process from several points of view. The effects of building direction and surface condition on tensile and fatigue properties were evaluated with an in-depth analysis on defects influence. Moreover, various heat treatments (HT) were studied in order to analyze the alloy behavior and to define a HT portfolio that could cover different design requests.

Obviously, being applied to a productive company, performance has to be accompanied by productivity. Hence, a large campaign was set up for process parameters optimization to reach the best compromise between mechanical properties and production time.

Another aspect considered was the component working environment, since it is one of the main factors taken into account by designers during material and product validation. Therefore, an extensive study on corrosion resistance of AlSi10Mg printed parts was carried out. Several HT and surface treatment conditions were considered to evaluate the behavior in different fluids, in comparison to the one of A356 aluminum cast alloy.

The aim of all this work was to study thoroughly L-PBF applied to AlSi10Mg in order to provide production solutions that could satisfy different applications. Thanks to the process knowledge and to the familiarity acquired, it was possible to draft technical specifications for both process and product controls. At the same time were defined the steps made for design and production feasibility in order to build up small batch production from a prototypal one.

ABSTRACT (Italiano)

I processi sotto il nome di Additive Manufacturing (AM), come il Laser Powder Bed Fusion(L-PBF), stanno acquisendo crescente interesse da parte di industrie di diversi settori grazie alla possibilità di produrre pezzi personalizzabili e di geometrie complesse, irrealizzabili con le tecnologie tradizionali.

La tecnologia L-PBF sfrutta il principio alla base dell'AM, ovvero la produzione di parti aggiungendo materiale invece che rimuoverlo, per costruire componenti strato su strato. Ciò offre la libertà di ri-progettare completamente i vari prodotti da un punto di vista strettamente funzionale, con l'obiettivo, ad esempio, di una diminuzione di peso. Inoltre, offre vantaggi in fase prototipale per la riduzione di tempi e costi legati a modifiche di progetti, dal momento che non serve produrre o fornirsi di attrezzature specifiche come ad esempio accade in tecnologie tradizionali come quelle di fonderia.

Questi sono alcuni dei motivi per l'aumento di interesse nel mondo dell'AM da parte di settori come quello automotive.

Questa tesi è stata svolta in Ferrari S.p.A, dove ho avuto l'opportunità di osservare gli step svolti per l'introduzione e della tecnologia L-PBF, con l'obiettivo di una produzione non solo prototipale. La lega scelta è l'AlSi10Mg, una delle leghe di alluminio più usate nell'AM grazie al rapporto tra prezzo e caratteristiche meccaniche ottenibili.

Viene riportata l'analisi completa del processo svolta considerando diversi aspetti. Sono stati valutati gli effetti della direzione di stampa e della condizione superficiale sulle proprietà statiche e dinamiche, con un approfondimento sull'influenza dei difetti di stampa. Inoltre sono stati studiati e applicati diversi trattamenti termici per evidenziare gli effetti sul materiale e definire quindi un portfolio di trattamenti che potessero rispondere a diverse richieste da parte della progettazione.

L'utilizzo di una nuova tecnologia in un'azienda produttiva, a prescindere dal settore, implica la necessità di ottenere non solo performance, ma anche produttività. Per questo motivo è stato impostato un importante studio per l'ottimizzazione dei parametri di stampa, con il fine di raggiungere il migliore compromesso tra proprietà meccaniche e riduzione dei tempi di produzione.

Inoltre, in fase di progetto e di delibera, l'ambiente di applicazione del componente rappresenta uno dei principali fattori da considerare per la validazione del materiale e del prodotto stesso. Pertanto, è stata svolta un'estesa campagna di prove di corrosione per stabilire il comportamento di provini stampati in AlSi10Mg con diverse condizioni di trattamenti termici e superficiali a contatto con vari fluidi, a confronto con provini da fusione in lega di alluminio A356.

L'obiettivo di tutto questo lavoro preliminare è stato quello di studiare approfonditamente il processo L-PBF applicato alla lega AlSi10Mg, in modo da poter fornire soluzioni produttive che potessero rispondere a diverse applicazioni. Grazie alla conoscenza della tecnologia e alla familiarità acquisita, si è giunti alla stesura di adeguate specifiche tecniche per il controllo del processo e del prodotto e alla definizione degli step necessari per passare da una fase prototipale a quella produttiva.

CONTENTS

LIST OF FIGURES

LIST OF TABLES

CHAPTER 1
INTRODUCTION

1.1 What is Additive Manufacturing?

Additive Manufacturing (AM), according to the ASTM definition, "*is a process of joining materials to make objects from 3D model data, usually layer upon layer, as opposed to subtractive manufacturing technologies*" [1].

Additive manufacturing differs from any other traditional technology starting from its basic principal. In fact, while processes as turning or milling are based on the subtraction of material from a wrought piece, in AM the material is added layer by layer until the completion of the desired built part.

This of course is generally accompanied by a reduction of the material waste since the quantity of material used is almost just the one needed [2], [3].

The development of this technology started in the early '80s, when it was better known as Rapid Prototyping (RP). The name itself defines the purpose of the process, which is the rapid production of parts prototypes that will be later produced with the use of traditional technologies.

Later on, the term Rapid Prototyping has been abandoned and substituted by Additive Manufacturing. This, to better underline the not subtractive nature of the technology and to expand its aim not only to the building of prototypes but also to the production of functional parts. Actually, the first AM technology invented in the 80s was stereolitography (SL), commercialized by 3D system in 1987 [4], paving the way for the introduction of all the other AM technologies in the following years. From that moment on, the AM technologies and applications gained a fast growing interest in industries investments. The AM market is growing at a Compound Actual Growth Rate (CAGR) of 14.4% (2020) until the achievement of a $55 billion market by 2029, as foreseen in 2020 SmarTech's report [5], in line with the goal of representing the 2% global manufacturing industry by 2030. The increasing interest in AM application in various industrial sectors as the automotive one is also promoted by the advantages listed in the following paragraph.

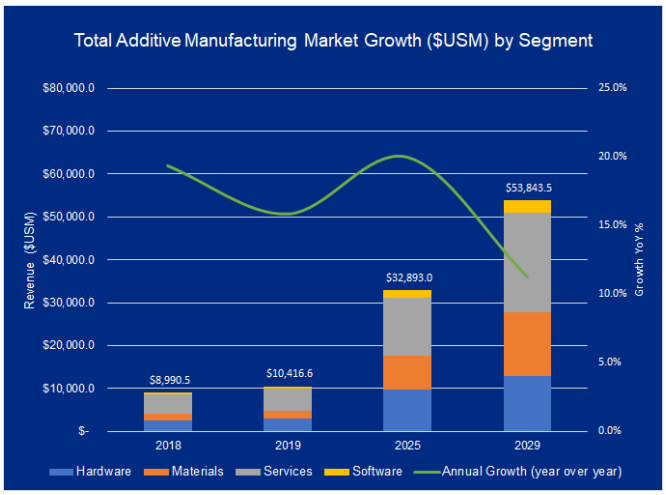

***Figure 1**: Total Additive Manufacturing market growth ($USM) by Segment* [5]

1.2 Benefits of AM

Adding material instead of removing it, gives freedom in designing complex parts that would not ever be produced by any other traditional technology [6]. This has been an incentive to the industries for investing in this new technology, for the possibility to re-design components in complex shapes for a better part functionality with advantages as weight saving.

Regarding this, the cost of a part produced by AM is affected by the material required and, as a consequence, the time necessary to consolidate it. Therefore, it is preferred designing part with a high void/solid ratio [7]. The light-weighting becomes a AM design principal, since light-weighted parts are here cheaper, in contrast to the traditional technologies where costs are associated to each added feature in terms of material waste and time production. This is one of the reasons why AM has taken hold rapidly in sectors as aerospace and automotive.

On the other side, the cost of a AM part is fixed, while the one produced by traditional technologies decreases as the production batch increases. There is a breakeven point above which the traditional technologies are still preferable in terms of costs. Figure 2 [8] shows the breakeven point between a traditional manufacturing (TM) as High Pressure Die Casting in comparison to AM SLS technology, pointing out how from a certain production batch dimension, TM is still more competitive. Actually, due to the limited build volume and to the general high production time of AM, this technology is generally suitable for small batch productions, even though progresses have been made in this field by industries to increase the productivity.

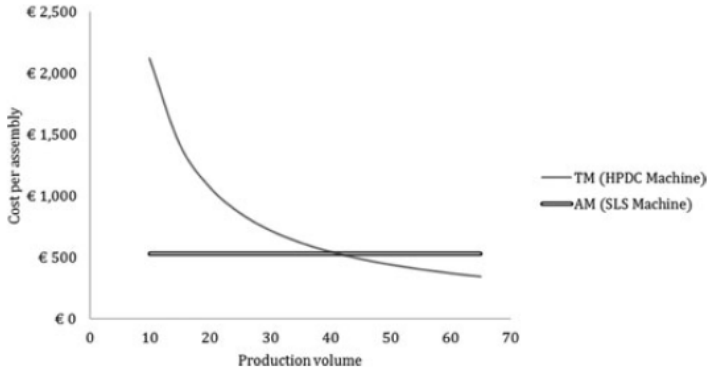

***Figure 2**: The graph shows the breakeven point between AM and traditinal technologies* [8] .

However, other aspects must be taken in consideration when comparing these technologies. For example, AM is usually exploited to produce a single complex part instead of several different pieces produced by traditional technologies, saving costs both in terms of material and assembly time. In addition, little changes in the design can be applied without any added cost to the production, as happens with traditional technologies in which any modification is linked to the use of different tools or equipment.

All these advantageous aspects flow into the main beneficial characteristic of AM, the design freedom. Analyzing the possibility to build complex parts, the costs per pieces related to the eventual traditional production increases with the growth of the complexity level of the design, while those corresponding to AM production stays almost unchanged, as shown in Fig 3.

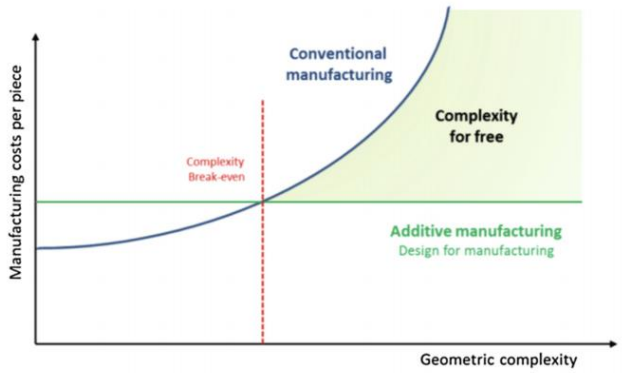

***Figure 3**: The graph shows the complexity breakeven point between AM and conventional technologies. Over this breakeven point the part complexity does not affect the part cost* [9].

Above the complexity breakeven point shown in Fig. 3 the gain is what is so called "complexity for free", that means that any increase of the geometric complexity of the AM part isn't accompanied by a rise of the built part cost.

Here below some of the main advantages and disadvantages of AM are listed [10].

Advantages

• Complexity is free	The part costs are note dependent on the geometry complexity of the part.
• Variety is free	Changing of the design doesn't affect the parts costs under the same conditions in terms of part volume.
• Design freedom	AM gives the possibility to design component with complex geometries that could never be manufactured by traditional technologies.
• Minimized waste	Thanks to the additive nature of the process the material wasted is minimized.
• Little lead time	Little time among design, production and testing of the printed part.
• Environmentally friendly	As this technology reduces the amount of material wastage used this process is inherently environmentally friendly.
• No need for assembly	AM offers the possibility to build complex single parts instead of several different pieces, thus reducing the assembly costs.

Disadvantages

• Low productivity	Due to the build rates and to the limited volume of the building chamber, the productivity is low. Hence, AM is mainly suitable for small batch production.
• High investment costs	The first investment to buy the AM machine is still high.

• Limited part size	Due to the limited volume of the building chamber the part size is constrained.
• No industrial normative or standards	Being an almost new technology, industries are facing problems related to the lack of general standards.
• Little material choice	Nowadays still few materials have been designed for AM, even though many research are focusing on this matter.

***Table 1**: Advantages and disadvantages of AM technologies*

Table 1 summarizes some of the advantages behind the increasing interest in AM world by industries as the automotive ones, together with the limitation and problems to face during AM introduction inside a productive company.

1.3 Aim of the thesis

This thesis was developed in close collaboration with Ferrari S.p.A. and represents a sort of reportage of the steps taken for introducing Additive Manufacturing applied to AlSi10Mg aluminum alloy in the company.

Being a not-conventional technology, the process was at first deeply studied in order to acquire the confidence needed for production phase with a glance of all those topics that could be required in an eventual AM component design. Therefore, aspects as alloy characterization, fatigue behavior in different conditions as well as surface treatments application were evaluated. Moreover, thinking of producing components that could be affected by their working environment, alloy corrosion resistance was thoroughly studied in respect of different corrosive fluids that could come into game during vehicle life.

Among the driving factors of AM application in automotive one of the leading is for sure the possibility to build component with complex geometries not otherwise feasible with traditional technologies. This advantage leads to the complete parts re-design with different purposes as weight saving and functionality integration.

On the other hand, talking about a productive company, these advantages are exploitable as long as they are competitive also from an economic point of view. Here came the need of finding the optimal process set up that could boost productivity for part cost reduction.

At the end, all these different studies were aimed for defining different process windows to be given to the design department, paving the way for AM applicability inside the company.

In parallel, thanks to the knowledge acquired during this work, the lack in universal standards (one of the drawbacks listed in table 1) was filled by defining internal specification for both process and product control.

1.4 Organization of the thesis

In detail, the dissertation is organized as follows:

- *CHAPTER 2: LITERATURE REVIEW*
  In this chapter, AM process is described from a technical point of view thanks to what reported in scientific literature. Great attention was put in particular to Laser-Powder Bed Fusion (L-PBF) technology applied to AlSi10Mg alloy, since it represents the process used in this thesis.

- *CHAPTER 3: MATERIALS AND METHODS*
  In this chapter, materials and methods used during the following experimental works are described.

- *CHAPTER 4: MECHANICAL CHARACTERIZATION OF AM AlSi10Mg PARTS*
  In this chapter, mechanical characterization of AlSi10Mg alloy is reported. In detail, heat treatments evaluation was carried out on stress relieved (SR) and solution heat treated followed by water quenching and artificial aging (T6) AM specimens. The study continues with fatigue behaviour investigation thanks to a wide rotating bending fatigue test campaign. Different conditions were here evaluated as, surface condition (machined and not machined specimens), sample orientation and height in the building chamber.

- *CHAPTER 5: PROCESS PARAMETERS OPTIMIZATION FOR MECHANICAL CHARACTERISTICS AND PRODUCTIVITY IMPROVEMENT*
  In this chapter, a wide Design of Experiment (DOE) was set up to find the optimal process parameters that could guarantee high mechanical properties and low building time. In this regard, hatch distance and scanning speed were varied, keeping fixed laser power and layer thickness. Parameters combinations were evaluated by tensile tests, density measurements and internal defect investigation. The three most promising combinations were further analysed by rotating bending fatigue tests on machined specimens.

- *CHAPTER 6: SURFACE TREATMENTS INVESTIGATION*
  In this chapter, different surface treatment, categorized in this work in “mechanical” and “chemical” were evaluated with morphological analysis and roughness measurements. Among the mechanical surface treatments, we investigate barrel stone machining and shot peening with B60 ceramic beads and S110 steel shots. Among the chemical ones, chemical milling, DryLyte®, Hirtisation® and green etching® were considered. Then, some of these surface treatments were further analysed with rotating bending fatigue tests to evaluate the influence of surface condition on fatigue resistance.

- *CHAPTER 7: CORROSION BEHAVIOUR OF AM AlSi10Mg PARTS COMPARED TO OTHER ALUMINIUM ALLOYS*

  In this chapter, corrosion resistance of AlSi10Mg samples in different heat treatment and surface conditions was evaluated in comparison to aluminium alloys normally used in traditional technologies (A356 T6, EN AW1050 H24, EN AW3003 H111, EN AW6082 T6, EN AW5083 O). Corrosion behaviour was numerically estimated by calculating the corrosion rate according to ASTM G31-72 [11] after parts immersion in different fluids

as salty water, oil for active suspensions, oil 5W40, automotive gasoline (E10), glycol (50%). Some of these tests were subsequently repeated at high temperature to better simulate the component working environment inside the vehicle.

- *CHAPTER 8: FROM PROCESS INVESTIGATION TO INDUSTRIAL APPLICATION*

  In this chapter, it is briefly described how the in-depth process study led to the proper confidence that allowed the definition of internal standards for process and product control.

CHAPTER 2
LITERATURE REVIEW

2.1 AM Process

AM, as opposed to traditional technologies, is based on the adding of material instead of the removal. The steps to follow for the design are listed in Table 2.

Pre – printing	➢ CAD design ➢ File format ➢ Machine input file
Printing	➢ Machine setup ➢ Building
Post – printing	➢ Remove ➢ Post processing ➢ Application

Table 2: *AM process steps*

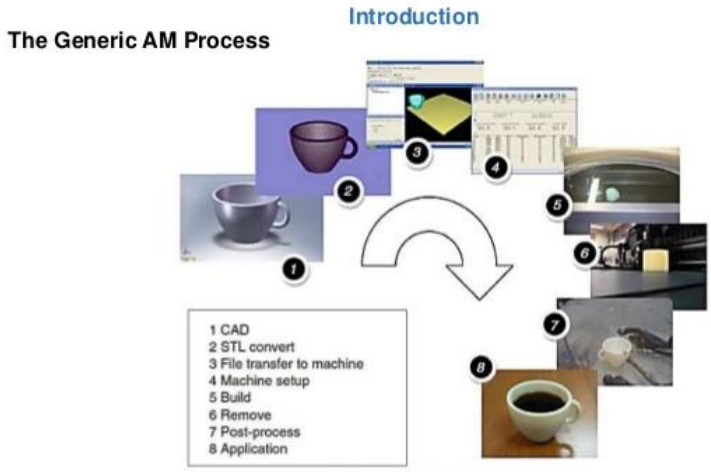

Figure 4*: Generic process steps, from CAD to the built part* [12]

Pre-printing

The starting point for the part design is the same of any other technology, a CAD model where the geometry of the final part is defined.

The model is then converted to an STL file format in order to be readable by the AM machine. This file is a representation of the original CAD model, in which the external surface of the part is approximated to several triangles, hence introducing a first set of error.

The STL file is then transferred to the AM software, where the correct position and orientation of the piece to build can be chosen in order to optimize the process. Here, the STL file is read by the AM machine software that, depending on the layer thickness chosen, "slices" the geometry. If the lateral surface of the part is not perfectly parallel to the growth direction, the staircase effect takes

place, that is a direct consequence to the deviation between the original external surface and that one effectively produced.

Here, this other approximation error is strictly linked to the discrete nature of this technology. To minimize the staircase effect thinner layer thickness must be imposed at the expense of a longer production time. Therefore, depending on the scope of the part to be built, a compromise between printing quality and production time has to be found.

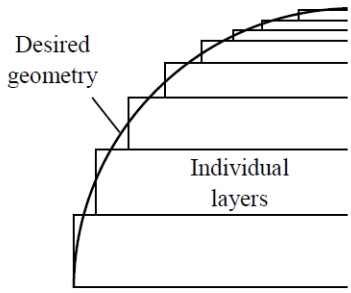

Figure 5: *Staircase effect in AM due to the layer-by-layer production* [13]

Printing

Before starting the building process the AM machine must be setup. This phase consists in the material preparation, in terms of quantity, for the building of the part and in the machine parameter setting. Then, the printing phase, which is the core of the process, can start. In Laser-Powder Bed Fusion it consists in the repetition of computer-controlled actions as the spreading of the powder on the building platform by a recoater and the application of a heat source for the selective melting of the powder itself. This process continues until the part is completed, unless errors occur during the printing, as for example insufficient material in the storage tank.

Post Processing

Once the building phase is ended, the part has to be cleaned from the remaining powder and removed from the building plate, together with the support material, if there is any. Then, depending on the required characteristics of the built part, the piece can undergo heat treatments or surface finishing.

Finally, the part is ready for use. AM finds application in different fields thanks to the possibility to use several materials and to build complex and customized geometries. Nevertheless, still nowadays it is mainly used in the prototyping phase to take full advantage from the small batch production, in which other traditional technologies cannot compete in terms of cost and production time.

2.2 AM Technologies

The AM technologies differ for the materials used and for the process basic principles. Hence, in 2010, the American Society for Testing and Materials (ASTM) group [14] formulated a set of standards that classify the range of Additive Manufacturing processes into 7 categories:

1) **Vat Photopolymerization**

   Photopolymerization occurs when a photopolymer resin is exposed to the light of a specific wavelength and undergoes a chemical reaction to become solid.
   The technologies developed are:
   - Stereolithography (SLA) in which a single laser point scans the desired geometry on a build plate submerged into a liquid photopolymer resin. The part is built layer by layer and then cured with UV lights to increase mechanical properties.
   - Direct Light Processing (DLP), which is similar to SLA with the difference that it uses a digital light projector screen to flash a single image of each layer all at once.
   - Continuous DLP (CDLP), which is equal to DLP but with a continuous movement of the building plate along Z direction to speed up the process.

2) **Material Extrusion**

   AM process in which material is selectively dispensed through a nozzle, building up the part layer by layer
   - Fused Deposition Modeling (FDM). A thermoplastic material is extruded through a heated nozzle and deposited to build the part layer by layer.

3) **Material Jetting**

   AM process in which droplets of material are selectively deposited to build up the part. It is commonly compared to 2D ink jetting process. The materials used can be photopolymers, metals or wax that are cured when exposed to UV light or to high temperatures.
   - Material Jetting (MJ), which dispenses photopolymer material in droplets from nozzles in a print head to build a part layer-by-layer. As the droplets are deposited to the build platform they are cured and solidified using UV light.
   - Nano particle jetting (NPJ), in which droplets of metal nanoparticles contained in a liquid solution are jetted onto the build tray in thin layers. The chamber high temperature leads to the liquid evaporation leaving the built metal part.
   - Drop-On-Demand (DOD). According to this process the material jetting printers have 2 print jets: one to deposit the build and another for dissolvable support material.

4) **Binder Jetting**

   AM process in which a binding agent is dispensed onto a powder bed, building the part layer by layer.

5) **Powder Bed Fusion**

   AM process in which a thermal energy selectively fuses powder material that could be plastic, metallic or ceramic.
   - Selective Laser Sintering (SLS), in which Laser energy input selectively sinters the powder material spread layer upon layer on the building plate.

- Selective Laser Melting (SLM), which is similar to SLS except for the way the powder is joined. In fact, here the temperatures reach the melting point, so the material is melted and not sintered. Moreover, here the materials are generally metals.
- Electron Beam Melting (EBM). This process is similar to SLM with the difference that the thermal energy here is represented by an electron beam focused on the powder material to selectively melting it.
- Multi Jet Fusion (MJF) is essentially a combination of the SLS and Material Jetting technologies. A carriage with nozzles deposits a fusing agent on the desired area to be printed. A high-power IR energy source then passes over the build bed and sinters the areas where the fusing agent was dispensed, while leaving the rest of the powder untouched.

6) Direct Energy Deposition

AM process in which focused thermal energy fuses material by melting it while it is being deposited.

- Laser Engineered Net Shape (LENS), according to which a deposition head consisting of a laser, a powder dispensing nozzle and an inert gas tubing, melts the powder while it is being deposited.
- Electron Beam Additive Manufacture (EBAM), where the metal in form of powder or wire is welded by an electron beam as heat source.

7) Sheet Lamination

AM process in which sheets of material are joined to form an object.

- Laminated Object Manufacturing (LOM).

2.3 SLM Process

The SLM process, together with electron beam melting EBM and selective laser sintering SLS, belongs to the family of powder bed fusion technologies. For these technologies the operating steps, as represented in Figure 6, are the same.

The recoater blade spreads a layer of powder on the building plate that can be pre heated in order to minimize the thermal residual stresses. Then, an energy source interacts with the powder bed to selectively fuse it. In particular, EBM uses a high energy focused electron beam to fuse the material, for this reason the process must take place in a low partial pressure vacuum environment. On the other hand, SLM and SLS use a LASER as heat energy source.

The main difference between the latter technologies is the way the powder and layer are fused together. As mentioned above, SLS, as suggested by the acronym itself, sinter the powder, so at a temperature below the melting one of the alloys considered. On the other hand, in SLM process, the LASER selectively heats up the metal powder over the melting temperature to fully melt the material.

The entire heat affected region is melted to a depth greater than the one of a single layer. In this way the bonding between consecutive layer is granted [15], leading to the building of a high density part.

After completing the fusion of a layer, the building platform is lowered of one layer and the process starts again from the spreading of the powder [12]. Hence, the part locally undergoes repetitive heating and cooling cycles, with extremely high solidification rates around 10^3-10^7 K/s [15].

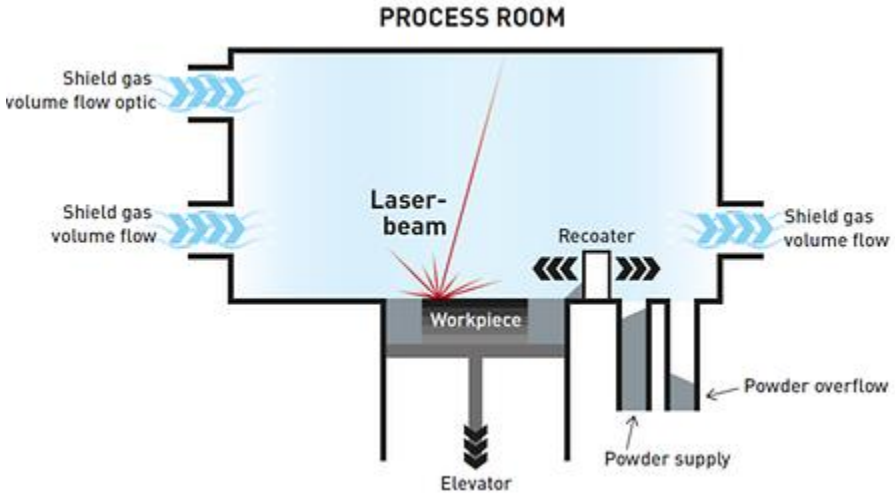

Figure 6: *Scheme of the building chamber in L-PBF process*

2.4 Materials for L-PBF

As mentioned above, SLM is a process that leads to the melting of metal powder. Regarding this, L-PBF owes its industrial diffusion mainly thanks to the possibility of building parts in several materials depending on the final application. In industries the principal materials used are aluminium alloys [16]–[21], nickel alloys [22], [23], steels [24], and titanium alloys [25]with some copper alloys [26], magnesium alloys [27].

Many studies have been carried out for designing specific metal alloy for AM. As reported in [28], some of the strategies employed to optimize the metal alloys for SLM can be summarized as following:

- Increase fluidity and weldability to avoid problems as solidifications cracking, balling, hot tearing
- Reduce the solidification range to reduce hot tearing
- Add of alloy elements to satisfy certain requirements or to form low eutectics, thereby minimizing the crack sensibility
- Extend the solid solution strengthening

Nevertheless today, the attention has been focused mainly on pre-existing alloys typically used in industrial traditional technologies, as for example casting or welding. That is why the principal features required for an AM alloy are weldability and fluidity, even though the process is different and more complicated than casting or welding. First, the solidification rates are much higher than those in traditional technologies. Then, differences can be found also in the starting material condition since in AM the raw material is metallic powder while generally in casting or welding is in form of ingots or wires. Hence, this, together with the repetitive re-melting and solidification of the layers, change the physics of heat transfer to the bulk material and, as a consequence, the microstructure, as it is deeply discussed in the following paragraphs.
Therefore, nowadays it is still difficult to adjust a strategy for AM alloy design for a proper compromise between chemical/physical characteristics requirements and process feasibility.

As stated before, among the materials typically used in SLM there are the Aluminium alloys. In general they are used in many industrial applications (as aerospace, automotive etc.), since they offer a compromise between lightening and strength[29]–[31]. On this regard, strengthening is reached during SLM process thanks to high cooling rates that lead to a microstructural refinement [15], [32], [33].

The most frequently investigated Al alloys for SLM are the Al-Si alloys [19] and, in particular, the eutectic ones, that's to say Al-Si alloys with Silicon in the range of 11-13wt%, or the near eutectic alloys as AlSi10Mg, as the one studied in this thesis. The presence of Si facilitates the weldability, while the addition of elements such as Mg or Cu plays an important role in age hardening thanks to the precipitation of secondary phases [18], [34], as better explained in the following paragraphs.

However, some Al alloys properties bring with them problems still difficult to solve when it comes to the application to SLM technology. First, Al reflectivity reaches 91%, while its laser absorptivity is low in the wavelength range of 1,06μm [35], which is typical of fibre lasers generally used in SLM technology. Hence, higher laser power is needed to guarantee the correct melting of the powder and to avoid problem related to low energy absorption as porosity or cracks [36]. Moreover, Aluminium oxidizes very easily, which could lead to the occurrence of

metallurgical defects that could be detrimental to the mechanical characteristic of the built part [19].

2.5 Powders

The metallic powder represents the raw material in SLM process. Generally, the dimension range of the metallic powder used in AM is 10-120µm to guarantee a theoretical homogeneous spreading of a thin powder layer on the building plate for each printing step. Many studies reported how the characteristics of the powder influence the quality of the printed part [37], [38]. Hence, a correct powder analysis is needed, to ensure that the starting material characteristics fit in a specific acceptance range.

Metallic powder can be produced in different ways. The most common is *gas atomization* where an elemental feedstock is melted under an air or inert gas blanket, or under vacuum. Then, the gas in the chamber forces the molten alloy through a nozzle. The thin flow of the melted alloy divides in small droplets by high pressure of inert gas and solidifies during the flight in atomizing chamber [39], [40]. The gas atomized powder is almost composed by spherical particles, even though "satellites" can be present, especially during the production of thin powders [41]. Satellites are small particles attached to bigger ones. Their formation could be caused by the gas recirculation inside the atomizing chamber. This lifts the smaller particles that collide with the still melted bigger ones.

Water atomization exploits a high pressure of water steam to divide the melt flow. It is mainly used for the less reactive material as for example steel[40], [42]. Moreover, due to the higher cooling rates, the shape of the particles is not perfectly spherical, but more irregular than the powder atomized by gas. Another disadvantage is the limitation of purity especially for those metal alloys that oxides very easily.

Plasma atomization is used for production of near perfect spherical powders [43] with high melting point as titanium, zirconium, tantalum etc. The raw material is a wire that is insert into a plasma torch that discretizes the wire into spherical droplets that solidify in flight [40].

As reported in a study [44], the powder properties can be classified in:

- Chemical and physical properties
- Bulk powder properties, so how the powder behaves as a whole
- Powder in-process performance, so how the powder behaves under some process conditions.

The *chemical* of the powder can be easily examined through an EDX micro-analysis.

Particle size distribution (PSD), one of the most important properties, is generally defined with the sizes D10, D50, and D90. These represent the volumes in terms of 10, 50 and 90% of particle with a size smaller than a specific value. A wide distribution means a powder batch that includes particles with different size. This implies that in the powder spreading by the recoater blade, the smaller particles fill the empty spaces left by the bigger ones. Hence a good powder packing is reached. On the other hand, for a good flow of the powder a narrower PSD is needed. It is generally measured with laser diffraction methods [44].

Among the bulk properties, the *flowability* is the most studied and discussed. It plays a fundamental role during the spreading of the powder by the recaoter blade on the building plate,

influencing the powder bed density and, as a consequence the quality of the printed part [45]. It is affected by particle shape and size, particles surface morphology and by humidity.

Regarding the shape, in general spherical powder guarantees a higher flowability and a greater packing density. While, concerning the size, small particles show lower flowability since the cohesion strength between particles increases with the decrease of the particle size, hence it will be more difficult the spreading of a homogenous powder layer. Humidity of powder makes effect of sticking particles together and leads to worse results in flowability measurement [46], so it is strongly recommended to dry the powder before using it.

Other important aspects in powder characterization are its density and the corresponding relationship with the flowability. In this regard, a distinction should be made between *powder apparent density* and *tap density*. While the former is the density measured in a cylinder with a known volume, in general 100mL, without any compaction, the latter represents the density of a compacted batch of powder. To measure the tap density the volume of powder undergoes controlled vibrations in order to facilitate the rearrangement of the particles that moves toward a more stable equilibrium, lowering the gravity centre of the system. To compensate the volume diminution caused by the compaction, other powder is added to the cylinder. The procedure is repeated until the achievement of the maximum grade of packing. The density of the rearranged powder is the tap density.

The relation between apparent and tap density is the *Hausner ratio* [47]:

$$H = \frac{\rho_t}{\rho_a} \tag{1}$$

where ρ_t and ρ_a are respectively the tap and the apparent density.
Hence, the closer to unity is the Hausner ratio, the higher is the packing grade of particles and as a consequence, the higher is the flowability. Therefore, H could be interpreted as an index of the quality of the powder flow [48], [49].

Among the defects that must be taken in consideration, there is the eventual presence of porosity inside single particles as in Figure 7 [50]. These may generate during the powder formation mechanism, where high pressured gas used for atomization can be entrapped in the metal droplets. This internal porosity can degrade the quality of the final part. In fact, after the interaction between the laser and the powder, the gas entrapped in the powder expands, leading to the formation of spherical porosity in the final part.

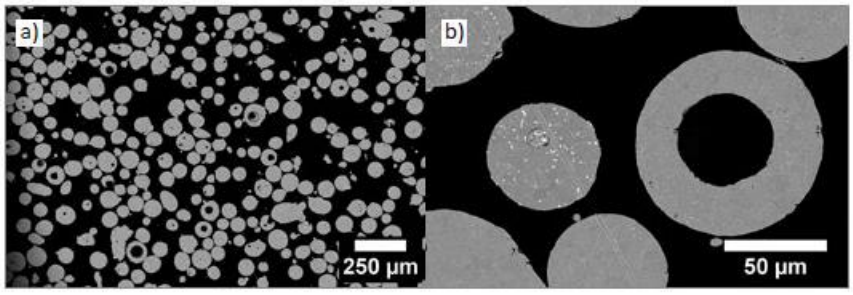

***Figure 7**: Section of metallic powder with internal porosities* [50]

Another important aspect to take into account is the quality of the recycled powder. Only a portion of the entire powder batch introduced in the SLM machine is effectively used to build a part. Hence, most of the powder can be recycled, thus minimizing the waste and reducing the production costs.

Different strategies can be used when it comes to the powder recycling phase, as listed below [44]:

- Before each build, sieved and used powder are mixed in constant proportions with the virgin one
- After a predefined number of jobs, used powder is mixed with other powder of the same age
- Used and sieved powders are added at the top of the virgin powder batch without any mixing
- After each job, sieved powder is reintroduced without any mixing

The last strategy is the most common one because, from an operational point of view, it is simple, but, at the same time, it guarantees a sort of control on the raw material conditions thanks to the sieving.

After the completion of a PBF process, as stated in [51], remain two kinds of powder. The powder that interacted with the heat source and the one that has not. To the first group belong the particle that has been heated or partially melted by the laser and can be subdivided in laser spatter and condensate that are caused by the evaporation of the powder. More in detail, laser spatter is a "drop" of material that is ejected from the melt pool during the laser scanning [52], [53]. Due to the lower solidification rates, if compared to the one of the melt pool, the spatter is generally characterized by a coarser microstructure, as better explained in the following paragraphs. Moreover, spatter particles usually have rough surface and a bigger size than the one of the fresh powder.

To the second group belong those particles that have not been affected by the heat source, so they are similar to the fresh particles except for the fact that they could be coated by the condensate, thus influencing absorptivity and flowability of the powder. Therefore, this powder can be reused after a sieving process. Fig. 8 shows the differences between fresh, sieved and reused powder and spatter [54].

The similarities, in terms of morphology and microstructure, between fresh and sieved particles are evident. Both of them have a smooth surface and an almost spherical shape with the presence of some satellites. On the contrary, spatter particles present an irregular and rough surface with a microstructure characterized by a fine dendritic distribution of Silicon in the Aluminium matrix.

These similarities between sieved and fresh powder suggest a comparable behaviour during the building stage, and, as a consequence a similar answer of the built part in terms of mechanical characteristics. This fact has been confirmed by many studies as for example the one of Maamoun et al.[55] in which are discussed the microstructural and mechanical behaviour of AlSi10Mg parts built both with fresh and recycled powder. Same conclusion has been reached in study [54].

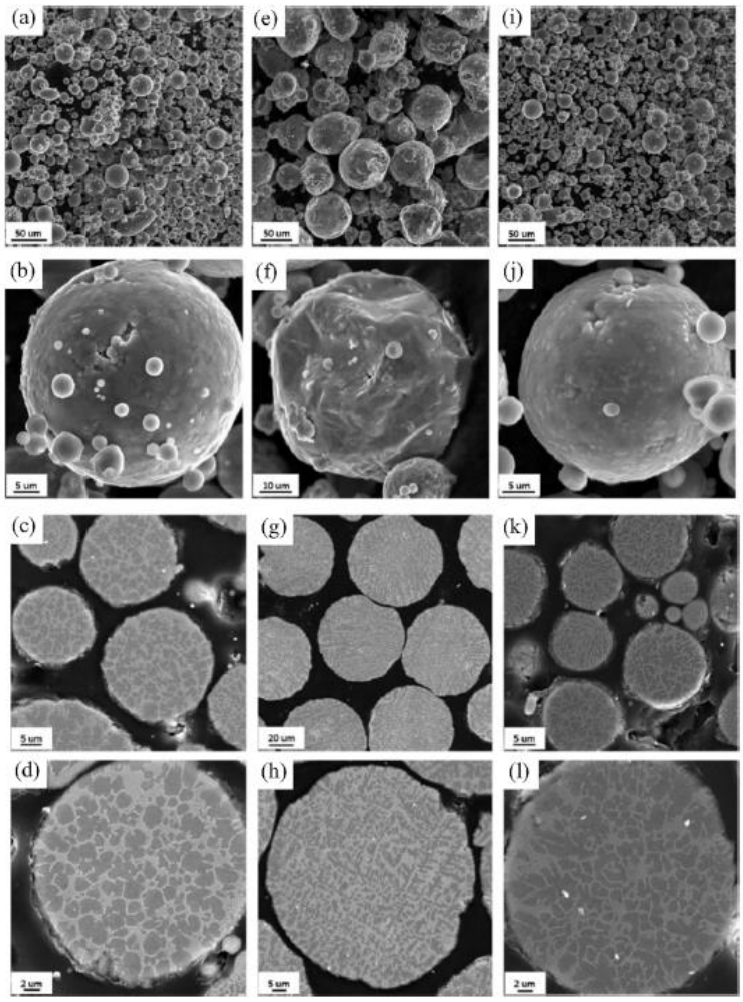

***Figure 8**: Differences between fresh AlSi10Mg powder (a-d), spatter particles (e-h) and recycled powder (i-l).*[54]

The main problem with recycling is the almost inevitable degradation of the powder that indicates that there should be a maximum number of cycles for a reused powder. In fact, even though the powder sieving should avoid the presence of large agglomerates of particles, the handling of the powder generally occurs in presence of air. Hence, a possible oxide layer on the sieved particles could be present. This, if not correctly broken by the laser, hinders the correct melting of the powder, with consequent defects in the built part.

This problem may be solved by drying the powder before the usage or setting a low power laser scanning on the powder bed before the full power scan.

Moreover, it must be taken in consideration that, inevitably, the powder size distribution changes with the re-use of the powder. The fraction of smaller particles decreases while the one of the bigger particles increases. This phenomenon affects the process in terms of different flowability of the powder and different interaction with the heat source, in comparison to the first job with fresh powder.

2.6 Effect of Process Parameters

L-PBF and more in general SLM processes are based on the interaction between a heat source and the raw material. Therefore, process parameters play a fundamental role in this interaction since they influence the way the material is melted and, as a consequence, the quality of the final part in terms of density, defects and mechanical characteristics.

The L-PBF parameters can be classified in four main categories [16]:

- Laser related parameters
- Scanning related parameters
- Powder related parameters
- Temperature related parameters

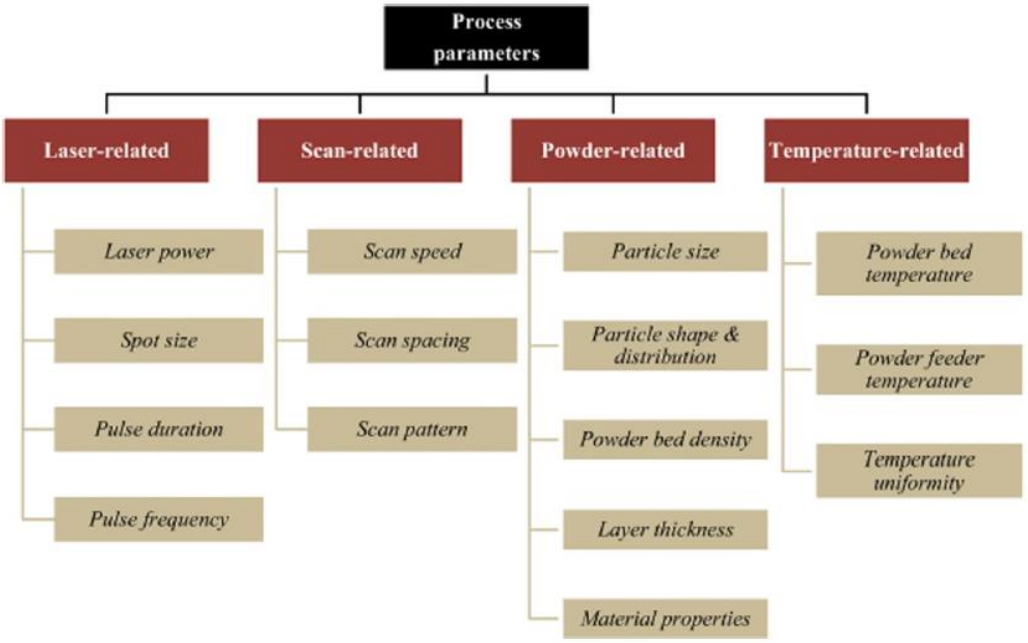

Figure 9: *tree-graph representing the classification of process parameters involved in L-PBF technology* [16]

Before looking in detail some of these parameters, an introduction to the types of LASER used in L-PBF must be made.

LASER type

The LASER is representative of the source of energy in L-PBF, hence the adoption of the optimal one is necessary to guarantee a controlled and consistent process. The main LASER types can be classified in three main categories:

1- CO_2 Lasers
2- Nd:YAG Lasers
3- Fiber Lasers

Regarding the first type, CO_2 Laser is one of the earliest gas lasers developed. This kind of laser can generate light beam output with a wavelength from 9 to 11 μm, but due to this infrared emission, special materials must be used for the optical components as, for example, silver or

gold for the mirrors. The main advantages consist in the high power efficiency and high output power. However, due to the limited absorptivity of metals in the infrared field[56], CO_2 lasers are not the best candidates for L-PBF process. In addition, for beam delivery in this particular wavelength range, fibers cannot be used, thus requiring fee-space bulk reflective optics for beam delivery.

Nd:YAG lasers exploit Nd:YAG crystals as a solid gain medium. This is pumped by a flash lamp or by an 808 nm diode laser, while the output is a near infrared with a wavelength of 1064 nm. In contrast to CO_2 lasers, Nd:YAG lasers can use fiber as beam delivery. However, they have been substituted with Yb fiber laser in AM due to the low electrical to optical power conversion efficiency.

Yb Fiber are the most commonly used lasers in AM thanks to their reliability, good electrical to optical power efficiency, compact size and low maintenance[57]. They are pumped by lasers diodes and produce a near infrared output with the wavelength in the range of 1030 – 1070 nm.

Regardless the kind of laser used, the energy impinging on the raw material is absorbed or reflected in quantities depending on several factors. One of them is the material absorptivity at a particular wavelength. Generally, metals have higher light absorptivity the lower is the wavelength of the incident ray, as shown in Fig. 10, which is why Fiber Lasers are preferred to CO_2 Lasers.

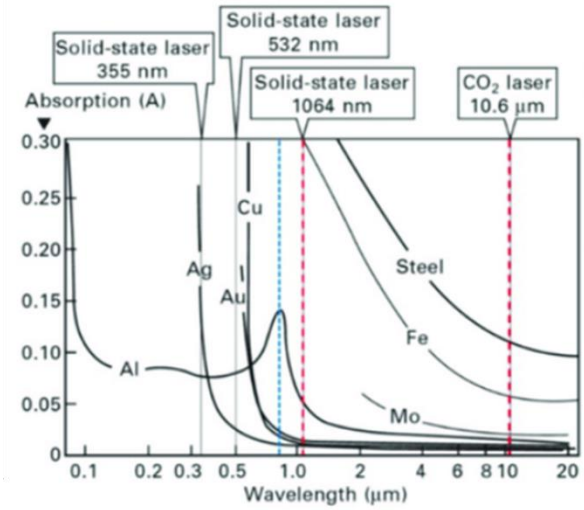

Figure 10: *Difference LASER absorpitivities by the interaction with different metals*[58]

Moreover, some materials, as aluminium or copper, are characterized by a high reflectivity and thermal diffusivity, thus requiring a higher laser intensity for a correct melting, where the laser intensity is defined as the laser power per unit of area and it must exceed a certain material limit to guarantee its melting. In addition, it must be considered that the absorption of laser energy by the molten material is higher than those for solid material. (These are only few phenomena that occur with the interaction between the laser energy and the raw material).

When a too high laser power is applied, plumes of vaporized metal or plasma can form above the melt pool, absorbing the successive laser energy and preventing the continuity of melting of the powder layer. If moreover the pressure of the vaporized powder increases, a depression occurs in the melt pool, with a consequent trapping of the laser energy. Hence, as a consequence, a preferential melting occurs and a vapour cavity is created. This phenomenon is generally known

as keyhole mode and could lead to drawbacks as porosities or cavities in the printed part[59], [60], as better explained in the following paragraphs.

Energy density

Energy density is, in general, the most common metric used in AM for the process parameters optimization. It can be defined as linear, areal or volumetric.

The *linear energy density* is calculated as the ratio between laser power P [W] and scanning speed velocity v [mm/s], as reported here following:

$$ED_l = \frac{P}{v}, \quad [\frac{J}{mm}] \tag{2}$$

The *areal energy density* take count also of the hatch distance h [mm]:

$$ED_{ar} = \frac{P}{v \cdot h}, \quad [\frac{J}{mm^2}] \tag{3}$$

In any case, the most common parameter used in literature is the volumetric energy density (VED), which incorporates the layer thickness t:

$$VED = \frac{P}{v \cdot h \cdot t}, \quad [\frac{J}{mm^3}] \tag{4}$$

It appears clear that several combinations of parameters could be adopted maintaining unvaried the energy density. Many authors adopted this approach for the evaluation of the correlation between this parameter and the quality of the final part, in terms of density, surface roughness and mechanical characteristics [61]–[64].

Actually, the energy density transferred to the metal powder depends on other factors not reported in the formula, as the material absorptivity and heat conductivity, the effect of the heat convection related to the gas flow, the laser spot size. Therefore, some studies [65] focused on the evaluation of the normalized energy density, that takes in consideration some of these aspects.

$$ED^* = \left(\frac{A \cdot P}{2 \cdot v \cdot t \cdot r}\right) \cdot \left(\frac{1}{0.67 \cdot \rho \cdot C_p \cdot (T_m - T_0)}\right) \cdot \frac{1}{h^*}, \tag{5}$$

where:

- A is the material absorptivity
- P is the laser power
- v is the scanning speed
- t is the layer thickness
- r is the laser spot radius
- ρ is the material density
- C_p is the material heat capacity

- T_m is the specific melting temperature of the material
- T_0 is the initial temperature of the powder bed
- h* is the ratio between hatch distance and laser spot radius

However, this definition, though more punctual from a physical point of view, has its limitations, starting from the calculation of the material absorptivity A. In fact, researchers are still on the evaluation of a correct absorptivity coefficient for the different materials in form of powder. Therefore, the adoption of an A value from literature, typical of polished metal plates or of oxidised surface is forced, making almost vain the utilization of ED* parameter. So, in this thesis will be used only the linear and volumetric definitions of energy density.

Laser power, scanning speed and hatch distance are, therefore, the main parameters studied in literature to achieve a full density part, without defects, and with a low surface roughness.

In detail, the *laser power* is defined as the power value that is transferred from the heat source, so the laser, to the powder material.

The *scanning speed* is considered, together with laser power, one of the most influencing parameters on the quality of the final part. In general, high scanning speed means low exposure time of the laser on the powder bed, thus decreasing the width and depth of the melt pool. The problem with too high scanning velocities is the risk of not correctly bonding two successive layers, with consequent occurrence of cracking and defects in the part.

The *hatch distance* is defined as the spatial gap between two consecutive scanning at the same layer. Generally, is imposed as minor than the dimension of the laser beam to guarantee a certain degree of overlapping between the two adjacent scanning. This to avoid the presence of not melted area with powder particles not fused.

For the processing of Al alloys, a high laser power is required since, as underlined above, the material has a high reflectivity. Many studies have also reported how a low scanning speed should be preferred, since it leads to the minimization of the porosity and defects in general, as well as balling phenomenon [16]. Obviously, from a productive point of view, the decrease of the scanning speed is inversely proportional to the production time, with the consequent increase of production costs. Hence, a compromise should be reached between productivity and part quality, as better explained in Chapter 5.

The *scan strategy* is defined as the pattern of the laser scan, in terms of orientation of adjacent tracks within a layer. The optimization of this parameter is generally linked to the limitation of the anisotropy problem. In fact, the printing process mechanism results in the formation of a final part in which each layer is fundamentally welded to the previous one. This phenomenon causes a consequent not isotropic behaviour of the printed piece. Many scanning strategies have been studied in literature related to this problem. In this regard, random scanning is often used so that there is no preferential direction for residual stresses induced by the scanning.

Another parameter that plays a fundamental role in L-PBF is related to the *process atmosphere* and in particular, the inert gas used in the chamber. In other words, the type of gas used, and the corresponding speed have a great impact on the printing. Generally, the quantity of oxygen present in the building chamber is kept below 0,1% to limit problems related to the oxidation of the metallic particles during the printing stage. Therefore, the chamber is filled with an inert gas,

typically Argon (Ar), nitrogen (N_2) or helium (He). A study on SLM process of Al alloy demonstrated how the mechanical characteristics of the printed part are not depending on the type of inert gas adopted, exception made for helium, which led to the production of the part with greater porosity [66].
The gas flow rate within the chamber has a great influence on the quality of the final printed part since it affects the amount of residual spatter on the powder bed. It has been demonstrated that, generally, the imposition of a high gas velocity is preferable. In this way, gas can carry the spatter to the outlet [67]. It must be remembered that the more spatter is present on the powder bed during the printing stage, the more defects will be present in the final part. However, the gas velocity must not be increased too much, otherwise problems related to the transportation of fresh powder to the outlet could take place, as denudation of the tracks and inhomogeneous layers.

2.7 Defects

As stated before, especially Al alloys are difficult to process for their high reflectivity, high thermal conductivity and high reactivity, for example, to oxygen. For all these reasons, Al parts produced by L-PBF are typically characterized by the easy formation of defects. Hence, the main objective in L-PBF production is the minimization of defects, maintaining a good productivity rate.

Depending on the shape and the size of the defect, they can be classified in different categories as porosities, lack of fusion and cracks. In this paragraph is made a detailed discussion on each type.

2.7.1 Porosity

One of the most common defects in L-PBF parts is porosity. They are characterized by a spherical shape and a small size, generally not bigger than 100μm [68]. The causes behind the formation of this kind of defect are different.

First, it could be due to a not proper powder packing on the building plate. That is to say that, if the powder bed density is low, air between the powder particles could dissolve in the molten pool and remains entrapped in it. This due to the rapid cooling rate that hinder the escape of the gas bubbles. Moreover, due to the high temperature reached in the melt pool, the gas solubility of the melted metal is high, making easier its enrichment.

Regarding this, a parenthesis must be opened on the hydrogen pores formation in Al alloys. This is caused by the hydrogen present in the powder material, due to the moisture on the powder surface that reacts with Al in the melt pool with the consequent formation of molecular hydrogen, as in the following reaction [69]:

$$3H_2O + 2Al \rightarrow Al_2O_3 + 3H_2 \quad (6)$$

$$H_2 \rightarrow H_{ab} \quad (7)$$

where H_{ab} is the absorbed hydrogen in the melt metal. Here, if the corresponding quantity is superior than the maximum hydrogen solubility at the relative high temperatures in the melt pool, hydrogen pores are generated and start to coalesce, with consequent detrimental effect on the final part.Hence, it appears clear that the reduction of moisture on the powder surface must be guaranteed. This could be achieved in two ways.

The first method involves the powder drying in a furnace before putting it in the SLM machine tank. This, on the other hand, has the possible detrimental effect of a sintering of the powder particles, with a consequent not uniform behaviour of the powder when interacting with the heat source.

The second method involves a pre-heating of the powder bed. This is made by a first laser scanning on the powder bed with a low laser power before the actual scanning at the imposed higher power for the real melting of the layers.

Another cause of the formation of porosities could be determined to the initial pore presence in the metal powder. These porosities may generate during the powder gas atomization, where the high pressure gas can be entrapped in the metal droplets.

Gas bubbles could be also related to the process parameters imposed. In fact, if the laser power is too high or the scanning velocity and the layer thickness are too low, the energy density applied to the powder bed increases. The melt pool temperature rises until the achievement of the evaporation point of the low melting elements present in the alloy, with consequent spherical defects in the printed part.

Moreover, the application of a high energy density leads to a melting mechanism defined keyhole mode, according to which the melt pool shape becomes narrower and deeper. If the keyhole is not correctly controlled it can become instable and can collapse, entrapping the vapour gases in the melt pool and causing consequent porosity defects.

2.7.2 Lack of Fusion defects

These defects are generally characterized by an irregular shape and a size bigger than 100µm. The main reason for the formation of lack of fusion defects lies in the choice of the not optimal process parameters. In fact, if the laser power is too low or the scanning speed is too high, the energy density applied to the powder bed results to be too low for the correct re-melting of consecutive layers. Therefore, problems of poor bonding between layers may occur in the final part (Figure 11).

Moreover, if laser energy input is too low, the melt pool width may not be enough to guarantee a proper overlapping between adjacent scanning tracks. This obviously could be directly due to the imposition of a too high hatch distance. In the case of an insufficient overlapping, lack of fusion defects are usually characterized by the presence of un-melted powders in the cavity, as shown in Fig. 11.

The direct consequence of these kind of defects, is that the surface in which it has been formed may be rough, hindering the deposition of a successive homogenous layer and the correct flow of the molten material, thus affecting the next interaction between laser source and powder bed.

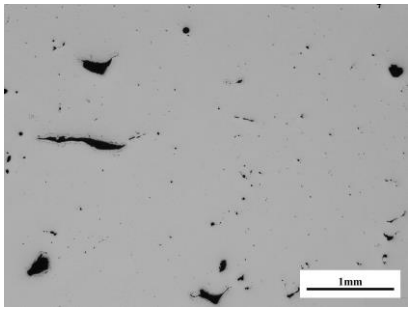

***Figure 11**: Optical image of lack of fusion defects*

A correct bonding between consecutive layers could be impeded also by the presence of oxide films. Aluminium alloys, as AlSi10Mg, are easily subjected to oxidation. Though maintaining the building chamber atmosphere with a quantity of Oxygen generally below the 0,1%, oxide inclusions may form in the printing part. These could have two different origins. One derives from the possible oxidized surface of the metal powder, the other from the oxygen entrapped in the turbulent molten flow. For aluminium alloys oxide films reduce the wettability of the melted

material, hindering the fusion of the metal powder and leading to a not-bonding layers defects [52].

Al oxides are generally brittle. A study [19] stated that, if a proper amount of energy input is applied, the oxide film on the upper surface evaporates, while those on the lower side may break under the effect of Marangoni flow. Hence, little residual of oxides could be found in the printed part.

2.7.3 Cracks

During SLM process, the melt pool solidifies with a cooling rate that reaches 10^8 K/s. This generates high thermal gradients, so, as a consequence residual stresses in the printed part. The combination of thermal and residual stresses gives place to a possible crack nucleation and successive propagation.

A way to reduce hot cracking ignition is working on the alloy itself. For example, the addition of Si reduces the melting temperature and solidification range, thus lowering the possibility of hot crack formation.

In addition, cracks may propagate also from inside porosities, which disposition may give a preferential path for the crack to propagate. Even all those kind of irregular defects with a not precise spherical shape could be place for cracks nucleation, due to the relative notch effect.

2.7.4 Balling

The balling phenomenon is one of the principal causes of a high surface roughness. It consists in the separation of the scan track in spherical balls, with detrimental effects on the process continuation.

Balling phenomenon occurs when high scan speeds or low laser power are adopted. A detailed study [70] shows the relationship between the linear energy density ED_l and the balling phenomenon.
If ED_l is too low, for the imposition of a too high scan velocity, the heat amount transferred to the powder is not enough to guarantee the correct wettability of the scan track with the substrate. This may also happen in the presence on the previous layer, of an oxide film that, because of the poor energy density applied, may not break, lowering the wettability of the molten pool [19].

The mechanism behind balling formation is driven by the surface tension and by the general tendency of the material to minimize its Gibbs surface free energy [30]. At very high scanning speed, the molten pool tends to become longer. If the critical length is reached (Eq. 8), the molten pool separates in spherical droplets, pushed by both internal capillarity and surface free energy forces. The critical length is defined by the Rayleigh instability ratio:

$$\frac{\lambda}{d} > \pi \tag{8}$$

where λ and d are respectively the length and the diameter of the melt pool, as in Fig. 12 [71].

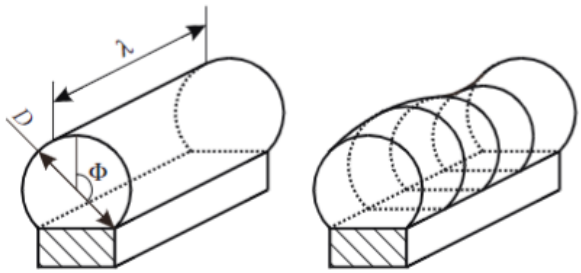

Figure 12: *scheme of the melt pool along the scanning direction. If the critical length is reached the melt pool starts becoming instable until the separation in droplets* [71].

The molten pool can be subdivided in two regions (Figure 13), the upper one relative to the fusion of the new powder layer and the other representing previous layers re-melting [72]. The upper one has the tendency to ball, driven by the surface tension at the interface gas-liquid. This tendency, if an adequate energy density is applied, is hindered by the tension produced by the liquid-solid interface at the lower part of the melt pool, maintaining the stability of the scan track and limiting the balling effect.

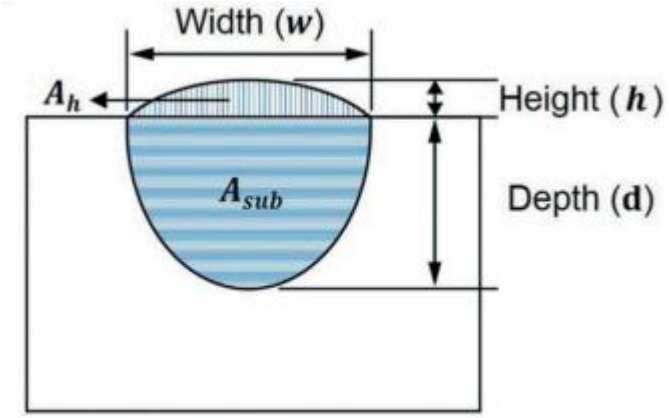

Figure 13: *Representation of the melt pool along the building direction.*[72]

Another consequence of the application of an insufficient ED_l, is the shortening of the solidification time. This means less time for the wettability with the substrate, resulting in possible balling phenomenon.

Generally, when the balling phenomenon occurs, on the scanning track may adhere not melted powder satellites, resulting in a not homogeneous track. Therefore, the spreading of the following powder layer will be uneven, with the consequent not uniform interaction between the laser heat source and the powder bed. Moreover, when the laser scans the following layer, the balls and satellites of the previous one cannot be melted due to the insufficient energy density, contributing to the formation of new defects.

Another aspect that contributes to the occurrence of balling phenomenon is the Marangoni convection. This is related to the material transfer driven by a tensional gradient inside the melt pool. Actually, the impinging laser energy has not a uniform distribution on the spot area, but a Gaussian one. That is to say that the powder in correspondence of the spot laser border receives

a lower energy density, if compared to that in the middle of the spot. Therefore, temperature gradients occur in the melt pool, with consequent surface tension gradient. This unbalance generates a melt material flow from region with low surface tension to those with high surface tension. This phenomenon is described by the Marangoni convention intensity, which can be calculated as following:

$$M_a = \frac{d\sigma}{dT}\frac{l_0 \Delta T}{\mu \alpha} \tag{9}$$

where ΔT is the temperature gradient, l_0 is the characteristic length (in this case is the melt pool one), μ is the material Poisson ratio and α is the material thermal diffusion coefficient.

When the Marangoni number reaches a critical value, the convective flows so, as a consequence, the scanning tracks, become instable and may break up into several spherical agglomerates, to achieve a more stable condition given by the minimization of the free surface energy.

2.7.5 Spatter

Spatter is defined as droplets of material ejected from the melt pool during the laser scanning. Generally, these droplets oxidize in flight and then land on the powder bed. If they fall on a portion of the powder bed interested by the laser scanning, the spatter may have detrimental effects on the printed part. This because, generally, spatter particles are bigger than the virgin powder [52]. Therefore, the spreading of the subsequent powder layer will be uneven, with a consequent not uniform distribution of the laser radiation. Moreover, the laser energy may not be high enough to correctly melt the full spatter particles, so that they remain entrapped in the part as inclusions.

The spattering is mainly driven by the combination of vapour recoil pressure and Marangoni convection. A study reported a simulation to explain the physics behind this phenomenon[73].

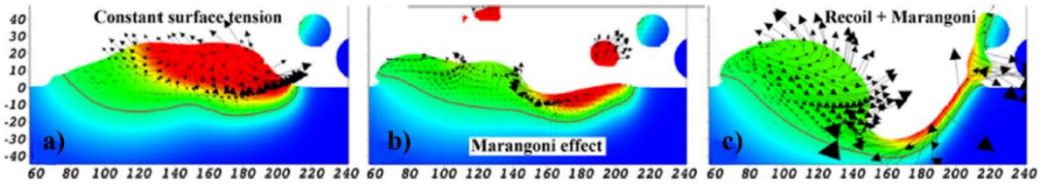

Figure 14: *Simulation of the spatter generation driven by the combination of Marangoni effect and vapour recoil* [73]

As shown in Fig. 14 a, with a supposition of a constant surface tension, the melt pool is less deep and the material transfer is only driven by the temperature gradient.

However, the strong temperature differences in the melt pool are related to temperature dependent surface tension, thus creating Marangoni convection (fig. 14b), explained in the previous paragraph. It transfers the fused material from the region with higher temperature to the rear one with a lower temperature. In other words, Marangoni effect homogenizes the temperature distribution in the melt pool thanks to the recirculation of the melted metal and may generate spattering from the expulsion of liquid material with lower viscosity.

Due to the high temperature reached in the centre of the laser spot, the material may reach the boiling temperature. The consequent vapour recoil pressure creates an area of depression in the melt pool, and this, combined to the Marangoni effects, facilitates the expulsion of melted material.

It must be also underlined that the instability of the melt pool becomes critical for high linear energy densities, which increases the Marangoni convection [70]. Therefore, recalling the lower limit of ED_l explained in the previous paragraph, to avoid the Rayleigh instability and consequent balling phenomenon, also an upper limit to ED_l must be defined to reduce spattering.

Another study distinguishes between different types of spatters depending on their corresponding characteristics [74]. The first type is associated to the jet of melted metal from the melt pool portion deformed under high vapour recoil pressure. Then, the ejected particles immediately fall under the force of gravity (Fig.15).

At the same time, under the Marangoni convention, the material is transferred from high to low temperature regions and expelled by the combined effect of high vapour pressure (Spatter type II). These spatter particles oxidize in flight and, in order to minimize their free surface energy, separate in spherical drops.

Moreover, some fused metal accumulates at the front of the melt pool and is pushed frontward by the recoil pressure (Spatter type III).

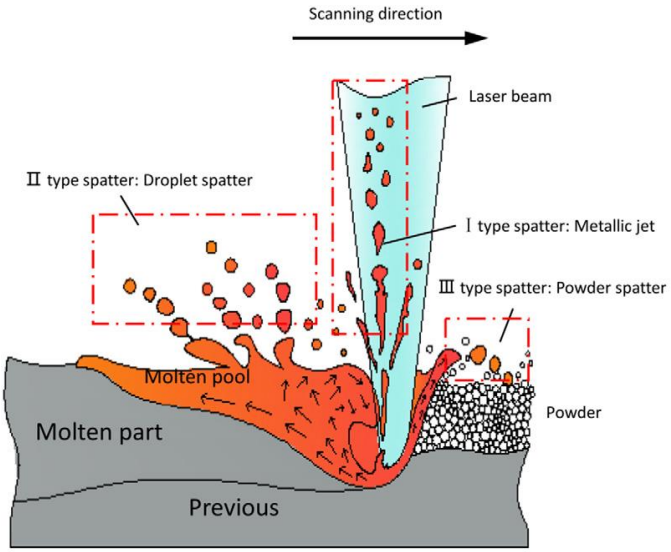

Figure 15*: Distinction of spatter types according to* [74]*: type I is the Metallic jet generated by vapour pressure; type II is droplet spatter due to Marangoni effect; type III is powder spatter that falls forward on powder bed.*

Generally, the vaporization is accompanied by loss of element compound in the allow. According to Simonelli et al. [52], when processing Alsi10Mg, the corresponding spatter is characterized by spherical particles with rough surface, with oxide films rich in Si and Mg.
The loss of elements in the alloy alters its chemical composition, resulting in a different behaviour of the material during the interaction with the heat source.

2.8 Selective Laser Melting of AlSi10Mg

Aluminium alloys are used in several fields in industries, from aerospace to automotive. They represent a compromise between strength and lightweight and are generally not expensive.

For all these reasons, Al alloys have become perfect candidates for SLM production. As stated in the previous chapter, thanks to AM process, parts can be re-designed with different and complex geometries composed by cellular or hollow structures, thus reducing the part weight. Therefore, this technology is exploited whenever high performances and light-weighting are required as happens in automotive. The use of aluminium alloys co-works with the technology itself for the common purpose of reducing weight.

Moreover, thanks to the high solidification rates typical of SLM process, the microstructure is refined without altering the chemical composition, achieving a strengthening of the aluminium alloy.

On the other hand, as underlined in the previous paragraphs, the adoption of Al alloys in L-PBF is challenging due to their high thermal conductivity and low laser absorptivity in the wavelength range of fiber LASERs. Furthermore, aluminium is highly reactive to oxygen, so oxidizes easily with consequent drawbacks as porosity and defects in general.

In any case, the Al alloys that resulted to be more promising in AM are the cast alloys, and, among those, AlSi10Mg is the one receiving more attention. This due to its good cast-ability and to the fact that it is near to the eutectic point. Hence, the melting point is lower and the solidification range is narrower.

AlSi10Mg chemical composition (wt. %)	
Chemical element	Min. ÷ Max. [%]
Al	Balance
Si	9 ÷ 11
Fe	0 ÷ 0.055
Cu	0 ÷ 0.1
Mn	0 ÷ 0.45
Mg	0.20 ÷ 0.45
Ni	0 ÷ 0.05
Zn	0 ÷ 0.10
Pb	0 ÷ 0.05
Sn	0 ÷ 0.05
Ti	0 ÷ 0.15

Table 3: *AlSi10Mg chemical composition (wt. %)*

2.8.1 AlSi10Mg microstructure

The microstructure of AlSi10Mg processed by L-PBF is strictly connected to the interaction between the powder and the heat source. It is influenced by several aspects as the high input energy, the not uniform distribution of laser energy in the corresponding spot, the solidification rates, the re-melting of previous layers and so on.

The process is characterized by typical solidification rates in the range of 10^3 - 10^8 K/s, that lead to a very fine microstructure with metastable phases.

In detail, the characteristic microstructure is shown in Fig. 16, where are represented two sections of the printed part, parallel and perpendicular to the building direction. In particular, the polished section parallel to the building direction is characterized by the melt pools overlapping layer by layer, while along the perpendicular plane the melt tracks are clearly distinguishable.

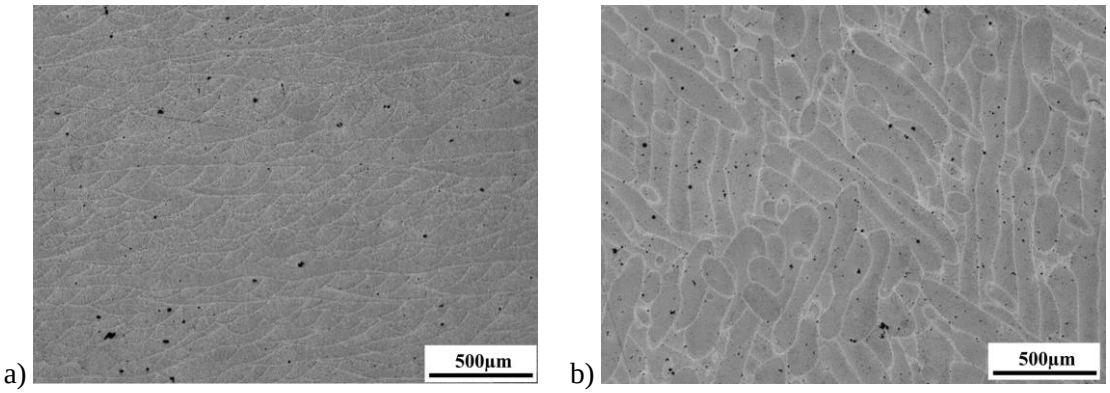

Figure 16: *Alsi10Mg microstructure. a) parallel to building direction; b) perpendicular to building direction*

At higher magnifications, it is possible to analyse the change in microstructure morphology along the two directions. As shown in the SEM image here below (Fig 17), along the build direction (plane XZ) columnar α-Al solidifies surrounded by inter-dendritic Si, while on the corresponding perpendicular direction Al matrix morphology is more equiaxed with inter-dendritic Si segregated on its boundaries. These morphological differences along different directions are due to the thermal history of the melt pool.

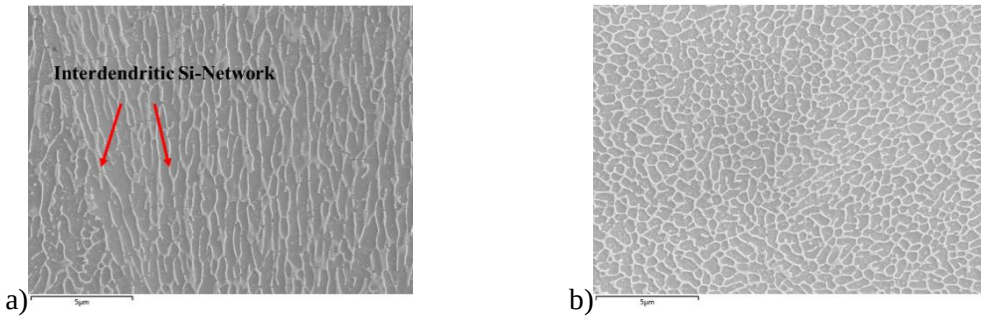

Figure 17: *SEM images of AlSi10Mg AM microstructure parallel (a) and perpendicular (b) to building direction*

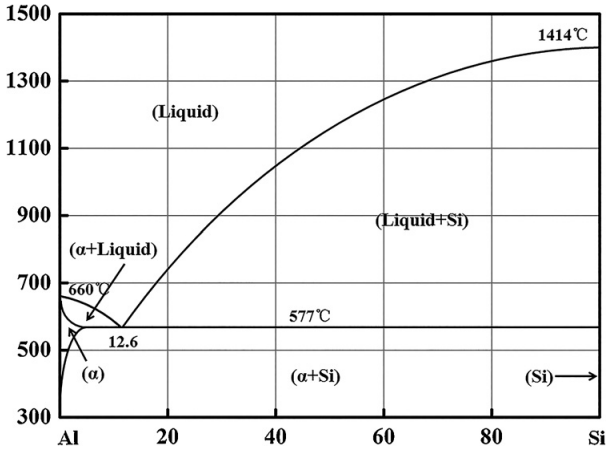

***Figure 18**: Al-Si diagram*

AlSi10Mg (~10 wt% of Si) is a hypoeutectic Al-Si alloy, since the corresponding eutectic alloy is characterized by a Si content of 12,6 wt%. During solidification, according to the Al-Si phase diagram (Figure 18), the melt metal undergoes firstly a phase transition reaction in which alpha phase is formed. In this first solidification step, Si is rejected into the remaining liquid increasing its content in it. Si, that has higher melting point, first nucleates in the melt pool. Then, with the temperature decrease, α-Al nucleates and grows surrounded by Si.

Regarding the solubility of Si in Al, it decreases with the temperature with a maximum solubility of 1.6%, as shown in the phase diagram. Nevertheless, during SLM process the material undergoes a high undercooling that increases the Si solubility in Al up to 8,89%.

The increase of Si content in the liquid with the continuation of alpha phase solidification moves the liquid composition towards the eutectic range with the consequent formation of Al-Si eutectic.

The solidification mechanism for AlSi10Mg alloy is cellular-dendritic. In particular, two different microstructures can be observed: a cellular-dendritic α-Al, rich in aluminium with dispersed Si, and an eutectic Al-Si phase, rich in Si and poor in Al, surrounding α-Al phase. The cellular-dendritic solidification is promoted thanks to the high cooling rates that occur in SLM process.

At higher magnifications, the two phases are distinguishable. As can be seen in Figure 19 [75] the grey islands represent the α-Al matrix, surrounded by the network of eutectic Si phase, represented by the lighter grid. In the α-Al matrix is present a fine dispersion of fibrous Si that has positive effects on the mechanical properties of the as built part.

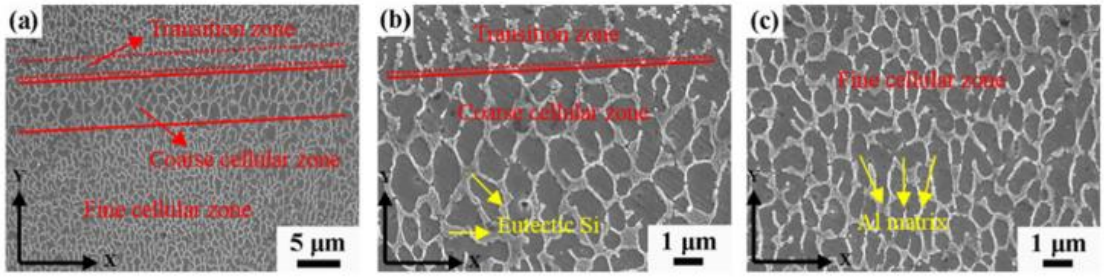

***Figure 19:** α -Al matrix surrounded by network of Si* [75]

The melt pool can be divided in three zones, depending on the different microstructure morphologies. This is due to the Gaussian distribution of energy in the laser spot and to the different solidification rates.

In detail, as pictured in Figure 20, the melt pool is characterized by a region of fine cellular grains (MP fine) that becomes coarser in correspondence of the melt pool boundary, due to the re-melting of the overlapped area. Then, there is the heat affected zone (HAZ), where the network of intercellular Si is broken due to its coarsening. This area represents the material that is not directly interacting with the laser heat source, but that is affected by it.

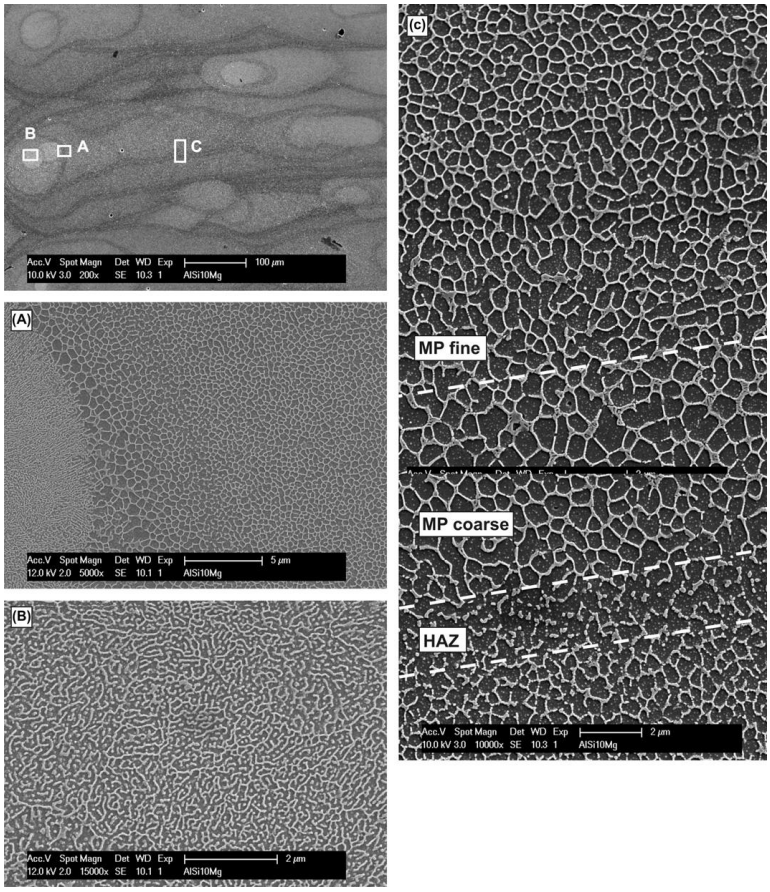

Figure 20: *SEM image representing three melt pool regions* [76]

2.8.2 Texture

The directional solidification in the melt pool leads not only to a morphological but also to a crystallographic texture. This is the main reason for the material anisotropy in parts produced by SLM, which reflects on the typical mechanical behaviour dependence on build direction.

The solidification directionality is linked to several factors as the scanning strategy, the layer thickness, the scan speed that, in addition, influences the melt pool shape. In fact, this, due to the laser movement, is not perfectly semi spherical but is elongated, with consequences on the solidification front direction. This means that, varying some process parameter, the microstructure and grain texture vary in turn.

The solidification mode and the average grain dimension depend on the thermal gradient G and the growth rate R. In detail, the thermal gradient G is defined as the temperature variation along a certain direction, while the growth rate R depends on the laser speed and on the angle between the laser direction and the material growth direction.

The ratio G/R identifies the solidification mode. In particular, the solidification mode changes consecutively from planar to cellular, cellular dendritic, dendritic and equiaxed dendritic with the reduction of G/R. The multiplication of G and R determines the microstructure grade on fineness. The higher the product the finer the grains.

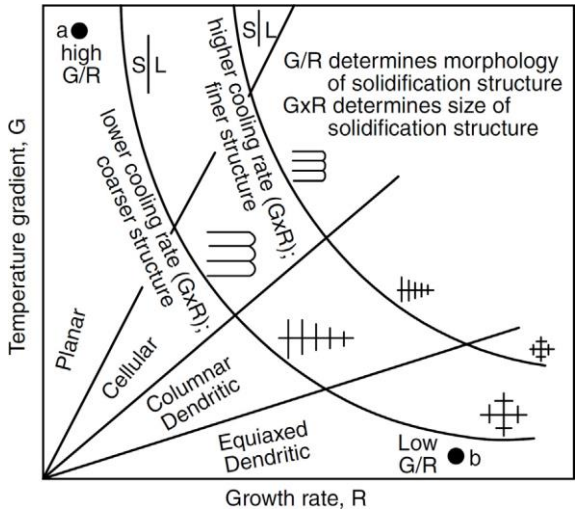

Figure 21: *Temperature gradient G in relation to the growth rate R. The graph shows the variation of solidification mode with the ratio G/R* [30]

G and R vary widely in the melt pool, due to the heat source movement and the rapid cooling rates. They are the highest at the centre of the melt pool and decrease proceeding toward the boundaries. Hence, the grain dimension increases going towards the melt pool boundaries.

As stated in the previous paragraph, the typical solidification mode in L-PBF of AlSi10Mg alloy is cellular-dendritic. In this case it is known that materials with a face centred cubic crystal structure, as aluminium, have a preferential growth towards <100> direction.

Moreover, during solidification elongated grains develop from the melt pool boundaries aligned to the build direction or directed to the melt pool centre, depending on the directional solidification. These phenomena generate the morphological and crystallographic texture in SLM part.

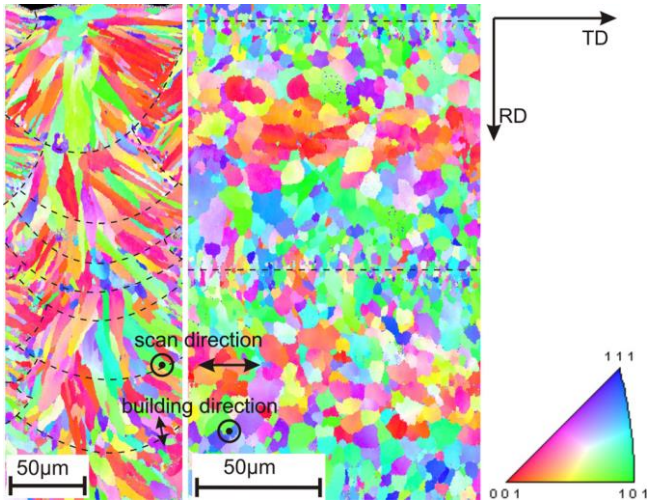

Figure 22: *EBSD analysis of AlSi10Mg AM crystallografic texture. Along the building direction grains preferably towards the melt pool centre while along the perpendicular direction the grains appear as more equiaxed* [76].

At the centre line of the melt pool the grain growth is typically epitaxial. Epitaxial growth occurs where the <100> direction of the substrate crystals is parallel to the heat flow direction, while away from the centreline the new grains nucleate with competitive growth.

Generally, at the top of the last layer the grains, from elongated, become more equiaxed [76]. Equiaxed grains have no predominant crystallographic texture, hence they are desirable when trying to achieve a major isotropy (Figure 22). Probably, equiaxed grains are present on the top region of each melt pool. However, this area is subsequently re-melted during the scanning of the following layer. Therefore, equiaxed grains disappears from the structure and only the one belonging to the last top layer will remain.

To minimize the anisotropy, it has been proved that changing the scanner strategy deeply affects the grains direction [76]. With a mono-directional scan strategy a predominant texture arises along the scan direction with a weak component along the building direction. By rotating the scanning direction each layer the amount of material re-melted is reduced, with consequent increase of the equiaxed grain quantity.

2.8.3 Effect of heat treatments

Heat treatments have significant effects on microstructure of parts produced by L-PBF. Generally, the application of a heat treatment aims to change the microstructure to achieve particular mechanical properties.

As stated before, the as built AlSi10Mg SLM part is characterized by a typical fine microstructure constituted by cellular α-Al matrix and a network of eutectic Si surrounding the α-Al cells. After a solution heat treatment, the Si becomes coarser and spheroidal (Figure 23).

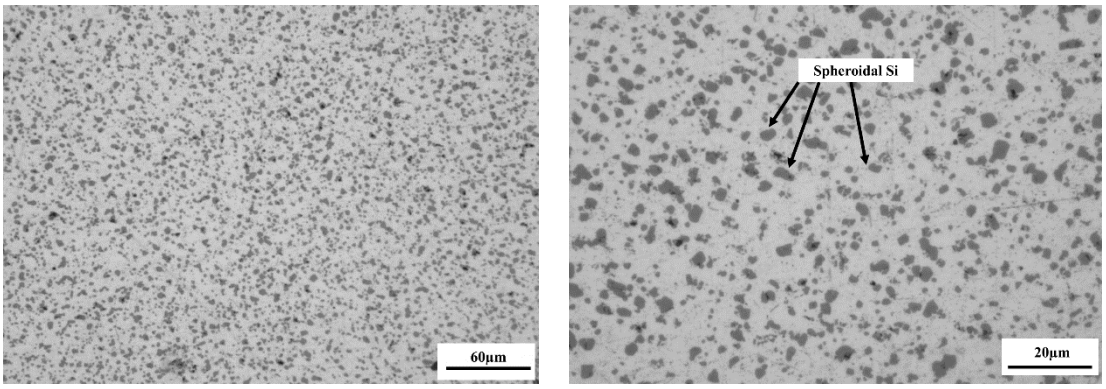

Figure 23: *AlSI10Mg T6 microstructure.*

Si particles grow with the increase of both temperature and time of the solution treatment. The increase in size confirms that in the initial as built condition the α-Al matrix is supersaturated due to the high cooling rates occurring in the solidification stage of L-PBF part. During heat treatment the exceeding Si precipitates in the matrix and increases in size while the number of Si precipitates decrease.

In detail, the reduction of the Si particles number is due to their coalescence and to the Ostwald ripening, according to which big congregates grows at the expense of the smaller ones [75].

The following aging treatment does not have a great influence on the Si particles growth [77].

The presence of magnesium in the alloy enables the precipitation of Mg_2Si after artificial aging that has the effect of improving ductility and strengthen the material. Firstly, the Mg_2Si precipitates nucleation occurs in a metastable β″ phase that gradually changes in β′ phase that provides the maximal strengthening. This is reached thanks to the interaction between the fine distribution of Mg_2Si precipitates and the dislocations. If the treatment exceeds the peak hardening limit, over aging occurs with strength decrease.

The main advantage related to the application of a solution or a T6 heat treatment is the dissolution of the anisotropy typical of the initial as built part. In fact, melt pools are cancelled and substituted by a homogeneous composite like structure in which no directionality is still distinguishable.

On the other hand, the coarser microstructure reduces the strengthening effect of the grain boundaries with consequent rise of the ductility of the material at the expense of the ultimate tensile strength and the yield strength.

In fact, contrary to the typical strength increase after T6 in cast parts, the AM parts generally exhibit a strength drop. This because the solution heat treatment weakens the contributions to the strength of the as built L-PBF parts. These contributions are:

- grain boundary strengthening
- solid solution strengthening
- dislocation strengthening, due to the dislocations movement impediment.

Indeed, the first consequence of a T6 treatment is the microstructure coarsening that limits the grain boundary strengthening. Moreover, due to the Si super saturation of the as built α-Al matrix, Si particles precipitates, decreasing the contribution of the solid solution, while the eutectic Al-Si network starts to break, reducing even more the strength.

Another problem related to the application of a solution heat treatment is the possibility of distortion of the part due to the exposition to high temperatures.

A good compromise to limit the part distortions keeping high strength properties is stress relieving the part before removing it from the build plate. A study [78] revealed that by exposing the part to temperatures in the range of 120-180°C, the effect on the microstructure is almost equal to an artificial aging.
Regarding this, the hardening is not caused by the precipitation of Mg_2Si since this phenomenon occurs only after a solution heat treatment. On the contrary, the strengthening is linked to the precipitation of Si particles from the super saturated α-Al matrix.
Stress relief is also generally recommended since it reduces residual stresses generated during the printing due to the high cooling rates achieved when the laser interact with the powder.

Hot Isostatic Pressing (HIP) is a post-process heat treatment that, thanks to the combination of both high temperature and pressure, aims to internal pores closing by favouring the gas solution in the alloy. However, the high temperatures cause the microstructure coarsening and, hence, a strength reduction. Moreover, HIP is associated to the possibility of oxide formation in correspondence of the open pores at the surface [79].

CHAPTER 3
MATERIALS AND METHODS

3.1 Manufacturing process

All the tests presented in this study were carried out on specimens and components printed by using SLM500 machine (SLM Solution GmbH, Germany). The machine is equipped with four overlapping IPG fiber lasers that work simultaneously with a maximum power for each laser that can reach 400W and an estimated beam focus diameter between 80 and 115 microns. During the process Argon gas with a purity level of about 99,998%, flows in the building chamber to guarantee an inert environment with an oxygen content less than 0,1%, thus reducing the risk of oxide formation inside the printed parts.

SLM Solution GmbH supplied a gas atomized AlSi10Mg powder, with a chemical composition as listed in Table 4, in accordance with the ASTM F3318 standard. The powder had a normal distribution from 20 to 63 µm and a particle size distribution as following: D10=25µm, D50=40µm, D90=65µm.

The incoming powder was generally further analysed inside the company to evaluate the particle morphology. Figure 24 shows SEM images of a common AlSi10Mg powder batch at different magnifications. Particles are mostly spherical in shape, even though elongated particles are also allowed. Powder sent by the supplier should be dry to avoid problems related to the moisture and consecutive gas porosity formation in the printed part. Therefore, the powder is further analysed before being put in the machine, to confirm a humidity level below 5%.

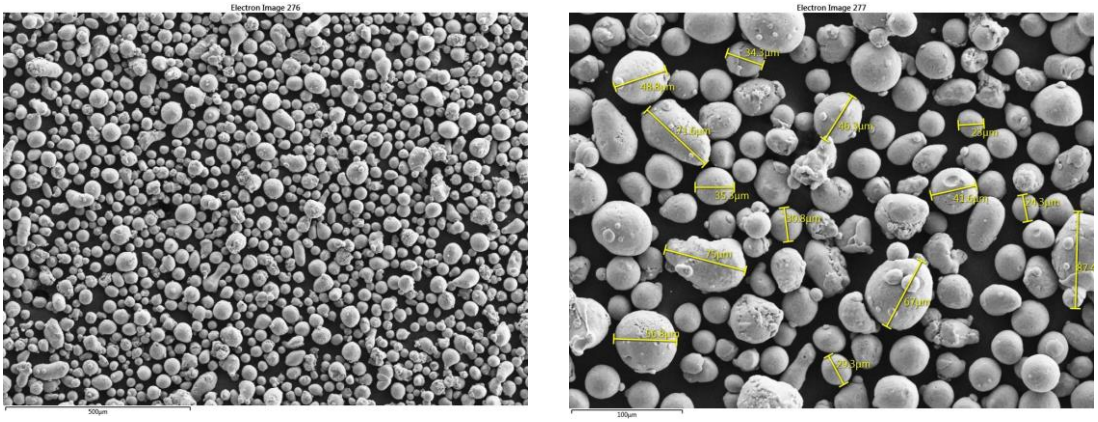

***Figure 24**: SEM images of incoming virgin AlSi10Mg powder at 200x (a) and 600x (b) magnifications*

Element	Al	Si	Cu	Mn	Mg	Zn	Fe
Wt %	Balance	9-11	≤0,05	≤0,45	0,2-0,45	≤0,1	≤0,55

***Table 4:** Chemical composition of AlSi10Mg powder*

The laser power and layer thickness were kept constant at 370W and 60 microns respectively.

Moreover, except for the study on process parameters optimization, in every research carried out in this thesis the hatch distance was set at 0,1mm and the scanning speed at 1650mm/s. The scanning strategy adopted for the experiments was a strip exposure in which each layer is rotated

by an angle greater than 50°, as shown in Figure 25. The build plate was heated up to 150°C during the process to reduce the internal stresses of the printed samples.

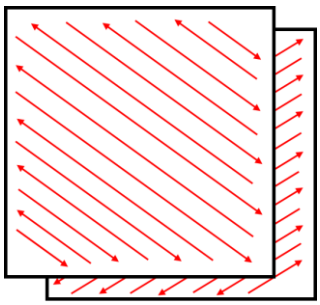

Figure 25: *Scanning strategy with an angle > 50° used in this study*

3.2 Mechanical characterization

3.2.1 Tensile tests

The static mechanical characteristics were evaluated by tensile tests at room temperature (according to the standard UNI EN ISO 6892-1) of specimens with a geometry as shown in Figure 26. The tests were carried out in strain control on the Galdabini Quasar 200 machine (Figure 27) equipped with a 200kN load cell.

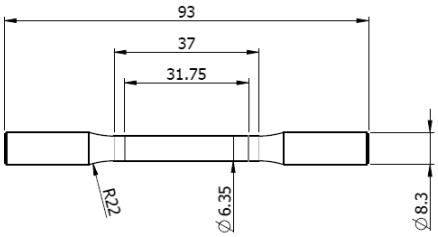

Figure 26: *Tensile specimen geometry*

Figure 27: *Galdabini Quasar 200 machine for tensile tests*

3.2.2 Density measurements

Density was measured using the hydrostatic balance (Gibitre Instruments, Electronic Densimeter Resol2.0) based on the Archimedes' method. According to this, the density (g/cm^3) is calculated as in Equation 10, where m_{air} and m_{water} are respectively the sample weight in air and in distilled water.

$$\rho_{sample} = \rho_{water} \cdot \frac{m_{air}}{m_{air} - m_{water}} \ [g/cm^3] \tag{10}$$

Even in this case the cubes surfaces were previously polished up to 320 SiC paper, to avoid the formation of air bubbles on the surfaces that may skew the results.

The Archimede's density gives information about the whole component volume. To evaluate in detail the density in terms of defects or porosities in the printed part, sections were analysed with optical microscopy. In particular, specimens sections were resin embedded and polished with the automatic polishing machine Tegramin-30, Struers Inc., US), using up to a fine 0,25µm silica suspension. Then, relative density, defined as the area percentage free from defects, was measured with software Olympus Stream Motion on Olympus BX51M optical microscope. Image analysis was conducted on stitched pictures, to investigate a wider area. The images were taken in greyscale and subsequently turned to a binary picture by the application of a certain threshold and setting same light conditions. Relative density was measured on a Region Of Interest (ROI) equal to 45000µm², to be sure to evaluate always the same surface extension.

3.2.3 Microstructural analysis

The microstructure of the as-built and heat treated SLM AlSi10Mg specimens has been analysed using both the optical microscope (Olympus BX51M) and a scanning electron microscope (ZEISS Sigma 300 VP). Before microstructure characterization, the sections were polished (with the automatic polishing machine Tegramin-30, Struers Inc., US), using up to a fine 0,25µm silica suspension and etched with Keller reagent (40% HF, 37% HCl, 69,5% HNO_3, H_2O).

3.2.4 Rotating bending fatigue behaviour of machined and not machined specimens

AlSi10Mg specimens for rotating bending fatigue resistance were tested with a final geometry as in Figure 28.

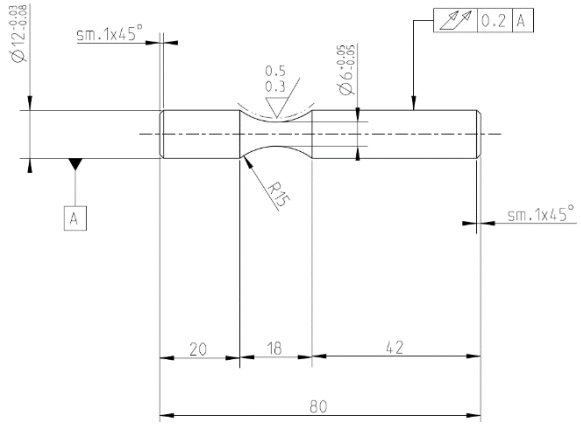

Figure 28: *Rotating bending fatigue specimen geometry*

Samples were tested in machined (M) and not machined (NM) conditions. In detail, for what concerns the machined specimens, cylinders with a diameter of 15mm and a height of 80mm were printed in Z and XY directions (Fig.29) and heat treated with stress relief at 160°C for 6 hours before cutting them from the build plate.

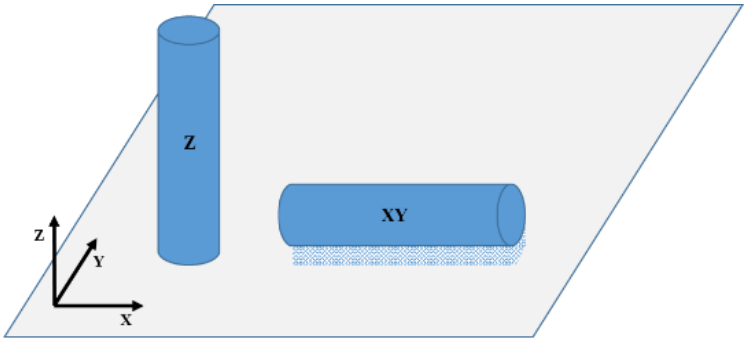

Figure 29: *scheme of printed cylinders to be machined for rotating bending fatigue tests.*

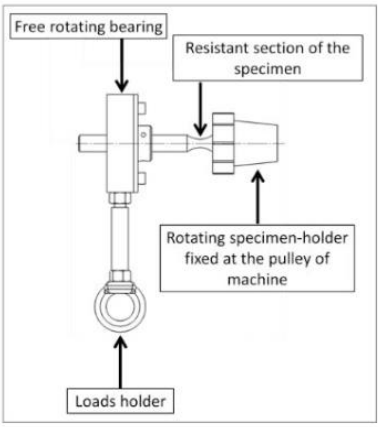

Figure 30: *Rotating bending fatigue setup (single point bending machine)*

Rotating bending fatigue tests were performed at 50Hz (R=-1) on a single point bending machine (represented in the scheme in Fig. 30). Staircase method was adopted to define the fatigue resistance for each batch of specimens, with a constant load variation equal to 10MPa. To identify the correct limit, a minimum of 15 samples for each fatigue test were tested, according to UNI3964 standard. The tests were stopped at the achievement of 10^7 cycles (runout condition), limit imposed for the samples survival, or whenever a specimen failed. If it didn't fail, the next sample was tested at a stress increased by one step. On the contrary, if it didn't survive, the next sample was tested at a stress decreased of one step. When all the samples are tested it is possible to evaluate the fatigue limit at 50^{th}, 10^{th} and 90^{th} percentile, in order to define a confidence range, with the application of the following equations.

$$A = \sum_i^{i_{max}} n_i \tag{11}$$

$$B = \sum_i^{i_{max}} i n_i \tag{12}$$

$$C = \sum_i^{i_{max}} i^2 n_i \,, \tag{13}$$

where i and i_{max} are integer numbers corresponding respectively to the stress level and the maximum stress level imposed during the staircase.

The mean stress μ at 50th percentile can be calculated as follows:

$$\mu_{s0} = s_0 + s\,(\frac{B}{A} \pm 0{,}5) \tag{14}$$

The evaluation of fatigue resistance through staircase method application is linked to the numerical count of survival and failed samples. If the failures are more frequent than the survivals, the lowest load at which a runout occurs corresponds to *i=0*. Starting from this value, the stress level applied directly greater corresponds to *i=1*, and so on. On the contrary if the survivals events are more prevalent, then the lowest load at which a failure occurs corresponds to i=0, while the greater stress levels are combined with *i* values as described above. To each *i* level corresponds a n_i value that stands for the sum of sample failed (or not failed) at that stress level.

s_0 represents the stress corresponding to *i=0*, while *s* is the stress step (equal to 10MPa in this study).

In equation 14, plus sign should be used if the frequency of runouts is greater than the numbers of failures. On the contrary, minus sign should be applied whenever the number of failures is higher than the one of runouts.

Standard deviation σ is defined as follows:

$$\text{if } \frac{AC-B^2}{A^2} \geq 0{,}3 \text{ then } \sigma = 1{,}62 \cdot (\frac{AC-B^2}{A^2} + 0{,}029) \tag{15}$$

$$\text{if } \frac{AC-B^2}{A^2} < 0{,}3 \text{ then } \sigma = 1{,}62 \cdot s \tag{16}$$

After defining the standard deviation, the 10th and 90th percentile can be calculated with equations 17 and 18:

$$\mu_{10} = \mu + \sigma \cdot 1{,}28 \tag{17}$$

$$\mu_{90} = \mu - \sigma \cdot 1{,}28 \tag{18}$$

Once concluded the rotating bending fatigue tests, a post-processing analysis was carried out in order to find a correlation between fatigue limits and printed part quality in terms of internal defects. Therefore, nearly all the fracture surfaces were analysed at stereo microscope and scanning electron microscope, to evaluate the eventual defects at fatigue cracks initiation. Then, the specimens were sectioned along the samples axis for image analysis with the use of optical microscope. For this last analysis the sections were polished with the automatic polishing machine using up to a fine 0,25μm silica suspension.

Hence, the sample sections were analysed at optical microscope to evaluate which kind of defects were present (lack of fusion or internal porosity) and their dimension and circularity distribution.

3.3 Effect of heat treatments on mechanical properties

This study comes from the necessity of finding heat treatments (HT) with two aims, achieving high tensile strength or high elongations. Two different heat treatments have been studied in this work: stress relief (SR) and Solution heat treatment followed by artificial aging (T6).

Stress relief treatments have been carried out at temperatures of 200°C, 210°C, 220°C, 250°C, 270°C and 290°C for 2 hours (Table 5). A last test has been made considering the maintenance of the parts at 160°C for 6 hours.

SR	SR Temperature [°C]	SR Time [h]
SR_160	160	6
SR_200	200	2
SR_210	210	2
SR_220	220	2
SR_250	250	2
SR_270	270	2
SR_290	290	2

Table 5: *Stress Relief heat treatments (SR)*

Regarding T6 heat treatment, different variables were considered in this study: duration of solution treatments, water quenching temperature, and aging temperature and duration. Prior to T6, a stress relief of 160°C for 6 hours was applied to the samples before they were detached from the building plate. Then, in detail, the specimens underwent solution heat treatment (SHT) at a temperature greater than 510°C for 4,5 6 or 8 hours, followed by water quenching (at room temperature or at 75°C). After SHT the samples have been subjected to artificial aging (AA) at different temperatures (150°C, 160°C and 180C°) for times ranging from 4,5 to 14 hours. In Table 6 all the T6 heat treatments applied in this study are listed.

T6	SHT Temperature [°C]	SHT Time [h]	Water quenching temperature [°C]	AA Temperature [°C]	AA Time [h]
T6_1	>510	4	75	150	4,5-8-12-14
T6_2	>510	8	75	180	4,5-8-12
T6_3	>510	4	75	180	4,5-8-12
T6_4	>510	6	RT	160	4-6-8-10

Table 6: *T6 heat treatmens evaluated in this study*

Each heat treatment was evaluated by mechanical characterization and metallographic analysis. Tensile tests, hardness and density measurements were carried out as described in the previous paragraphs.

To have a solid statistical base, 11 tensile specimens built in Z direction and 4 cubes 15x15x15mm³ for density and hardness evaluation were printed for each heat treatment.

The most promising heat treatment was further characterized by rotating bending fatigue tests. Several variables were investigated:

- Influence of part orientation
- Influence of the raw surface
- Influence of printing height

Starting from the influence of part orientation on fatigue limit, cylindrical specimens with a diameter of 15mm and a height of 80mm built were printed both in Z and XY direction (figure 30). Subsequently, they were turned to achieve the final shape (Figure 29) and grinded to obtain a Ra surface roughness, especially in correspondence of the gauge section, below 0,5 µm.

To evaluate the influence of printing height, different regions were considered to investigate the eventual variance of fatigue behaviour all over the building chamber volume and not only in proximity of the building plate. Three zones (A, B and C) were identified. Four plates were printed in Z direction with dimensions of 285x95x18mm. From each plate, three fatigue specimens were extracted in each zone, for a total of 12 horizontal fatigue samples built at the different heights. Furthermore, twenty columns with 350mm height and 15mm diameter were built to extract one specimen per zone, for a total of twenty vertical samples for each zone, as described in the scheme in Figure 31.

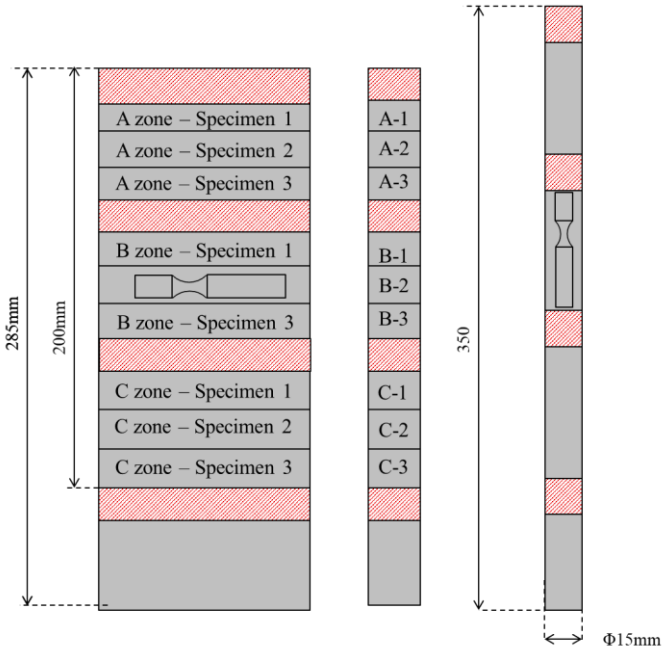

Figure 31: *geometry of plates built to evaluate the variation of fatigue resistance of machined specimens all over the building chamber height.*

Thirdly, a fatigue test campaign was set up to investigate the difference in terms of fatigue life between machined and not machined specimens. This study aimed to estimate the dynamic mechanical characteristics of as-printed part since, as stated in the previous chapter, the near net shaping factor in L-PBF is one of the main advantages of this new technology.

Therefore, sixteen samples were built in Z direction with final shape as in image 28 in order not to be machined. On the other side, 16 cylindrical specimens 80mm high and with a diameter of 15mm were printed in Z direction and subsequently machined. XY specimens were not tested since the not machined ones have supports in correspondence of the gauge length. The supports, if not perfectly removed, leave a rougher surface that could act on the notch coefficient, thus affecting the fatigue limit results.

3.4 Process parameters optimization

To evaluate process parameters effects on mechanical characteristics of AlSi10Mg specimens a Design Of Experiment (DOE) was set up. The variables considered were hatch distance and scanning speed, while maintaining laser power P and layer thickness λ equal to 370W and 60µm respectively. The build plate was heated to 150°C during the process to reduce the internal stresses in the printed samples. The process window considered in this study is shown in table 7. In detail, hatch distance h_d increased from 0,06 to 0,24 mm with a growth step of 0,02mm, while the scanning speed v_s increased from 800mm/s to 2000 mm/s. The values within each cell represent the volumetric energy density (VED) for each pair of variables, calculated as in Equation 4. Given the high number of combinations, in the first step of the analysis the VED range was narrowed by considering just the values around 38 J/mm³ (green cells), with a maximum and a minimum respectively of 45,3 J/mm³ and 30,2 J/mm³.

The second step of the analysis focused on finding optimal process parameters that can guarantee high mechanical properties while increasing the building rate. The building time decrease leads to a reduction of production costs, making L-PBF process more competitive from a productive point of view. In this regard, building time was estimated by calculating the time needed for the scanning of an area of 10mmx10mm, as reported in Equation 19.

$$Build\ time = \frac{A_{10x10}}{v_s \cdot h_d}\ [s] \tag{19}$$

Therefore, the parameters combinations considered in this second step (yellow cells) mainly belong to the left-bottom part of the matrix, where the build time decreases. Table 8 shows the percentage variation of the build time when the slowest parameter set is taken as reference.

VED (J/mm³)		Hatch distance (mm)									
		0,06	0,08	0,1	0,12	0,14	0,16	0,18	0,2	0,22	0,24
Scanning speed (mm/s)	800							**42,8**	**38,5**	**35,0**	**32,1**
	900						**42,8**	**38,1**	**34,3**	**31,1**	
	1000					**44,0**	**38,5**	**34,3**	**30,8**		
	1100					**40,0**	**35,0**	**31,1**			
	1200			51,4	**42,8**	**36,7**	**32,1**				
	1300			47,4	**39,5**	**33,9**	29,6				
	1400		55,1	**44,0**	**36,7**	**31,5**					
	1500		51,4	**41,1**	**34,3**	**29,4**	25,7	22,8	20,6		
	1600		48,2	**38,5**	**32,1**	27,5	24,1	21,4			
	1700	60,5	**45,3**	**36,3**	**30,2**	25,9	22,7	20,2			
	1800	57,1	**42,8**	**34,3**	28,5	24,5	21,4				
	1900	54,1	**40,6**	**32,5**	27,0	23,2	20,3				
	2000	51,4	**38,5**	**30,8**	25,7	22,0	19,3				

Table 7: *Tested combinations of hatch distance and scanning speed. The values inside each cell represent VED. The green and yellow cells correspond to the parameters considered respectively in the first and in the second steps.*

Build Time variation (%)		Hatch distance (mm)									
		0,06	0,08	0,1	0,12	0,14	0,16	0,18	0,2	0,22	0,24
Scanning speed (mm/s)	800							**70,8**	**63,8**	**58,0**	**53,1**
	900						**70,8**	**63,0**	**56,7**	**51,5**	
	1000					**72,9**	**63,8**	**56,7**	**51,0**		
	1100					**66,2**	**58,0**	**51,5**			
	1200			85,0	**70,8**	**60,7**	**53,1**				
	1300			78,5	**65,4**	**56,0**	49,0				
	1400		91,1	**72,9**	**60,7**	**52,0**					
	1500		85,0	**68,0**	**56,7**	**48,6**	42,5	37,8	34,0		
	1600		79,7	**63,8**	**53,1**	45,5	39,8	35,4			
	1700	100,0	**75,0**	**60,0**	**50,0**	42,9	37,5	33,3			
	1800	94,4	**70,8**	**56,7**	47,2	40,5	35,4				
	1900	89,5	**67,1**	**53,7**	44,7	38,3	33,6				
	2000	85,0	**63,8**	**51,0**	42,5	36,4	31,9				

Table 8: *Tested combinations of hatch distance and scanning speed. The values inside each cell represent build time percentage variation in relation to the slowest set of parameters here taken as reference. The green and yellow cells correspond to the parameters considered respectively in the first and in the second steps.*

Three tensile specimens (built in Z direction) and one cube 15x15x15mm³ were printed for each set of parameters. All the samples underwent stress relief. The static mechanical characteristics were evaluated by tensile tests at room temperature (according to the standard UNI EN ISO 6892-1) of not machined (NM) specimens.

The quality of the printed parts was evaluated by measuring the density both with Archimede's method and image analysis, as described in the previous paragraphs.

The best parameter combinations were further analysed by testing a larger number of tensile specimens, to obtain a wider statistical distribution of the data and by rotating bending fatigue tests.

3.5 Surface treatments

As stated in the previous paragraphs, AM is gaining increasing attention thanks to the possibility of producing near net shape components. On the other hand, the technology carries along problems related to the nature itself of the process. In fact, inclined surfaces have a staircase profile because of the adding of material layer-by-layer. This of course leads to a high surface roughness, to which also the not melted powder or the balling phenomenon contribute, affecting the fatigue life or simply the part aesthetic. Hence, here comes the need of finding treatments that can enhance the surface quality.

In this research several surface treatments were considered, divided in mechanical and chemical processes.

According to this classification, among the mechanical surface treatments the following processes were analysed:

- Barrel stone machining
- Shot peening with B60 ceramic beads
- Shot peening with S110 steel shots

On the other hand, the chemical treatments considered were:

- Chemical milling, a process in which components are soaked in an acid solution (H_3PO_4 + HNO_3 + H_2SO_4).
- Green etching® a process in which the components are soaked in a solution without acid contents.
- Hirtisation®, which is a combination of electrochemical pulse methods and hydrodynamic flow that helps support structures removal while improving the surface roughness. Together with the supplier, several tests were conducted to find the correct process setting and the optimal printing parameters for the support structures removal, in order to be more easily attacked by the electrochemical solution.
- DryLyte® (DLT), a process in which small spheres act as electrolyte for the electrolysis reaction. The piece works as the anode of the reaction, therefore when the power is activated, the electrical current starts flowing. The medium is composed by spheres of non-conductive polymeric material that retains liquid electrolyte. One of the advantage of this technology is that the spheres can contact only the surface peaks, hence the material removal occurs selectively in correspondence of the peaks and not the valleys, helping the surface smoothening.

The here listed surface treatments were firstly evaluated by the measurement of surface roughness. In this regard, the evaluation between each process was conducted by the comparison of the area parameter roughness as Sa (arithmetical mean height) and Sz (maximum height). More in detail, Sa parameter describes the height deviation from the mean surface height, while Sz is defined as the sum of the largest peak height value and the largest pit depth value within the defined area [ISO 25178].
The roughness measurements were carried out with the use of Sensofar S Neox confocal microscope on vertical surface of printed cubes. In detail, the evaluation was made on the more exposed surface to the argon flow on areas greater than 2,3x2,7mm^2. For each surface the roughness measurements were repeated at least two times in two different zones.

Each scanned area was acquired and digitalized as a point cloud map with SensoSCAN 6.6 software and subsequently elaborated with SensoMAP 7.4. With this, firstly, a planar filter was applied, then, surface roughness was measured without any further filter to have a first overview of the surface profile. The problem related to the surface roughness measurements on additive components without the use of a profilometer lays in the fact that there is not any reference standard on the precise topic.

For each detected area a second roughness measurement was made with the application of a cut-off gaussian filter equal to 0,8mm. This value was chosen after several attempts to evaluate which filter better fit the surface profile. In this regard, a smaller cut-off was not selected to avoid an excessive elimination of the waviness component of the roughness. In fact, the surface profile of additive manufactured piece is characterized by an intrinsic waviness given by the material adding layer by layer, hence, by the nature of the process itself.

The different treatments were further investigated from a morphological point of view. The surfaces were analysed at stereo microscope and scanning electron microscope to evaluate the treatments effect on the surface's morphology.

After this preliminary analysis, the best surface treatments were chosen to investigate the effect on both static and dynamical characteristics. Hence, tensile tests and rotating bending fatigue campaign were set up. Tensile and fatigue specimens were printed in Z direction and subsequently surface treated. In this regard, in order to guarantee the correct notch diameter of the tensile and fatigue specimens the samples were printed with an appropriate oversizing.

Tensile and fatigue tests were carried out according to the method described in the previous paragraphs.

3.6 Corrosion tests

This study had the aim of going deeper into the corrosion analysis on AM AlSi10Mg components by introducing different conditions and environments. AlSi10Mg specimens were subjected to different heat treatments and surface treatments to evaluate their effects on the corrosion resistance in comparison to other common Aluminium alloys typically used in casting or in plastic deformation processes. All the alloys were tested by immersion in several fluids directly connected to the automotive sector to evaluate their behaviour in their actual working environment.

The corrosion was quantitatively estimated by calculation of the corrosion rate, defined as microns of corroded material per year, to have a numerical and objective comparison between AM AlSi10Mg and the other Al alloys.

Rectangular parts were printed in Z direction with a thickness of 5 mm and a layer thickness of 60 µm. The specimens underwent different heat treatments, to investigate the effects on the corrosion resistance. Some of the samples were heat treated with stress relieve (SR). The remaining samples underwent T6 heat treatment.

To evaluate the eventual influence of surface roughness on the corrosion resistance of AlSi10Mg selective laser melted parts, all the specimens were tested both in the as built and in surface polished condition. In this regard, the automatic polishing machine Tegramin-30, Struers Inc., US was used up to a fine 1200 SiC abrasive paper. Moreover, two other finishing process were applied to some of the AlSi10Mg samples that underwent stress relief: sand blasting (SB) with corundum and DryLyte ®.

As a direct comparison, A356 T6 specimens, with a chemical composition as listed in Table 9, were obtained by sand casting. Rectangular samples with a thickness of 9mm were cast to test the mechanical resistance of the alloy in the raw condition. Even in this case, some of the specimens were polished using up to 1200 SiC abrasive paper to evaluate the corrosion behavior of the bulk material.

Alloy	**Al**	**Si**	**Cu**	**Mn**	**Mg**	**Zn**	**Fe**
A356	Balance	6,5-7,5	≤0,03	≤0,10	0,35-0,45	≤0,03	≤0,15

Table 9: *A356 Chemical composition (wt. %)*

Other alloys from plastic deformation were considered and compared to the AlSi10Mg specimens in terms of corrosion resistance:

- EN AW6082 T6 (extruded)
- EN AW 5083 O (superplastic forming)
- EN AW1050 H24
- EN AW3003 H111

Two kinds of corrosion tests were carried out:

- Partial immersion in salty water (NaCl 5%) for visually analyze the eventual corrosion presence
- total immersion of the samples in different fluids to calculate the corrosion rate

The samples were soaked in different fluids for 30 days. The fluids investigated in this analysis were common for the automotive industry and they were the following:

- salty water (NaCl 5%)
- 5W40
- Oil for active suspensions
- cooling mixture (50% distilled water and 50% glycol)
- automotive gasoline (E10)

The immersion tests in these five different fluids were performed at room temperature for the first step of the analysis, while the total immersions in 5W40, oil for active suspensions and water-glycol (50%) were repeated at T=90°C to simulate the environment in the vehicle.

All the specimens were photographed before and after the corrosion tests to visually evaluate differences on the surfaces in terms of corrosion. After the visual inspection, sections were made in correspondence of the corrosion points. The sections were then polished and etched with Keller reagent. Surface morphology and corrosion products were further analyzed with the scanning electron microscope.

The main aim of this research was to quantitatively estimate the corrosion of additive manufactured (AM) AlSi10Mg parts. Therefore, after immersion tests, the corrosion rate was calculated, defined as µm per year of corroded material. The corrosion rate was obtained according to the standard ASTM G31-72[11], as in equation 20:

$$Corrosion\ rate = \frac{8{,}76 \cdot 10^7 \cdot W}{A \cdot T \cdot D}\ [\frac{\mu m}{year}] \tag{20}$$

where:

- W is the weight loss [g]
- A is the sample area in contact with the fluid [cm²]
- T is the test duration [hours]
- D is the material density [g/cm³]

Limitation behind this definition is that it considers the corrosion as homogenous all over the surfaces in contact with the fluid in which the sample is soaked.

For the correct corrosion rate calculation, each specimen was weighted before and after the corrosion tests. Before, the samples were properly prepared by cutting them to a dimension of 25mmx50mm, cleaned with an organic solution and weighted. Particular attention was made during the cleaning of the AlSi10Mg as built specimens. These samples were ultrasonically cleaned repeatedly to guarantee the correct removal of the not melted powders attached to the raw surface, otherwise a false mass loss could have been measured when it would have come to calculate the weight difference before and after the test.

After the test, the samples surfaces were cleaned from the corrosion products, according to ASTM G1-03[80], repeating multiple stages of immersion in nitric acid (HNO_3) with a concentration of 69%. In each stage, after the immersion in nitric acid, the samples were soaked in an organic solution and ultrasonically cleaned, to help the removal of the corrosion products from the surfaces. The standard suggests repeating the cleaning stages to have greater control on the weight loss. The mass loss should be graphed in relation to the number of cleaning steps made, until the achievement of a curve as shown in Figure 32. The flat segment corresponds to the starting of removal of the bulk material due to the cleaning, meaning that all the corrosion products have been removed. The mass loss value to be considered in the equation 20 is represented by point B.

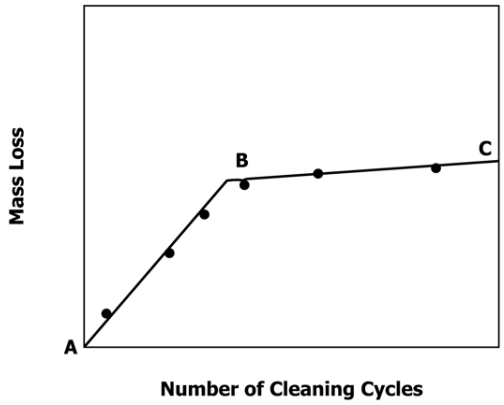

Figure 32*: mass loss after immersion corrosion tests as a function of the number of cleaning cycles according to ASTM G1-03*[80]

CHAPTER 4
MECHANICAL CHARACTERIZATION OF AM AlSi10Mg PARTS

This chapter follows the chronological history of the first steps taken to understand and introduce this not traditional technology.

Therefore, starting from the evaluation of different heat treatments that could answer to requested mechanical characteristic and to different purposes, the best one was further analysed in terms of rotating bending fatigue tests. This with a view of printing not just prototypes but production batches of components that may also have a structural function in the vehicle.

In this regard, several aspects were investigated:

- Building direction
- Effect of surface roughness of as printed specimens
- Influence of the build height to explore all the building chamber volume

4.1 Heat treatments investigation and their effects on mechanical properties

4.1.1 Stress relieves investigation

As stated in paragraph 3.3, two kinds of heat treatments (stress relief SR and T6) were considered in order to achieve the aim of having printed parts with high strength or high elongations. The two opposite purposes were needed to define different mechanical properties options to be given to the technical direction for a proper component design and simulation.

Starting from the SR study, different temperatures and HT durations were considered to study the effects on mechanical properties, thus, to give different mechanical properties windows for the eventual printed parts design.

First of all, not heat treated specimens (built in Z direction with a layer thickness of 60microns) were tested to establish the starting state in terms of mechanical characteristics of the alloy. The first SR evaluated was characterized by a temperature that was slightly higher than the one of the build platform, to look for residual stress reduction while maintaining high mechanical properties.

Absolute mechanical characteristic values cannot be disclosed due to industrial policies. Therefore, UTS, YS and elongations were normalized in relation to the mechanical properties obtained with as printed specimens, here considered as equal to a value of 100. For the stress relief definition only the mechanical properties of as built specimens printed in Z direction were considered. The results, shown in figure 33, confirmed the expectation. In fact, the deviation between not heat treated and SR_160 conditions is negligible.

Not applying any heat treatments has the advantages of high mechanical properties and a lead time reduction during the all production cycle of a component, but it is generally not recommended due to problems related to residual stresses.

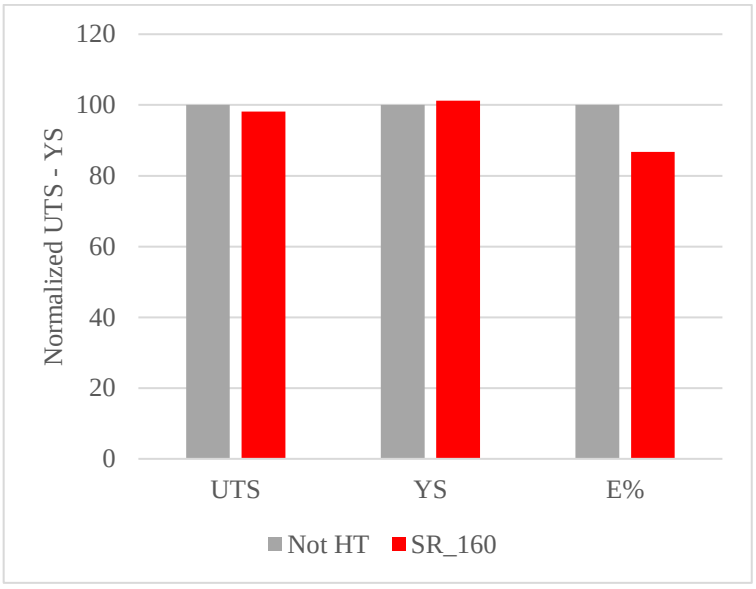

Figure 33: *Comparison between the normalized mechanical characteristics of not heat treateed and SR_160 specimens.*

The residual stresses generate during SLM process due to the rapid solidification rate, which the part is subjected during the printing. Local powder bed regions undergo high temperature that produces punctual transient thermal deformation [81]–[83]. When the heat source is removed, locally the area cools down with solidification rate in the range of 10^3-10^8 K/s, contracting differently from the surrounding parts, thus, originating residual stresses. The different contraction could lead to several problems. The part could locally move during the printing phase, slightly lifting from the powder bed with the risk of collision with the powder recoater, thus causing its consecutive damage. Moreover, residual tensions in the printed part could release after its cutting from the building plate, causing the part deformation. To avoid this phenomenon, printed parts usually undergo stress relief before the wire-cutting phase.

That is why, before SR exploration within a wide temperature range, residual stresses difference between not heat treated and SR_160 heat treated parts was evaluated. In detail, to quantify this deviation, specific cantilever specimens were printed with a geometry as in Fig.34.

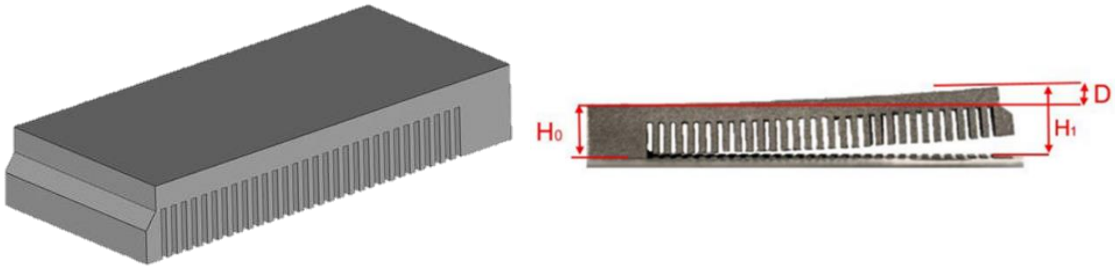

Figure 34: *geometry of the cantilever specimen tested to evaluate the residual stresses due to the process.*

Cantilever geometry has been used in several research [84]–[87] to evaluate the deformation after wire cutting. These cantilever specimens tend to curve once they are removed from the build plate. Their maximum deflection “D” is then measured working as an indicator of deformation caused by residual stresses.

Figure 35 shows the results in terms of displacement “D” of both not heat treated and SR_160 cantilever specimens. It can be seen that the application of stress relief at a temperature slightly higher than the one of the build plate guarantees a reduction of deformation, and as a consequence of residual tensions, of about 40% while maintaining the mechanical properties almost unvaried (Fig.33).

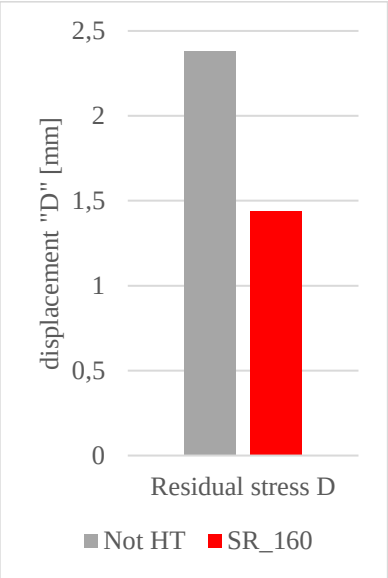

Figure 35: *Difference displacements obtained after cutting the cantilever specimen in the different HT conditions. SR_160 specimens exhibited lower displacement due to the reduction of residual stresses given by the stress relief*

Then, several different stress relieves were considered to establish the mechanical properties range that can be obtained by increasing the temperature while maintaining fixed the heat treatment duration. In this study, as listed in table 5, temperature between 200°C and 300°C were imposed for 2 hours for each SR.

Graph in figure 36 shows the mechanical properties trend obtained with the different heat treatments. In detail, the black horizontal lines represent the not heat treated normal values, considered equal to 100 in this study. The red dots represent the mechanical values obtained with SR_160. It can be deduced that, exception made for SR_160 which temperature is maintained for 6 hours, the temperature increase at the same duration conditions (2 hours) is inversely proportional to UTS and YS values. On the other hand, we assist to a parallel exponential elongation growth together with SR temperature.

Thanks to these trials, it was possible to establish a wide mechanical characteristic range to cover different mechanical designing requirements. Anyway, attention must be paid during heat treatment since, as it can be seen in the graphs, mechanical properties are deeply influenced by the temperature imposed.

Graph in figure 37 represents the percentage variation values listed in Table 10. In detail, Table 10 contains the percentage variation for each variable (temperature, UTS, YS and E) calculated for each temperature step.

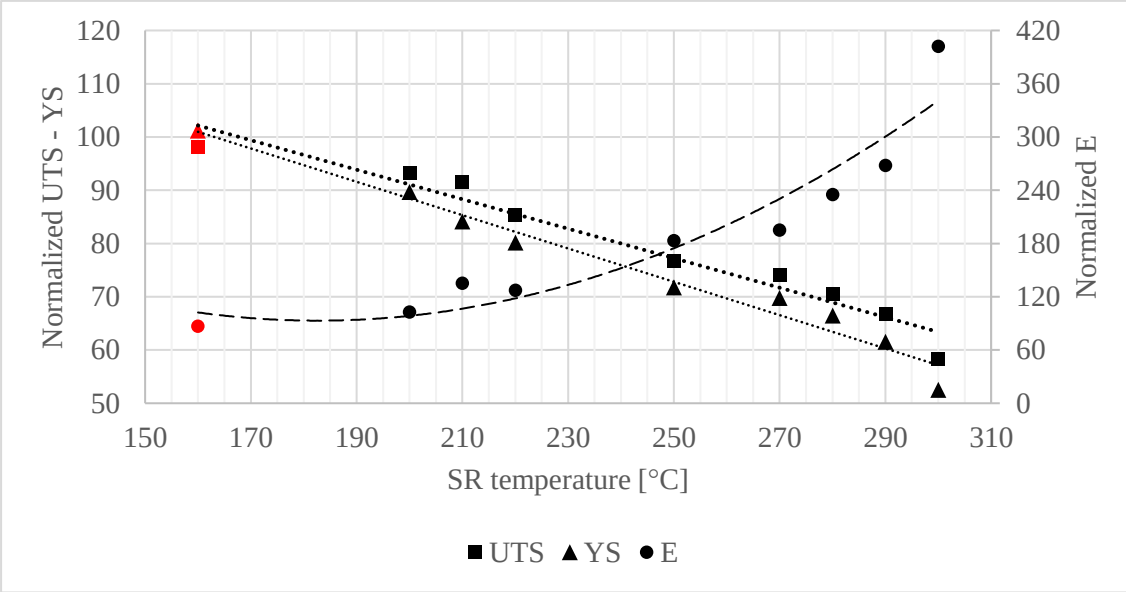

Figure 36: *average mechanical results obtained by testing tensile specimens with the different stress relieves. The results are graphed in normal condition.*

The T variation of just 10 centigrade, corresponding to a percentage in this study between 3% and 5%, leads to a UTS reduction that could reach even 13% passing from 290 to 300°C, with a parallel elongation increase of 50%. This means that, from a production procedural point of view, the temperature setting of the furnace must be maintained within a tight tolerance. From a more metallurgical point of view this phenomenon hides a significant material responsiveness to the temperature applied for a certain time. To have a deeper comprehension, metallographic analysis was carried out on specimens that underwent different stress relieves.

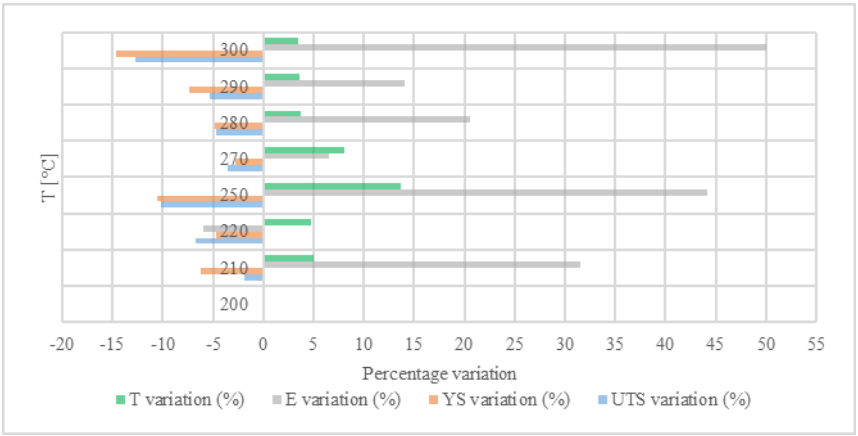

Figure 37: *mechanical properties variation in percentage in relation to the temperature variation. The graph highlights the material sensitivity to the temperature applied.*

Temperature [°C]	Temperature percentage variation [%]	UTS percentage variation [%]	YS percentage variation [%]	E percentage variation [%]
200	-	-	-	-
210	+5	-2	-6	+32
220	+5	-7	-5	-6
250	+14	-10	-10	+44
270	+8	-3	-3	+7
280	+4	-5	-5	+21
290	+4	-5	-7	+14
300	+3	-13	-15	+50

Table 10: *mechanical properties variation in percentage in relation to the temperature variation.*

Starting from the comparison between not heat treated and SR_160 samples, polished and etched sections perpendicular and parallel to the building direction (here called respectively as XY and Z directions) were analysed with optical microscopy.

As it can be seen in Figure 38, not heat treated (a, b) and SR_160 (c, d) sections are characterized by the same microstructure. This is the main reason why no significant differences were noticed on mechanical properties.

Another important aspect is the evident microstructural difference between Z section (Figure 38c,d) and XY section (Figure 38e,f). As anticipated in paragraph 2.6.1, the not heat treated or stress relieved printed parts are not isotropic due to due nature of SLM process itself. This is clearly visible in the microstructure where, Z sections are characterized by meltpools, while on XY sections the LASER tracks are distinguishable. This phenomenon explains the slight deviance between XY and Z specimens mechanical properties. XY samples exhibit in general higher elongations, thanks to the easier planes sliding along sample axis.

SR_160 specimens were further analysed with scanning electron microscope (SEM). Figure 39 shows the microstructure on a Z section in correspondence of the melt pool boundary, where the Si rich network (lighter areas) start dissolving and desegregate (Figure 39b) due to the local remelting and to the slightly slower solidification. The melt pool core along Z direction (Figure 39c) is fine and characterized by oriented columnar α-Al matrix (grey areas) surrounded by Si rich network. This elongated Al cells, if observed on the plane perpendicular to building direction (XY section) appear equiaxed (figure 40c).

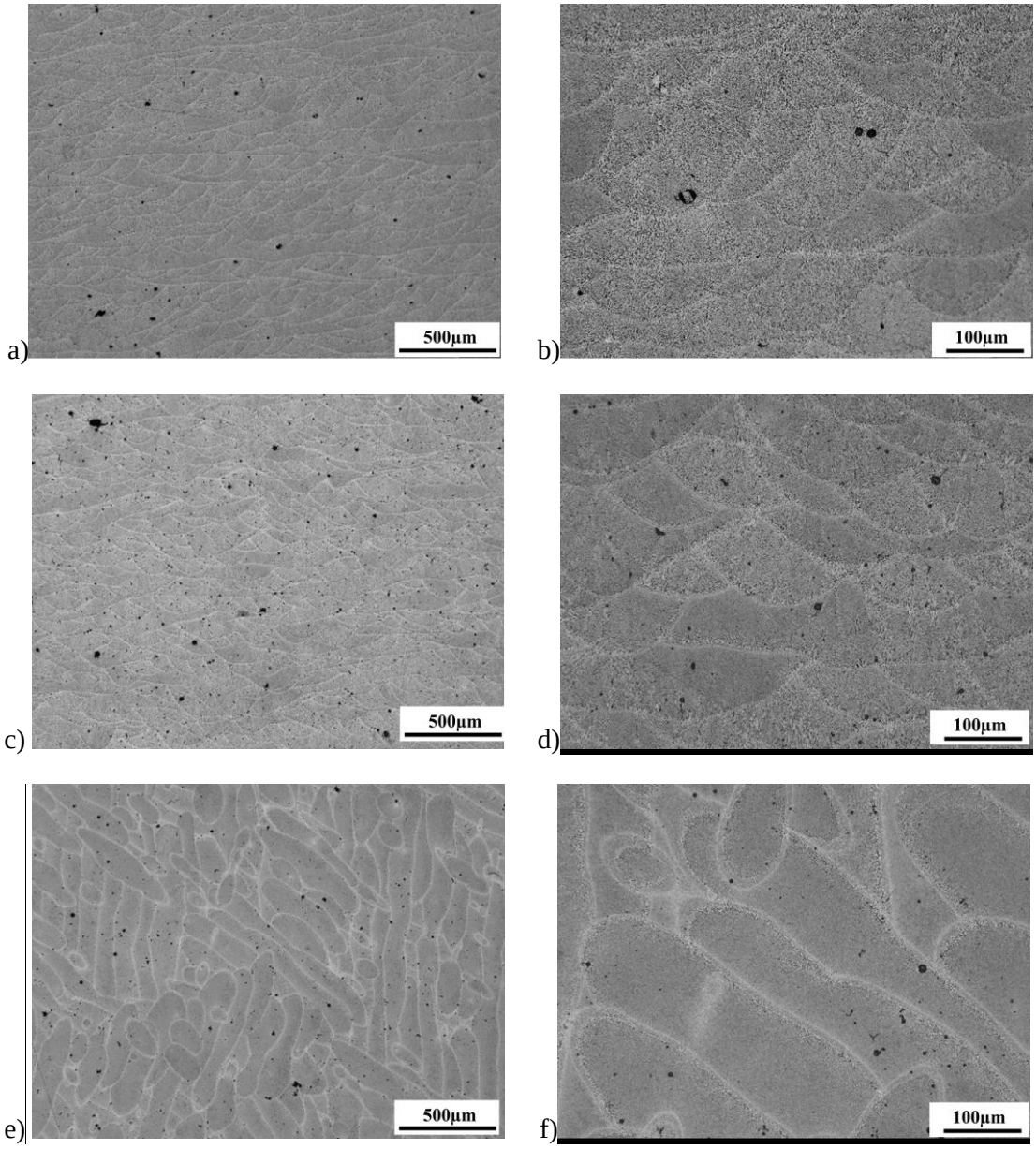

Figure 38: *comparison with optical microscope of microsturcures of not heat treated (a,c) and SR_160 (b,d,e,f,) specimens along Z direction (a-d) and XY direction (e,f)*

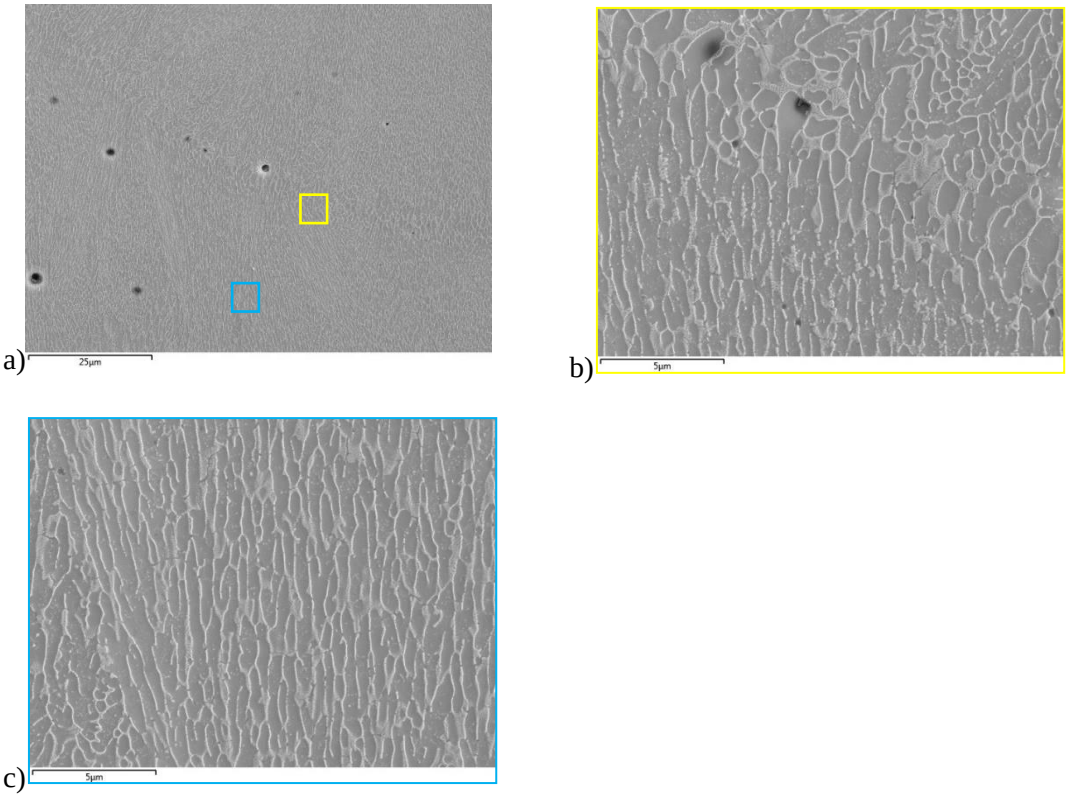

Figure 39: *SEM images at different magnifications of microstructure along Z direction. a) 100x; b,c) 500x. The microstructure is characterized by α-Al matrix (grey area) surrounded by columnar interdendritic Si-network (lighter areas).*

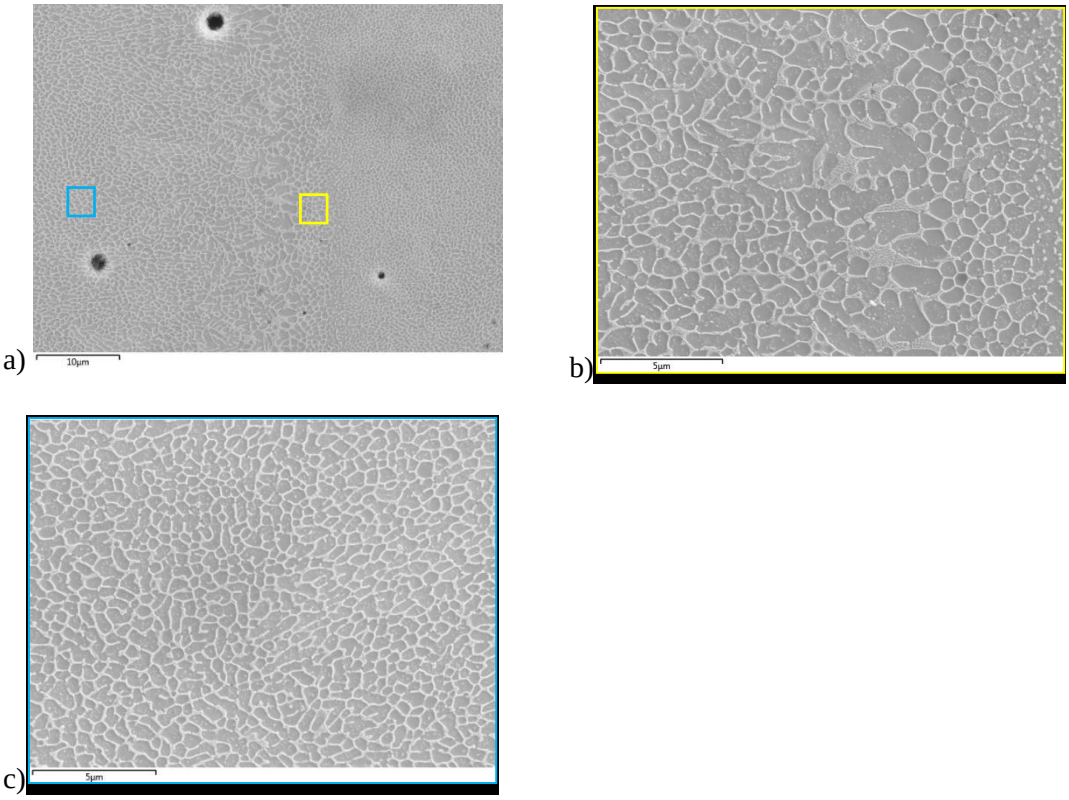

Figure 40: *SEM image at different magnifications of microstructure perpendicular to building direction.*

A deeper analysis was carried out on stress reliefs at different temperature, to evaluate the actual effects on microstructure. Taking stress relieved at 160°C for 6 hours specimens as a direct comparison, SR at 270°C and 290°C for 2 hours were considered. XY and Z sections were polished, etched and analysed with optical microscopy and SEM.

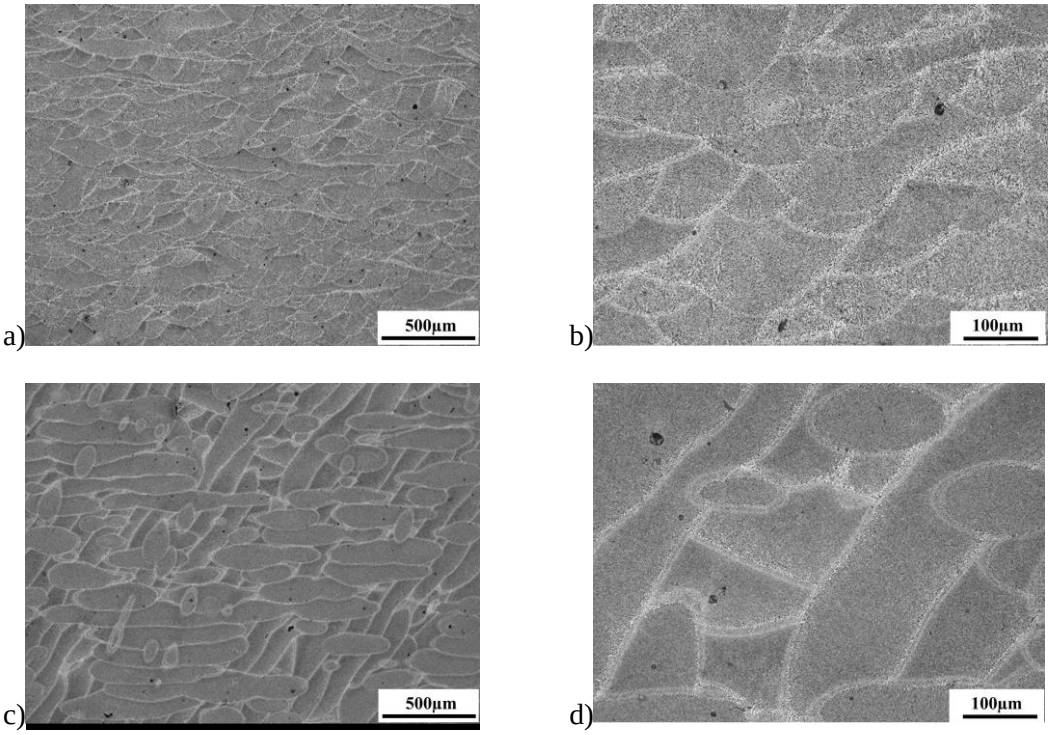

Figure 41: *microstructural analysis with optical microscope of specimens treated with SR_270 in Z (a,b) and XY (c,d) directions. a,c) 50x; b,d) 200x*

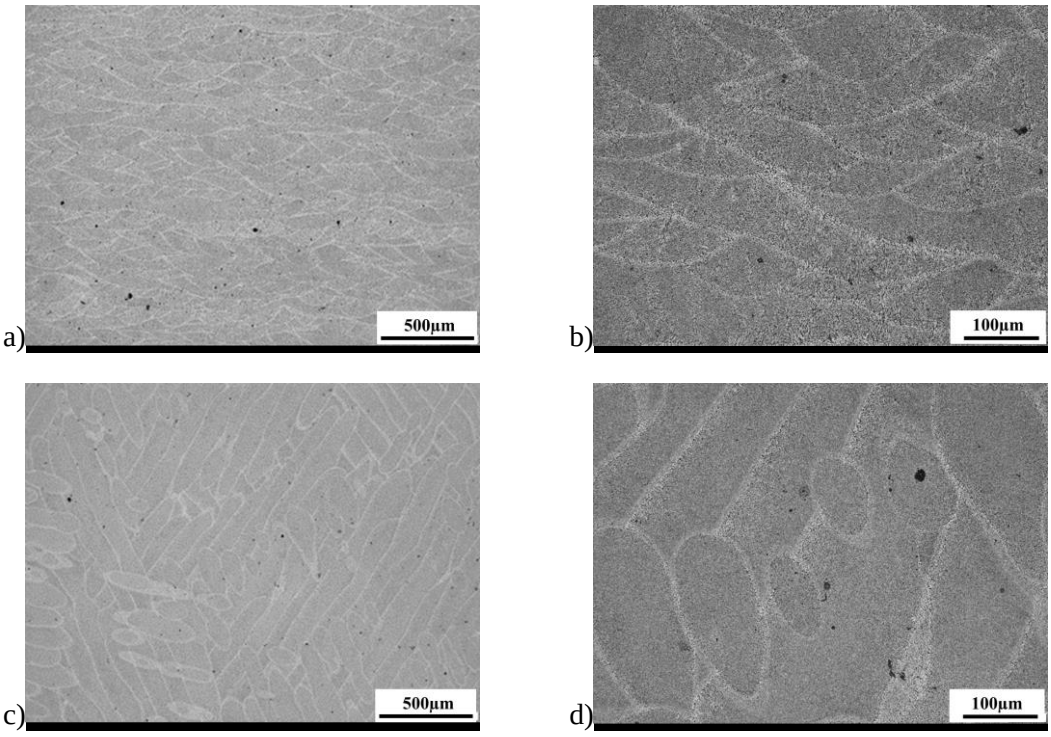

Figure 42: *microstructural analysis with optical microscope of specimens treated with SR_290 in Z (a,b) and XY (c,d) directions. a,c) 50x; b,d) 200x*

With optical microscope the microstructures at 270°C (Fig.41) and 290°C (Fig.42) are similar to the SR_160 specimen (Figure 38a, b). Melt pools and laser tracks are still visible. The only difference is that at 290°C melt pools boundaries are not as pronounced as at lower temperatures, starting slightly to dissolve.

To better appreciate the differences, SEM analysis was carried out.

Starting from spotting the differences between SR_160 (figure 39c) and SR at 270°C for 2 hours (figure 43e) on Z section, it can be noticed that, moving from 160°C to 270°C heat treatment temperature, the Si rich network surrounding super-satured Al matrix starts to break becoming less compact. Moreover, microstructure is in general coarser by the application of a higher temperature. This may be the root cause behind the material softening with higher elongations and lower UTS and YS. As reported by E.Amir et al. in their study [88], the rupture of the interconnected Si particle may give more mobility to dislocations, reducing the Hall-Petch hardening effect of not heat treated or SR_160 specimens.

This phenomenon is even more evident with application of 290°C. Regarding this, figure 43 shows the comparison between specimens microstructure stress relieved at 270°C and 290°C. Sections were made along the building direction Z at the same magnification. What was scarcely appreciable with optical microscopy becomes noticeable on SEM images. By increasing the heat treatment temperature of just 20 °C, the microstructure undergoes an evident changing. The Si network both at the melt pool boundary and core is broken and Si particles are even coarser. In parallel, UTS and YS decrease in favor of an elongation increase of 45%.

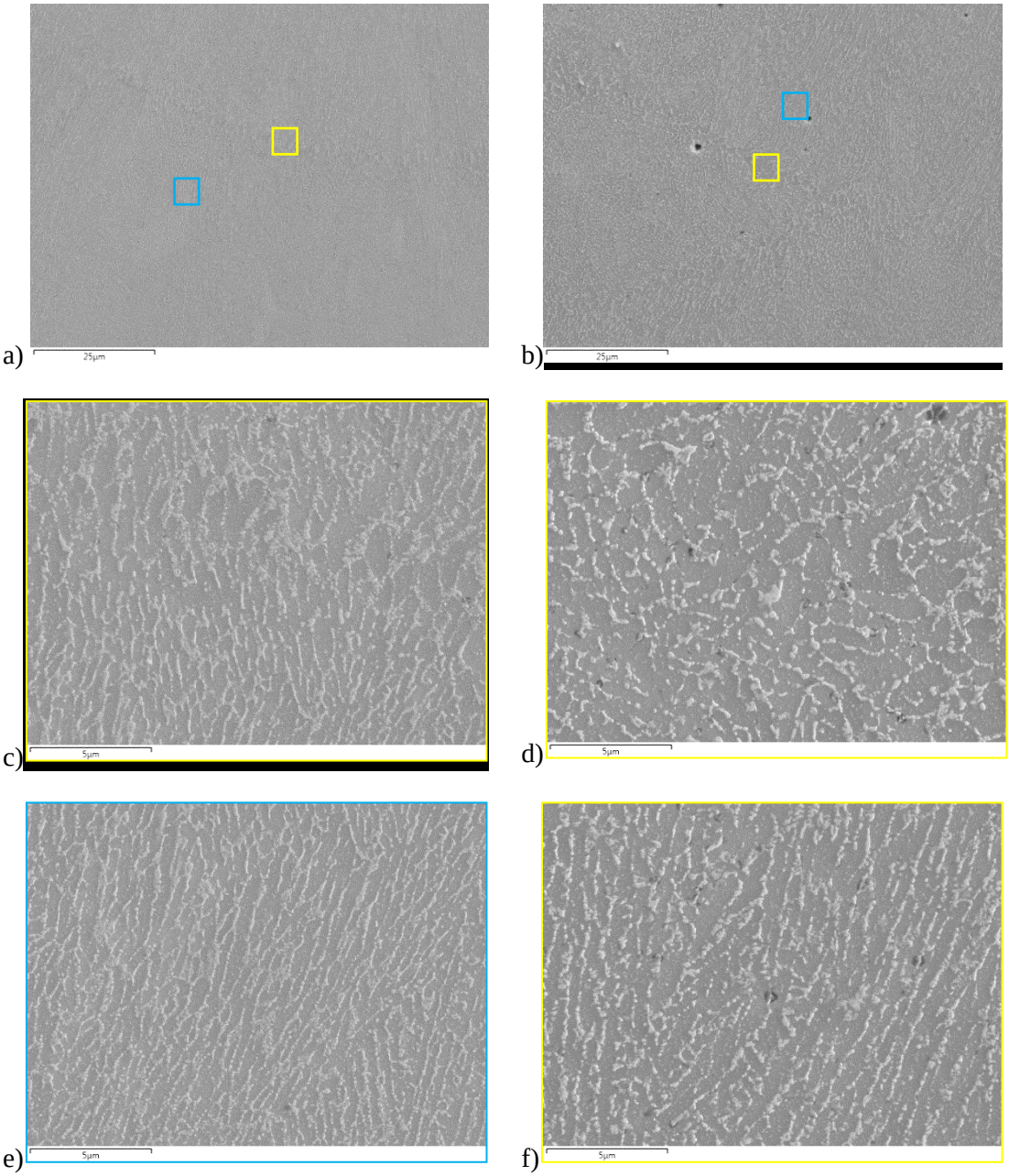

Figure 43: *SEM analysis of microstructures of specimens treated with SR_270 (a,c,e) and SR_290 (b,d,f). Si-network interruption passing from 270°C to 290°C of SR especially at melt pool boundaries (c,d). a,b) 100x; c-f) 500x.*

4.1.2 T6 investigation

The study on SR heat treatments highlighted the strong material anisotropy due to the SLM process itself for which the material is added layer by layer. Given the need of producing components with equal mechanical properties along both Z and XY directions, T6 heat treatments were investigate. The T6 tested are listed in Table 6, already presented in chapter 3.3.

Once again, absolute results cannot be disclosed due to industrial policies. Therefore, UTS and elongation results were normalized in relation to the mechanical properties obtained on not heat-treated Z specimens.

Figure 44 shows the aging curves obtained with the different solution heat treatments. The aim of this study was to find the peak of aging treatment. As can be observed, from 4 to 8 hours of aging duration, UTS are quite stable in a small values range regardless the duration of the former solution heat treatment. Nevertheless, T6_2 and T6_3 exhibit a decreasing trend with the increase of aging duration, meaning that the hardening peak was already overtaken. The hardening process is given by the precipitation of secondary phases, represented in this case mainly by Mg_2Si phase, that within a certain precipitates dimensions, deform the crystal structure of the Al matrix, hindering the dislocation movement.

An effective hardening is obtained within a certain aging duration window. This because, if the aging temperature is maintained for a not sufficient time, precipitates do not achieve the opportune dimension to significantly deform the planes of crystal lattice. On the other hand, over the hardening peak, precipitates start coarsening, thus reducing the hardening effect.

Over 8 hours of aging, UTS results deviate appreciably one from each other. T6_2 and T6_3 led to a steep tensile strength drop, while T6_1 reaches its peak hardening.

T6_4 was tested as a compromise between T6_1 and T6_2 in terms of solution heat treatment duration and aging temperature. Water quenching was performed at room temperature to compensate for the higher aging temperature applied compared to T6_1. T6_4 led to the achievement of the highest UTS, with the foreseeable drawback of excessive deformations due to water quenching at low temperature. Thin walls or cantilever parts are typical in additive manufacturing since design freedom is one of the main advantages that make this technology competitive in respect to traditional technologies as casting. This is the main reason why deformations due to heat treatment were not acceptable and T6_4 was not considered for any further study.

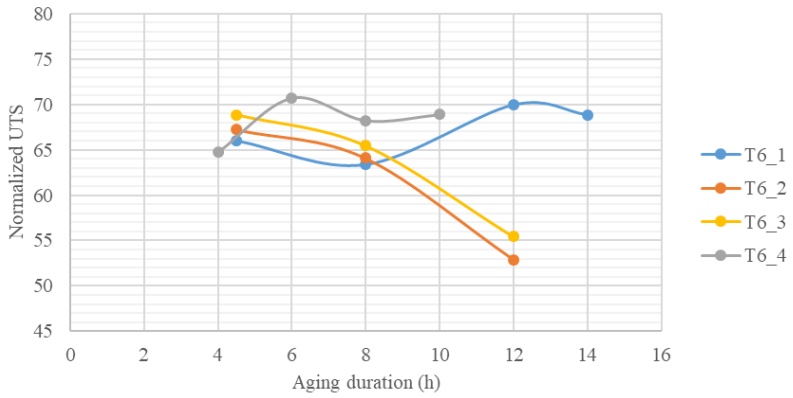

Figure 44: *Aging curves obtained with the different T6 applied*

4.2 Rotating bending fatigue tests of stress relieved specimens

4.2.1 Influence of printing direction and surface condition

In this study, the most promising heat treatment evaluated in the preliminary analysis (see previous paragraph) was further tested on a single point rotating bending fatigue machine. For this dynamic analysis the specimens underwent stress relief at 160°C for 6 hours.

First of all, machined specimens built in XY and Z directions were tested to quantify the effect of printing direction on fatigue resistance. In this regard, 16 bars for each direction were machined to final fatigue specimen geometry and tested as described in paragraph 3.2.4. Absolute results cannot be disclosed due to industrial policies. Therefore, in this study all the results were normalized in relation to the mean UTS value of as printed specimens built in Z direction.

As described in paragraph 3.2.4, staircase method was applied for rotating bending fatigue tests, with a load step of 10 MPa, testing more or less 10 to 16 specimens each time. The staircase method, by definition, is used to find the fatigue limit by testing the material in the nearness of the limit itself.

Hence, a complete Wöhler curve cannot be graphed, since specimens had never been tested at high loads, so within low cycle fatigue region.

Wöhler curve can be described by the Basquin law, defined as follows:

$$\sigma^{k_\sigma} \cdot N = cost \tag{21}$$

where σ is the load, N the number of cycles and k_σ is the slope of the curve in σ-N curve.

In a double logarithmic scale, the fitted curve is represented by a linear plot with double slope. For casting aluminium, FKM guidelines report a slope k_σ equal to 5 before the knee point corresponding to 10^6 cycles, and $k_{D,\sigma}$ equal to 15 after this knee point (Figure 45) [89].

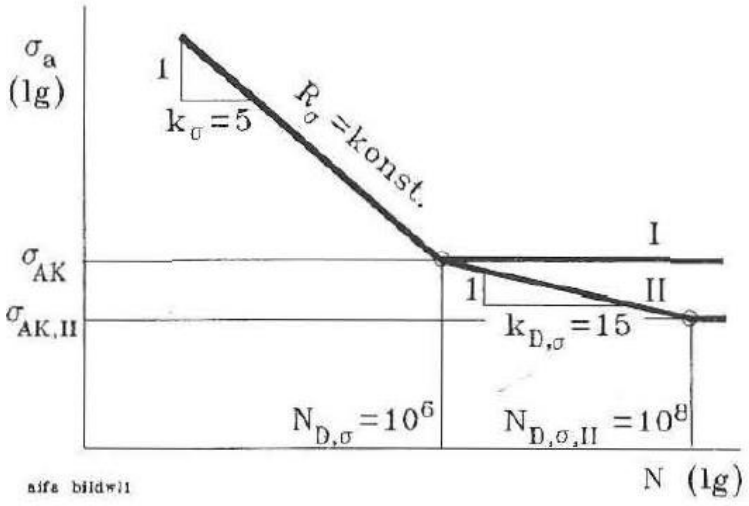

Figure 45: *log-log σ-N graph with k_σ slope as defined in FKM guideline for casting aluminum.*

In this research, results are displayed in a log-log graph to have a direct comparison between the different testing campaigns. Despite the limited data at disposition, as can be seen in graph 46, it appears clear that slopes k defined in FKM for cast aluminium (dashed lines) cannot be applied in AlSi10Mg additive manufactured curves. Looking for example at the results obtained with XY

and Z machined specimens, the application of $k_\sigma = 5$ does not fit correctly the present data, with an overestimation of the fatigue resistance at lower N. To the same conclusion came also other researchers as Romano et al. [90], who found curve slopes between 6 and 7,7.

Focusing on the fatigue values, this first rotating bending campaign lighted out that XY machined specimens have a fatigue limit about 70% higher than the one of Z machined specimens.

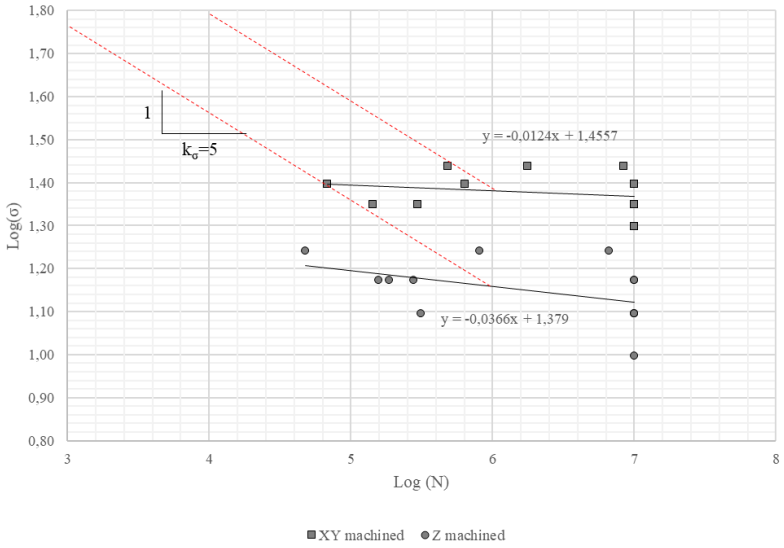

Figure 46: *σ -N curves obtained from rotating bending fatigue tests on XY and Z machined. The red dashed lines represent the curve approximation according FKM guideline for casting aluminium.*

After this first campaign, the second comparison was focused on the influence of surface roughness and contour on fatigue resistance. Therefore, specimens built in Z direction were tested both in the as printed and in the machined conditions. XY as printed specimens were not considered in this study due to supports in the gauge region that could alter the local surface roughness and could introduce different notch factors. Results are graphed in Figure 47. As printed samples show a significant lower fatigue resistance then the machined ones. As easily predictable, surface roughness severely and negatively affects fatigue behaviour leading to a reduction of nearly 50% of fatigue limit.

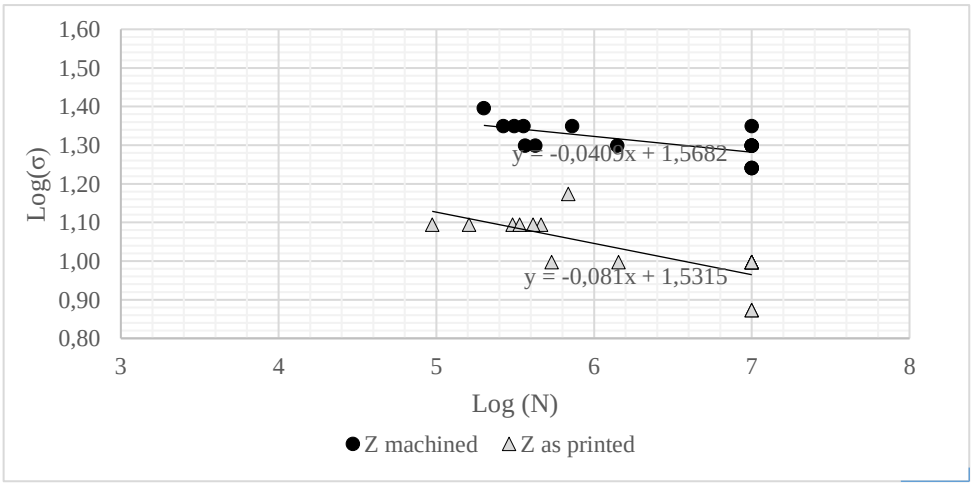

Figure 47: *Comparison between fatigue results obtained on Z machined and as printed specimens.*

For a deeper comprehension of the phenomenon, surface fractures were further analysed with stereo microscope. While in machined specimens crack initiation is located in correspondence of a defect (figure 48b, d), in as printed samples, fatigue crack origin is not punctual and traceable to a single point, but it is wider and shifted towards the surface (Figure 48a, c). Therefore, it can be stated that as printed surface has higher impact on fatigue resistance than single defects. This behaviour is also promoted by the test nature, since rotating bending mainly stresses the outer specimen surface than the core, as happens, on the contrary, in axial fatigue tests. This campaign was not completed (11 specimens were tested instead of 16) due to the achievement of the full scale of rotating bending machine during the testing of as printed samples.

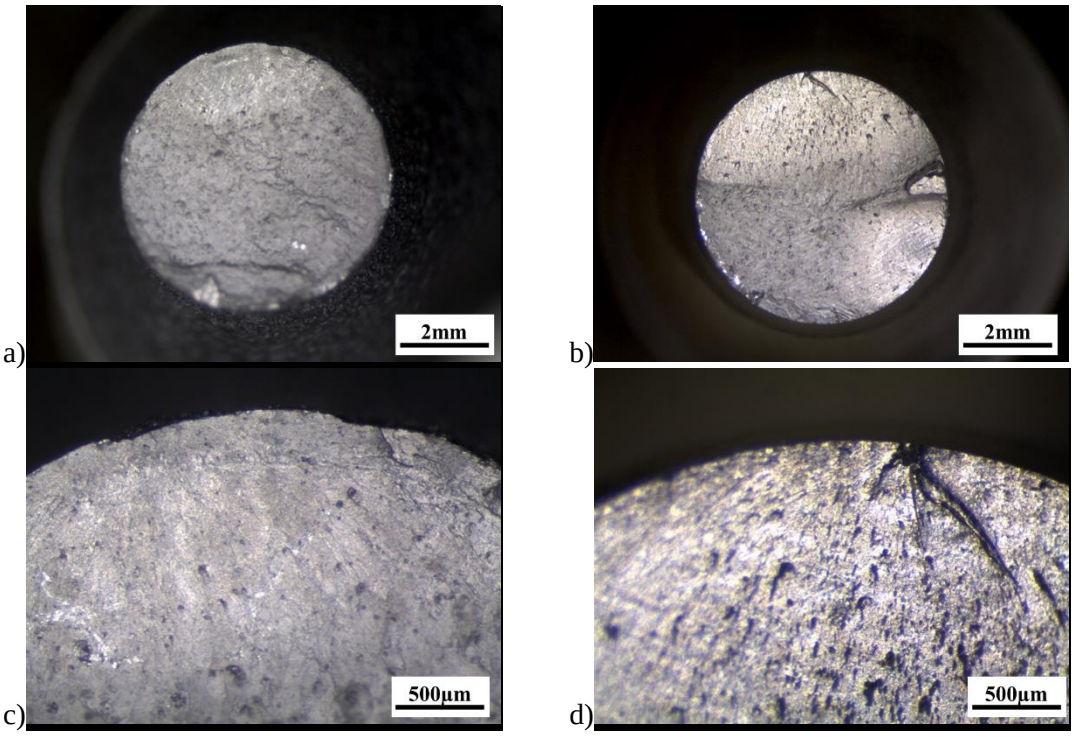

Figure 48: *Fracture surfaces of not machined (a,c) and machined (b,d) rotating bending fatigue specimens.*

Another important aspect evaluated in this analysis refers to the position of each single specimen along the build plate. The job layout was mapped according to failures and runout obtained during the rotating bending fatigue tests, regardless the samples condition (machined or as printed).

Figure 49 displays the job layout scheme. The dashed line is representative of the build plate centreline, while green and red circles represent respectively runouts and failures of each specimen. The blue arrows show the direction of the inert gas flow. What it was observed is that most part of the failures (about 95%) occurred on the half of the building plate corresponding to the gas flow outlet. At the same time, nearly all of the runouts are concentrated towards the argon inlet. The reason behind this phenomenon is related to the capability of the gas flow to swipe towards the build plate outlet the spatter generated during the laser scanning. Actually, as stated in chapter 2.4, spatter is composed by sort of drops of melted powder that are ejected from the melt pool and carried away by the inert gas. Therefore gas flow rate optimization is important, even though the removal of all the spatter is almost impossible. Spatter that settles on the powder bed may cause defects in the printed part due to a not correct melting of the subsequent layers and to the fast oxidation.

The fact that almost all the failures occurred towards the argon outlet may be due to the higher defects presence in the printed parts caused by spatter that accumulates along the gas flow direction.

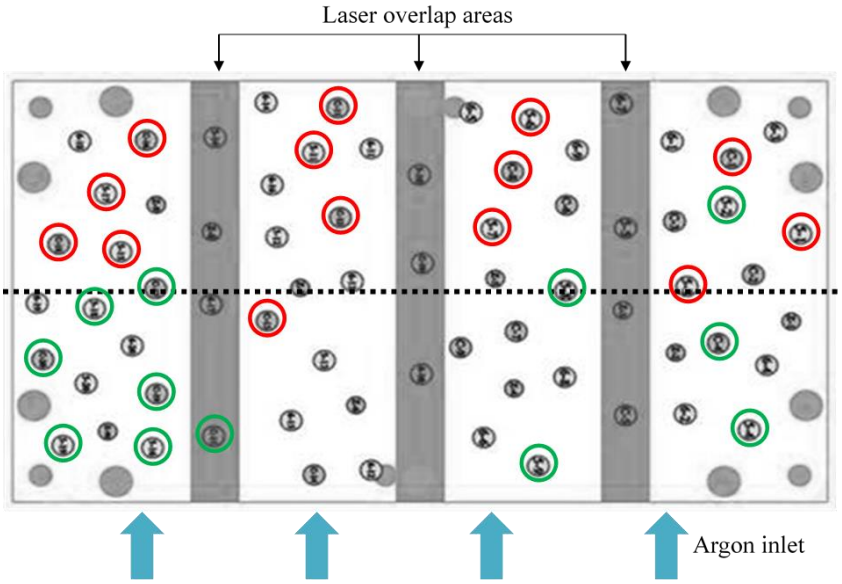

Figure 49: *JOB scheme with positions of KO (red) and runout (green) fatigue specimens.*

To evaluate this phenomenon image analysis was carried out on vertical sections (parallel to specimens axis, Z direction) of runout and failure samples. In detail, a total of 2 runout and 4 failure machined specimens printed respectively in argon outlet and inlet areas were considered.

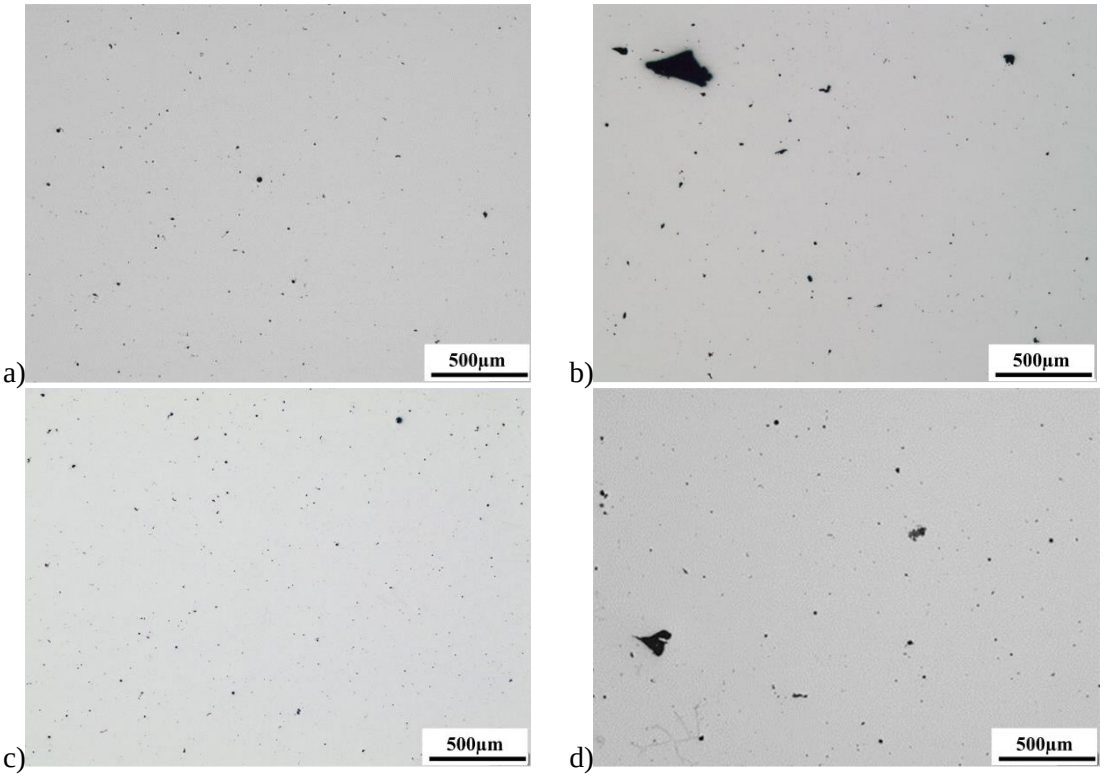

Figure 50: *optical microscope analysis of vertical sections of fatigue RUNOUT (a,c) and KO(b,d) specimens. Magnification 50x.*

What was noticed is a slight increase in defect concentration in failure specimens (built towards the argon outlet). As can be seen in figure 50, runout specimens (a,c) sections exhibited small and mainly spherical defects as gas porosities, while failure specimens (b,d) had in addition irregular defects with significant dimensions, typical of a not correct melting (lack of fusion). Anyway, further studies were carried out to have a quantitative (not only qualitative) analysis.

Therefore, starting from the defect evaluation at the fatigue crack initiation, a trigger dimension value was searched in order to highlight only those defects that could bring to fatigue test failures. In this study only machined specimens were considered, to not introduce the surface roughness variable, hence, to have the security that fatigue starts from inner defect. All the fracture surfaces were observed with stereo microscope and originating defects sizes were collected. In this regard, defect size was measured as the defect projected area to a XY plane, so parallel to the fracture surface.

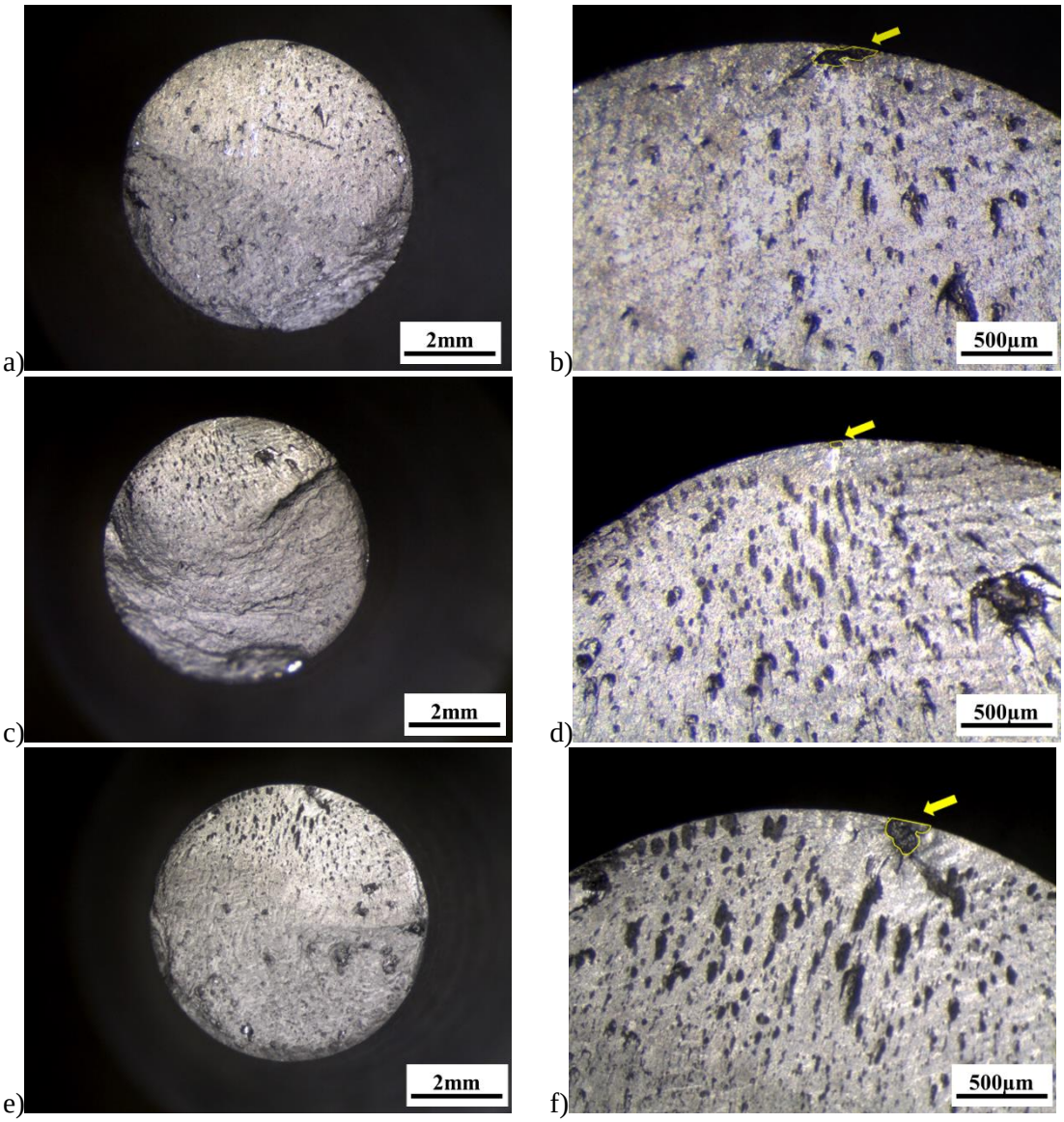

Figure 51: *Fracture surfaces at stereo-microscope of KO machined fatigue specimens with indication of defects at fatigue crack initiations.*

Figure 51 shows some of the fracture surfaces of Z machined specimens with indications of the originating defects and the corresponding measured area, while Table 11 report the estimated defects dimensions for each failure specimen. Starting from these results, the trigger defect dimension was established as the smallest defect area observed and corresponding, in this study, to samples labelled as Z-machined-2. Therefore, an area of about 2000 μm^2 was considered as the minimum defect area that could bring to the specimen failure. Assuming this, all defects detected by image analysis in sample sections parallel to Z direction were distinguished in terms of dimension between those smaller than 2000 μm^2 and bigger than 2000 μm^2. Then, considering the same region of interest for all the sections, the defects greater than 2000 μm^2 were simply counted and subdivided in frequency classes. This procedure was studied to correlate the general inner quality of a printed part, which is definable by simply sections, to a possible predictive fatigue limit without the help of CT scans.

Actually, CT scan is advantageous since is a non-destructive testing. On the other hand, though, is generally a high expensive analysis that requires extremely high resolution to intercept the relatively small defects typical of SLM technology. Hence, to overcome the problem, it could be reasonable printing samples in the proximity of a specific printed part region of interest that could predictive information on the dynamic behaviour of the component.

Specimen Label	Originating defect dimension (μm^2)
Z-machined-1	22400
Z-machined-2	**2100**
Z-machined-3	22000
Z-machined-4	67000
Z-machined-5	12300
Z-machined-6	13400
Z-machined-7	20000
Z-machined-8	4500
Z-machined-9	15200
Z-machined-10	12500

Table 11: *Dimensions of defects at fatigue crack origin of Z machined specimens. Z-machined-2 sample has the smallest defect on fracture surface*

By image analysis, with the help of Olympus StreamBasic Software, it was possible the collection of the data corresponding to every single defect detected in section. Each defect was classified in terms of dimensions and morphology, hence circularity defined as follows:

$$circularity = \frac{4\pi A}{P} \tag{22}$$

where A is the measured area and P is the perimeter.

Nevertheless, in this study only the dimension was taken into account. The outcome of this analysis underlined a major presence of defects with consistent dimension (greater than 2000 μm^2) in failure specimens. In detail, frequency classes of defect dimension were considered and then translated in percentage frequency. Graph in figure 52 exhibits the percentage frequency of defects found in Z machined specimen that achieved or not (KO) the runout condition. The grey area highlights the results greater than trigger dimension. As expected, almost the totality of the defects is small in size. Moreover, KO specimen sections were characterized by a greater number of defects bigger than 2000 μm^2 quantifiable as 0,16% of all the defects detected. This number

drops down to 0,04% when it comes to consider the runout samples, confirming that defect dimension is one of the leading factors in the determination of the fatigue resistance.

As demonstrated before, almost all the failures occurred towards the argon outlet, where there is a higher probability of spatter deposition, and the samples sections are characterized by a greater number of defect of significant dimensions. That means that the defects that may lead to a fatigue failure are surely related to a not proper powder bed cleanliness from the spatter that easily accumulates toward the gas flow outlet.

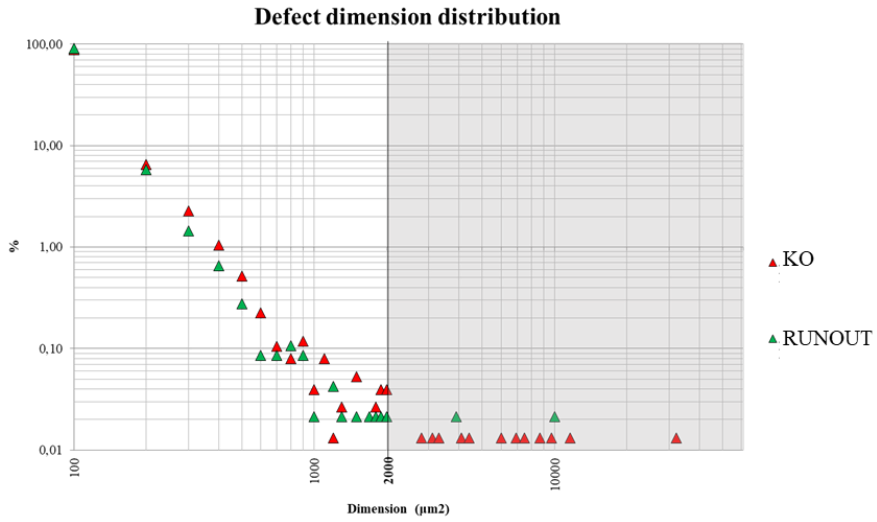

Figure 52: *Defect dimension distribution of KO and Runout machiend fatigue specimens with indication of the defect with an area greater than 2000 µm²*

4.2.2 Influence of printing height

In this analysis, influence of printing height was considered to evaluate if dynamic mechanical characteristics would vary along the printing chamber height. Hence, plates and cylinders 285 and 350 mm high were printed. XY and Z machined specimens were respectively extracted at three different distances from the building plate (see paragraph 3.3). Therefore, three regions were considered: A (the farthest to the building plate), B and C (the closest to the building plate).

Figure 53 shows a summary of the results obtained and plotted in a log-log scale. Even in this case, due to industry policies, absolute results could not be disclosed, so they were normalized according to the same method used in 4.2.1, so considering the mean UTS value of as printed vertical specimens equal to 100.

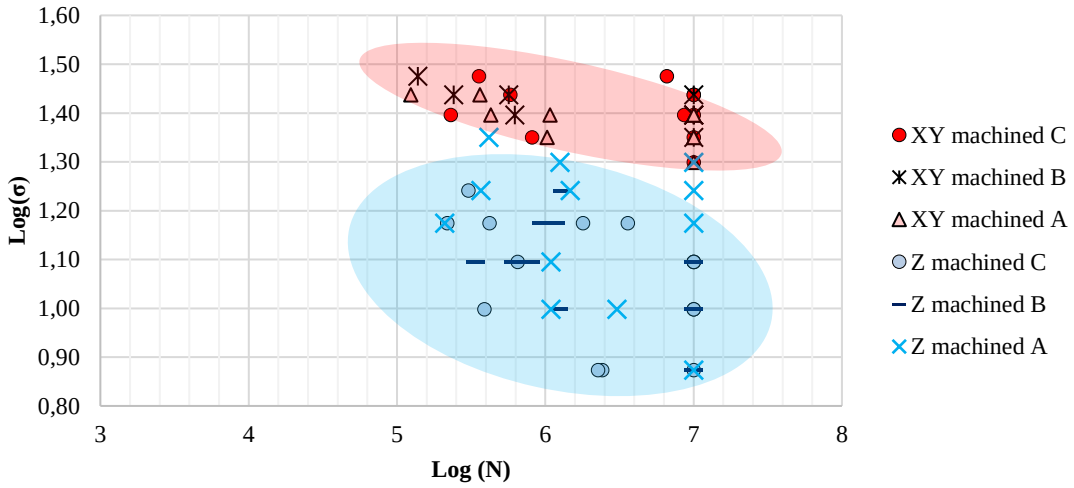

Figure 53: *Rotating bending fatigue results in log-log graph of Z and XY machined specimens at different heights (A,B,C).*

It can be stated that no significant difference in terms of fatigue resistance was observed in the regions corresponding to different heights for the same printing direction. Moreover, this study confirmed what seen in 4.2.1, which is the higher fatigue resistance of XY machined samples in comparison to Z ones.

In addition, Z specimens results (blue cloud in figure 53) exhibit a wider scattering, while XY specimens value have a tight dispersion.

Fracture surfaces were analysed at stereo microscope (figure 54). Starting from specimens corresponding to region A (the highest) it was seen that in general on fracture surfaces of Z samples defects at the origin of the fatigue crack were clearly distinguishable. On the other hand, as it can be seen in figure 54b) and d) XY samples exhibited a fracture surface “cleaner” in terms of defects presence. The black areas in figure 54b) should not be mistaken for defects since they simply represent fretting occurred during rotating bending test.

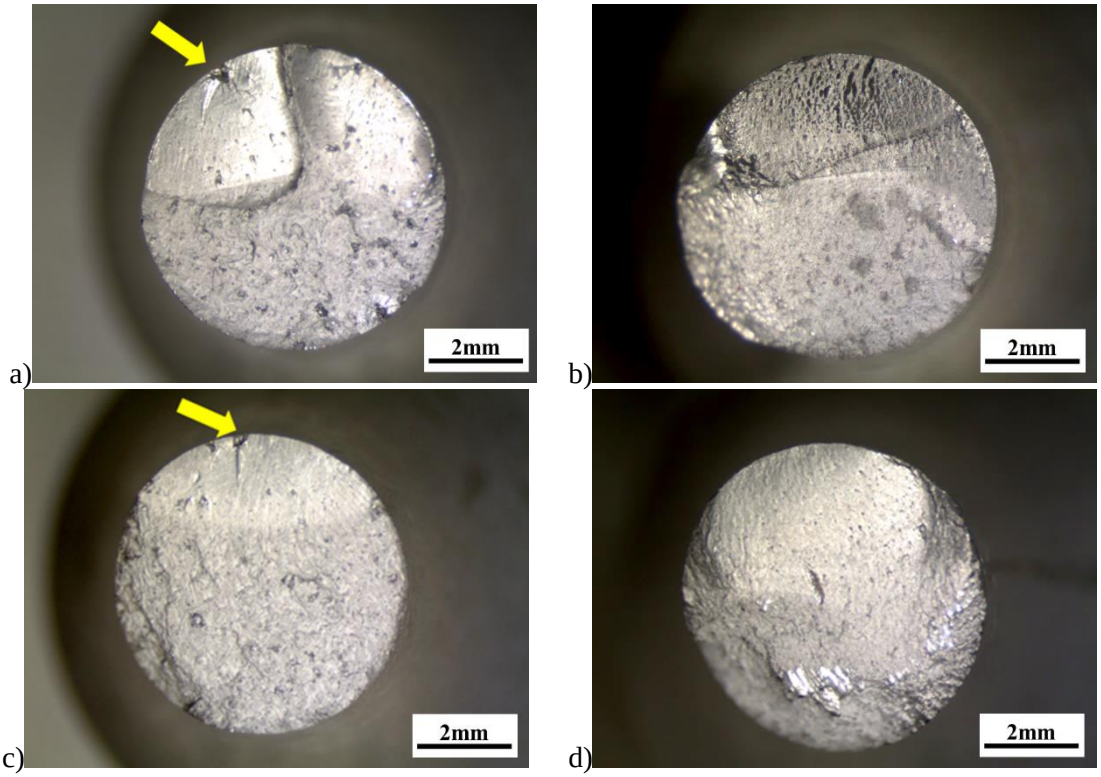

Figure 54: *Fracture surface images at stereo microscope of Z (a,c) and XY (b,d) fatigue specimens with indication of the defects at the fatigue crack initiation. Specimens were printed in the highest region (A).*

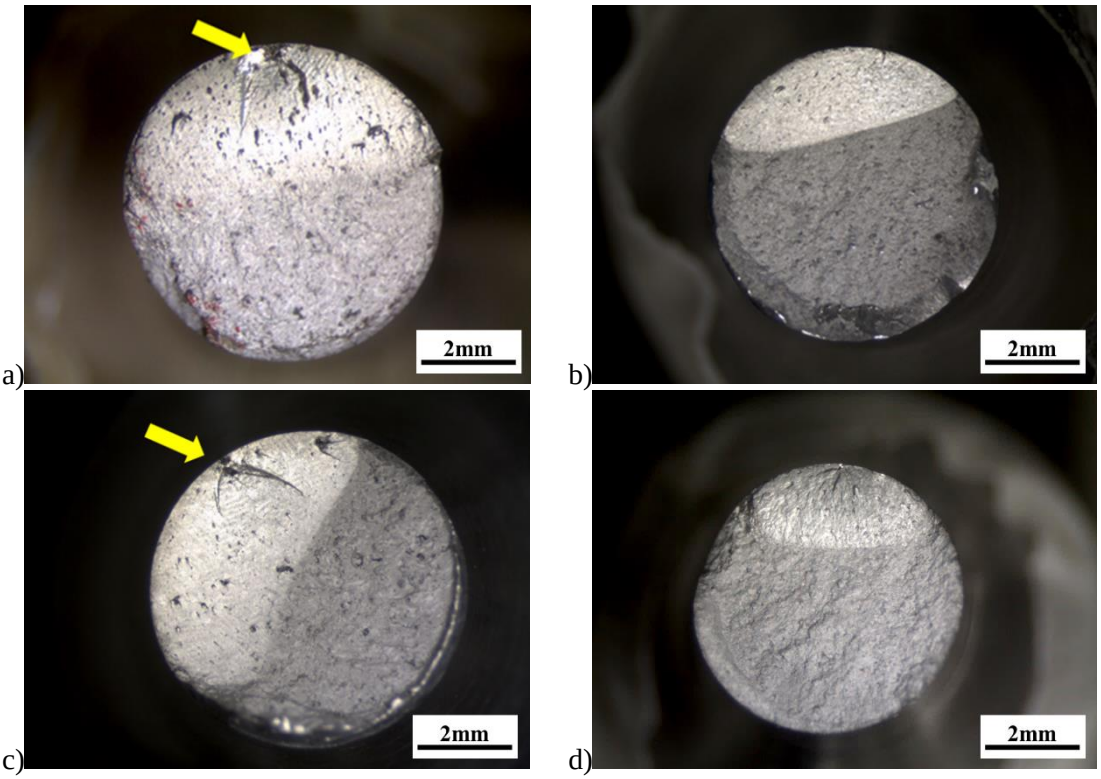

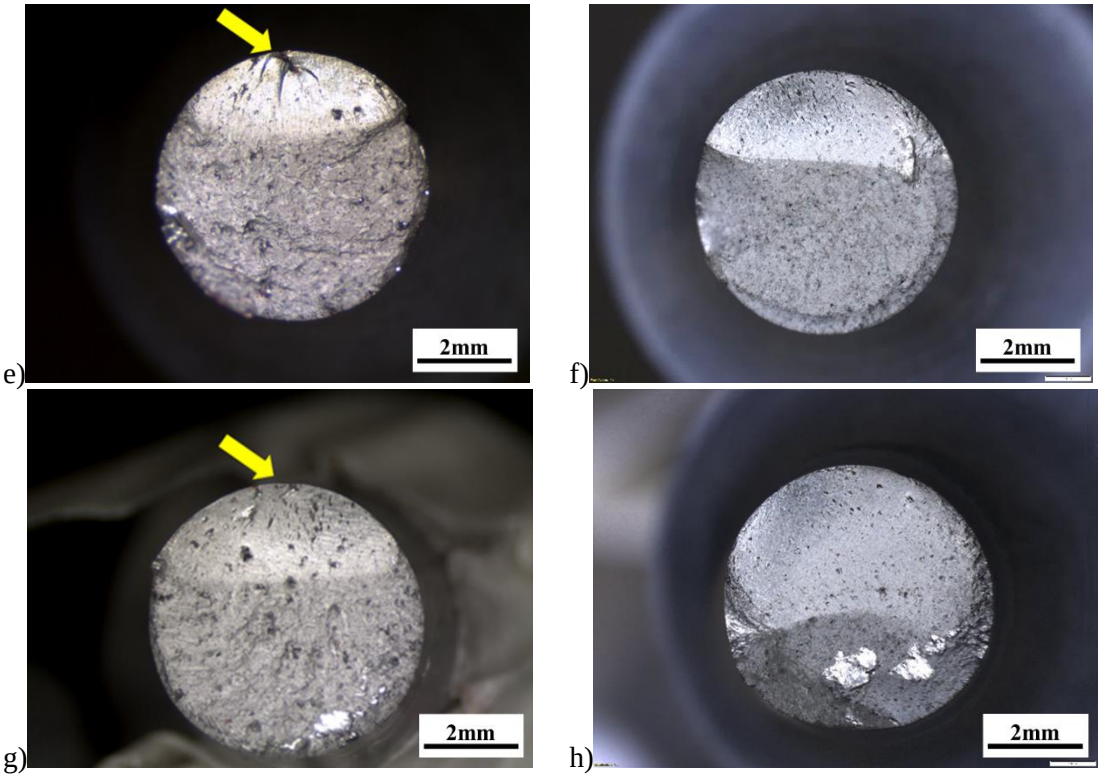

Figure 55: *Frature surfaces analysis at stereo microscope of Z (a.c.e,g) and XY (b,d,f,h) KO fatigue specimens. the specimens were printed at differents heights: B zone (a-d) and C zone (e-h).*

Same conclusion was reached after the visual inspection of fracture surfaces of the remaining specimens (see Figure 55). All the samples were further analysed with SEM. Figures 56, 57, 58 show some of the specimen fracture surfaces.

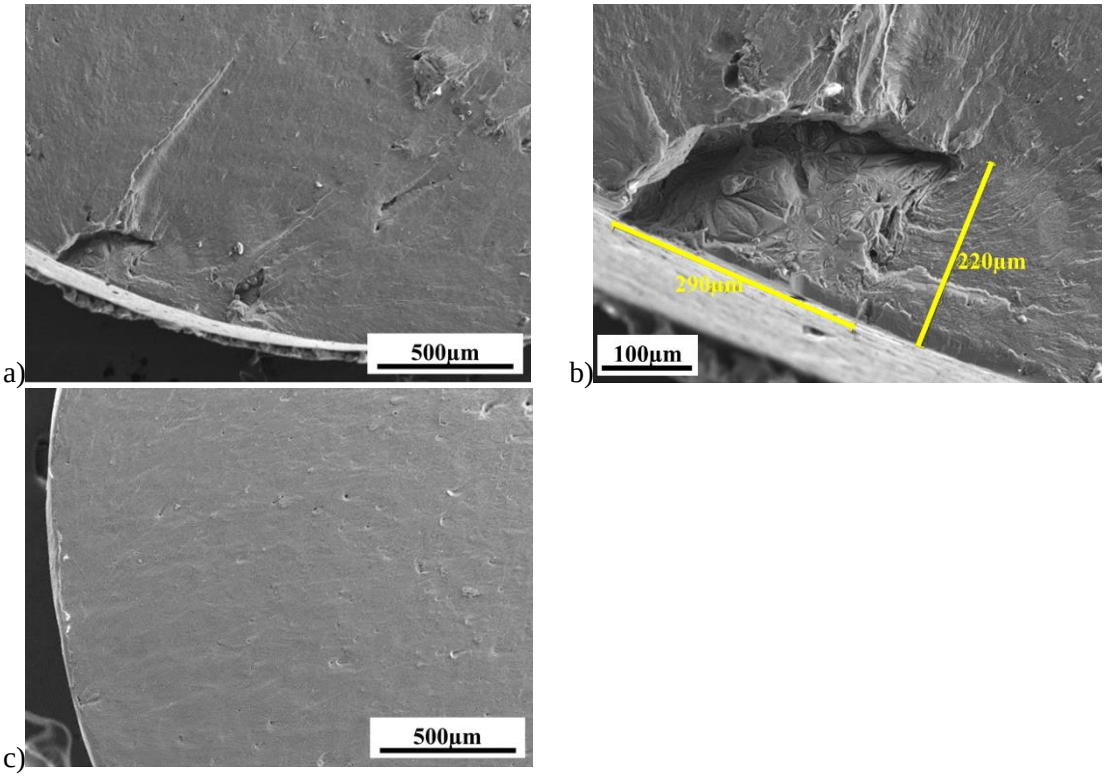

Figure 56: *SEM analysis of fracture surfaces of KO specimens built at A height in Z direction (a 150x,b 500x) and XY direction (c 150x).*

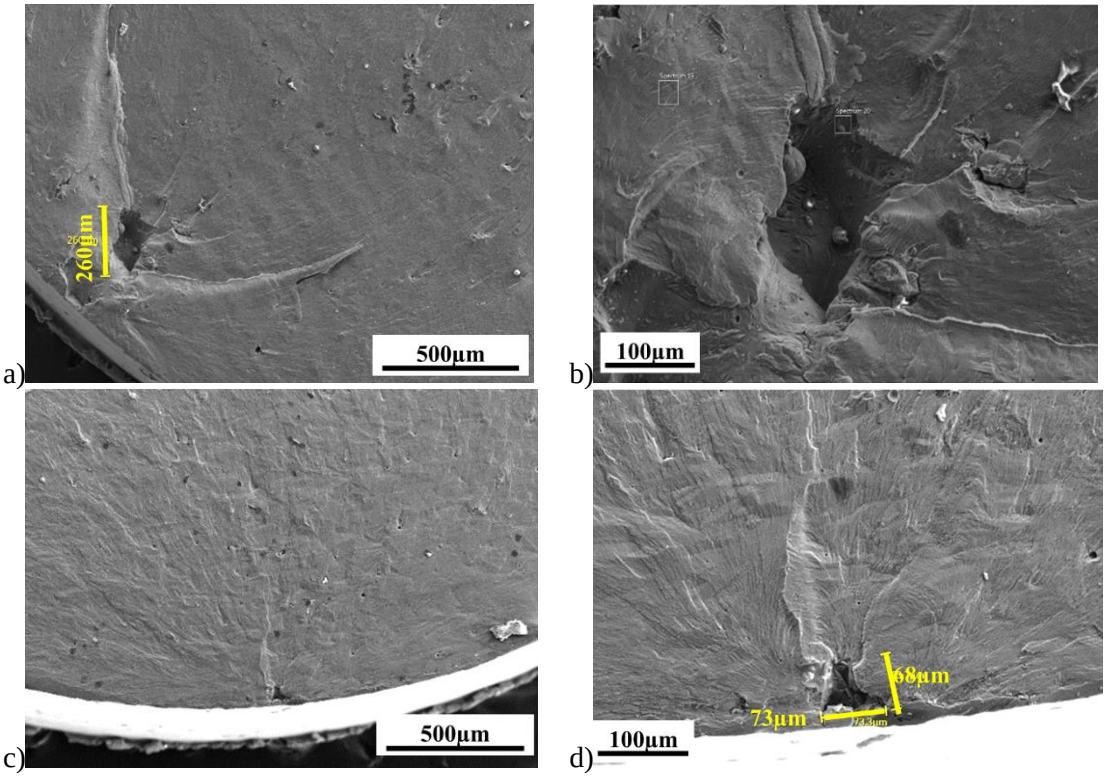

Figure 57: *SEM analysis of fracture surfaces of KO specimens built at B height in Z direction (a 150x,b 500x) and XY direction (c 150x).*

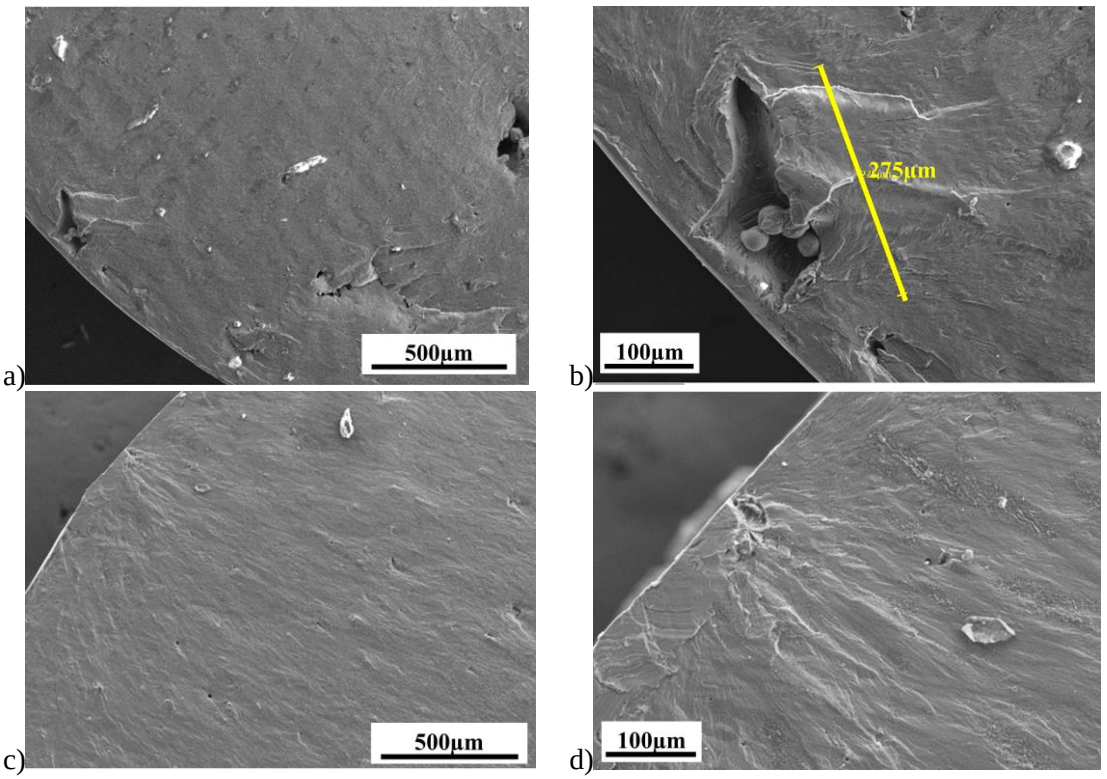

Figure 58: *SEM analysis of fracture surfaces of KO specimens built at C height in Z direction (a 150x,b 500x) and XY direction (c 150x).*

All the Z machined specimens, regardless the relative height, are characterized by defects as lack of fusion, not melted powder or oxidation in correspondence of the fatigue crack initiation with

considerable dimensions (until 0,3 mm). Image 59a, relative to fracture surface of Z machined specimen extracted at C region, shows not only an evident lack of fusion at the fatigue crack initiation, but also a similar defect towards the specimen core. Looking at XY samples, this kind of defect was scarcely detectable. Fracture surfaces were generally smoother without remarkable points at fatigue crack initiation or with much smaller defects than those found in Z sample (see fig. 57c, d).

This fact gave a qualitative explanation to two main facts summarized in the graph in Figure 59:

- The lower fatigue resistance of Z machined specimens, regardless the extraction height (since it was seen to be an invariant)
- The higher dispersion of Z machined samples fatigue results.

This means that printing direction influences fatigue resistance since XY samples were always characterized by a higher fatigue limit, but on the same time, fatigue behaviour of Z parts is strictly linked to the probability of finding defects on the surface corresponding to the notch.

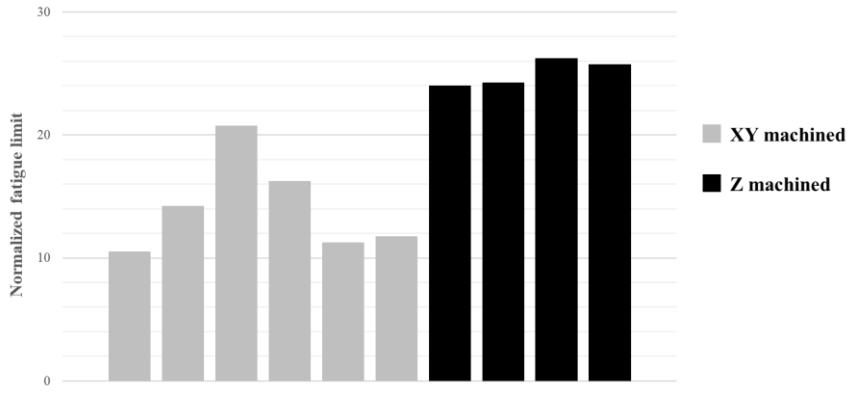

Figure 59: *Normalized fatigue limits (50 percentile) achieved woth Z and XY machined samples.*

For a parallel quantitative comparison between the obtained results, same image analysis done in 4.2.1 was carried out in this study. Therefore, four KO and two runout specimens were sectioned along the Z axis for each condition (Z and XY samples belonging to A, B and C regions). Sections were polished and evaluated in terms of types of defects. In this regard, the same defect size threshold (2000 μm^2) was considered in this analysis to enlarge the statistical base and to evaluate the effectiveness of this method for description of the part fatigue behavior.

Figure 60 shows sections of A specimens built in Z direction, KO (a) and runout (b) and in XY direction (c KO, d runout). It can be stated that KO Z specimen was characterized by defects as lack of fusion, that were not detected in Z runout sections or in almost any of XY specimen (regardless the fatigue test ending). Same conclusion was reached after B and C samples section evaluation (figures 61 and 62).

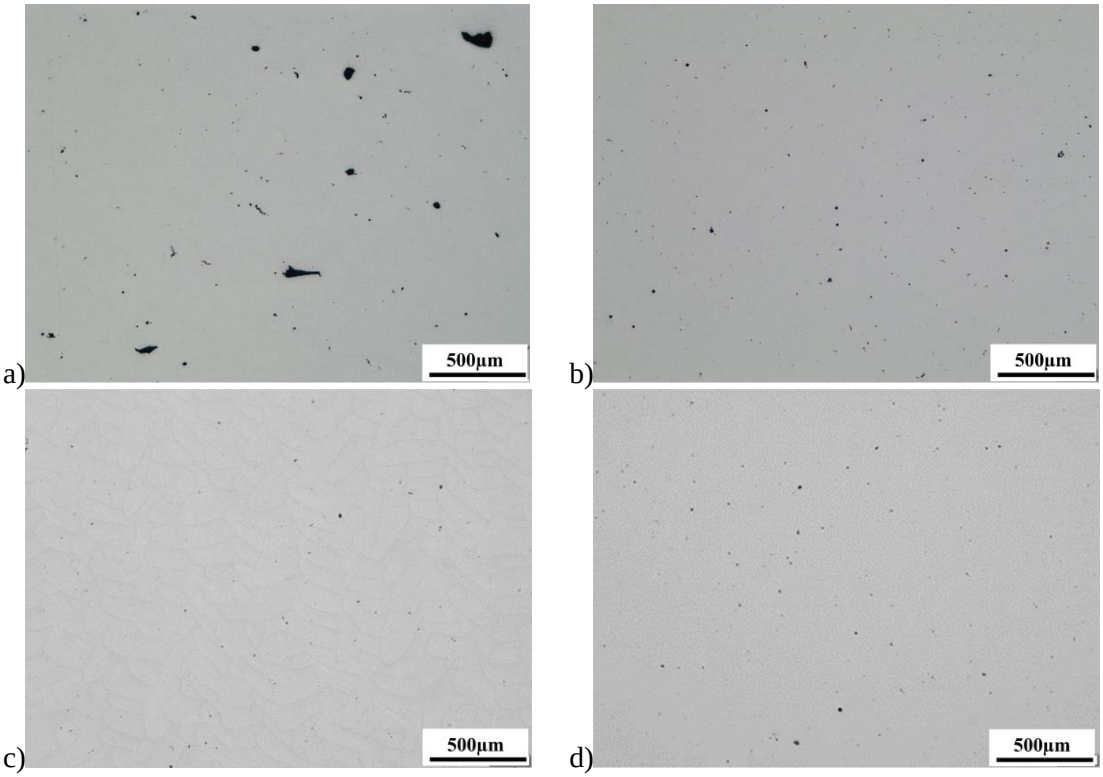

Figure 60: *optical microscope analysis of RUNOUT (b,d) and KO(a,c) specimens sections in A printing height. Magnification 50x. Samples shown in a,b) are built in Z direction, while those in c,d) are XY.*

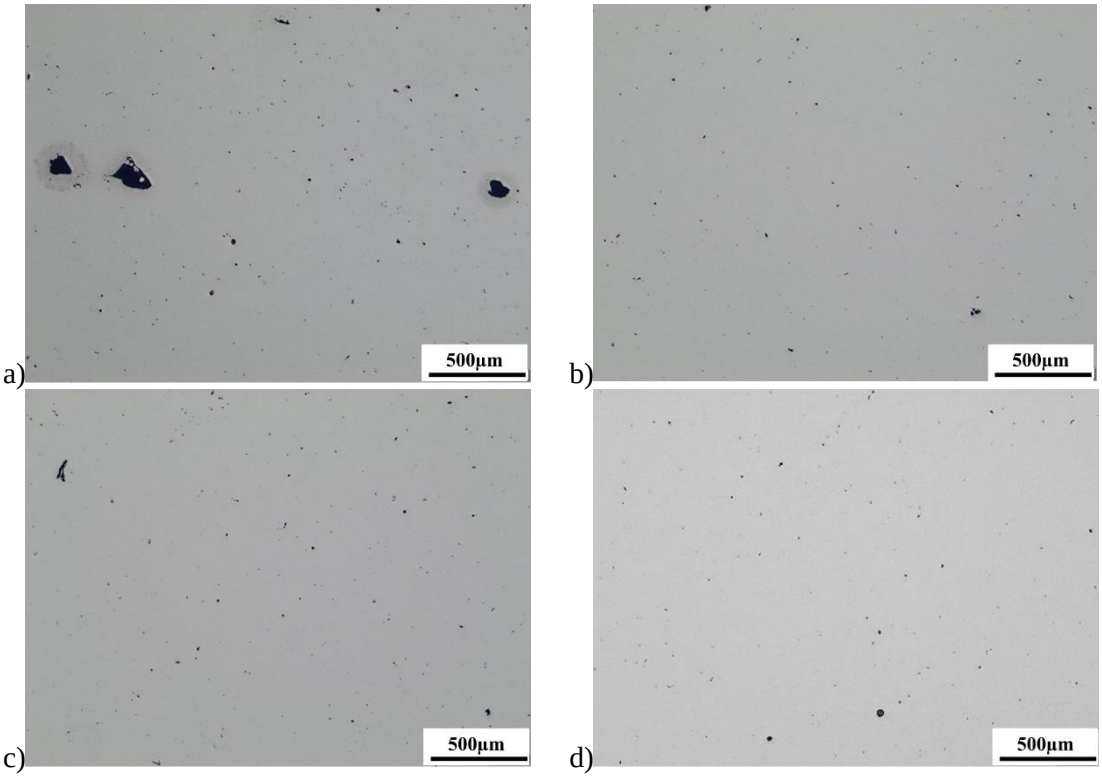

Figure 61: *optical microscope analysis of RUNOUT (b,d) and KO(a,c) specimens sections in B printing height. Magnification 50x. Samples shown in a,b) are built in Z direction, while those in c,d) are XY.*

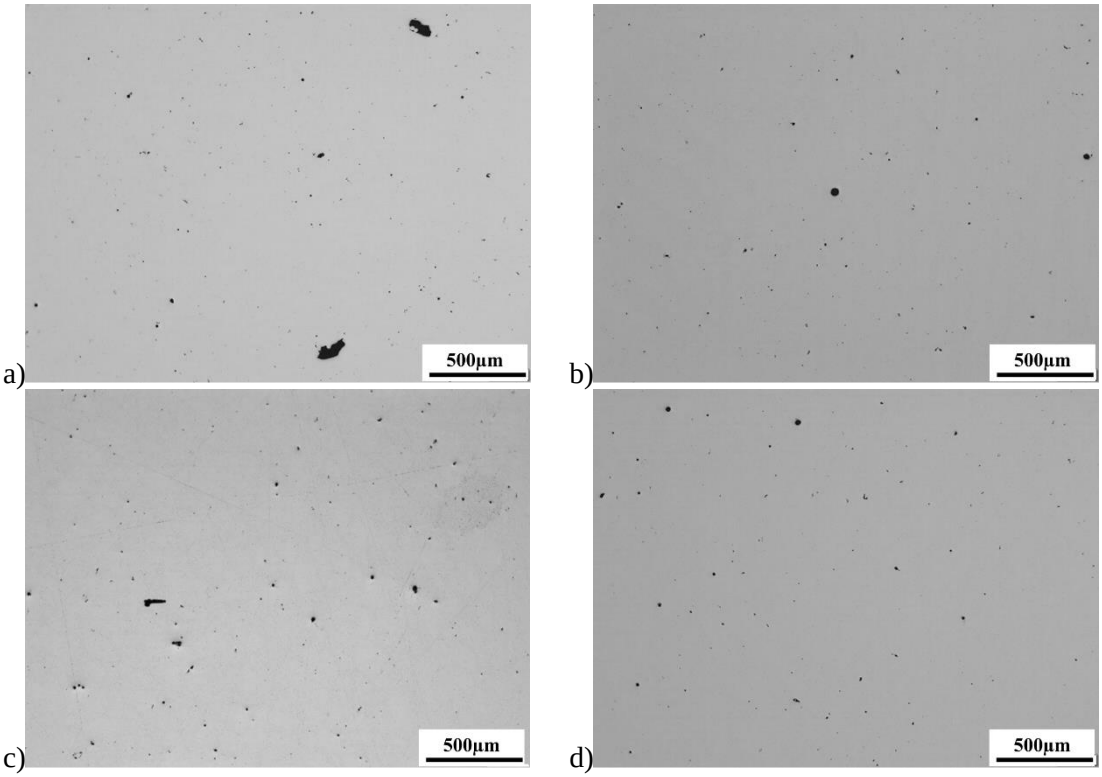

Figure 62: *optical microscope analysis of RUNOUT (b,d) and KO(a,c) specimens sections in C printing height. Magnification 50x. Samples shown in a,b) are built in Z direction, while those in c,d) are XY*

Having seen also in this study the presence of defects as luck of fusion mainly in Z specimens, the defect distribution in terms of size was not carried out for XY samples. Defects found in sections of Z specimens were collected and subdivided in dimension frequency classes. The graph in figure 63 shows the results obtained, that confirmed what previously seen in paragraph 4.2.1.

Almost the totality of defects has a dimension lower than 100 μm^2. The grey area highlights the frequency classes relative to dimensions greater than 2000 μm^2. Once again, above this "trigger" dimensions, there are almost only defects corresponding to KO. This confirms the hypothesis on the more probable failure of those specimens that has defects greater than this size, making 2000 μm^2 a stronger threshold value.

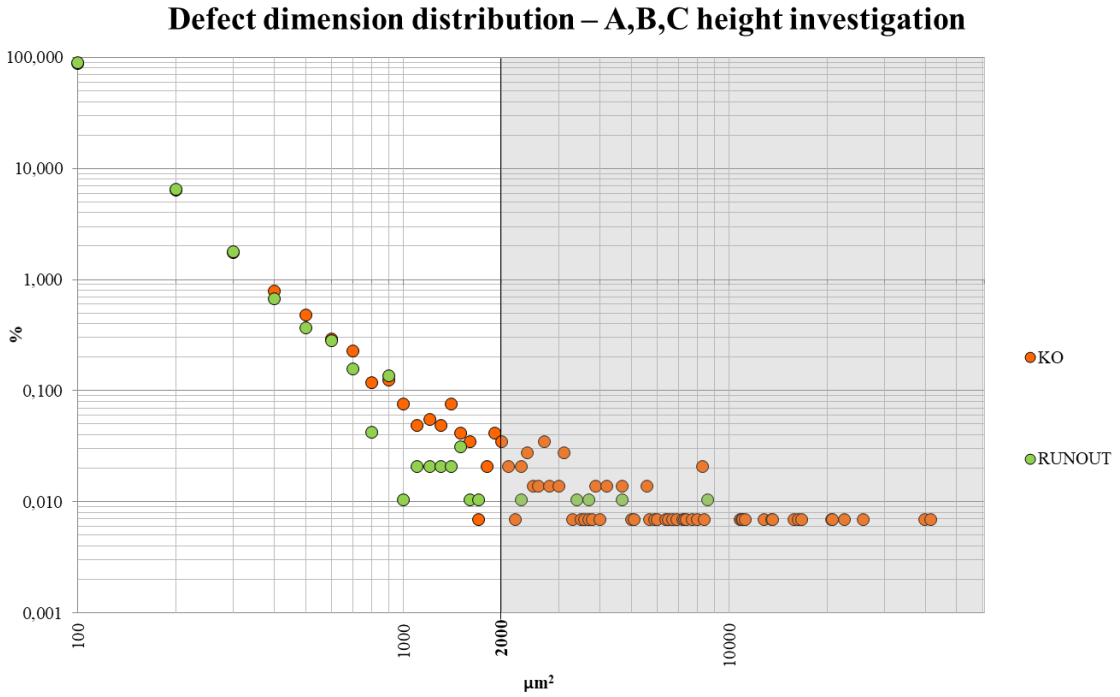

Figure 63: *Defect dimension distribution of KO and Runout Z machined fatigue specimens with indication of the defect with an area greater than 2000 µm2. The results are relative to all the Z specimens regardless the height (A, B or C) since no differences in fatigue limits was observed.*

4.3 Summary and Conclusions

Mechanical characterization of L-PBF AlSi10Mg alloy is here presented and analyzed. In detail, starting from heat treatments evaluation, it was highlighted SR importance in reducing residual stresses, as shown in picture 33.

Moreover, by heat treatments evaluation it has been demonstrated the inversely proportional relation between UTS and SR temperature, under same duration conditions. In this way, it was possible to establish a wide range of mechanical properties achievable with AM. From micrographic analysis, stress relieves at temperatures between 160°C and 290°C do not change deeply microstructure since melt pools are still visible in section. The difference became noticeable with SEM. Silicon network at melt pool boundaries starts breaking with the increase of SR temperature. This probably gives more freedom to dislocation to move, mitigating the Hall-Petch hardening effect.

T6 heat treatments were also evaluated. Peaks of hardening were obtained for different artificial aging. In detail, T6_2 and T6_3 showed the same aging curves with higher UTS for low AA duration, making these two HT competitive also from a productive point of view. Anyway, the highest UTS value was obtained with T6_4. Nevertheless, this HT was not considered applicable for the risk of deformations given by water quenching at Tamb.

For a complete mechanical characterization, fatigue behavior was studied by different rotating bending fatigue campaigns. It resulted that orientation affects fatigue since in general XY specimens exhibited fatigue resistance 70% higher than Z ones (both in machined conditions). Second test was related to the influence of Z samples surface condition (machined and not machined) on fatigue. Here, as printed specimens survived to fatigue tests with half the limit

obtained on machined specimens. Looking at fracture surfaces, fatigue cracks in not machined specimens started always from external surface due to the high surface roughness.

On the other hand, starting from defects observed at fatigue origin on fracture surfaces of machined samples, a trigger defect dimension equal to $2000\mu m^2$ was found. By image analysis, isolating only those defects greater than $2000\mu m^2$ it was noticed that they were more frequent in KO specimens. Moreover, looking at JOB layout, since KO samples were located for the majority in the region towards Argon outlet, it can be suggested that fatigue resistance is also affected by part position on build platform in terms of higher frequency of spatter particles towards Ar outlet that are one of the causes for formation of defect with significant dimensions.

For what concerns printing height, no influence was noticed on fatigue resistance of both Z and XY machined specimens. Here, once again, the better fatigue behavior of XY samples was confirmed. Moreover, same defect analysis was performed on XY and Z samples (both KO and runouts). It was highlighted the higher presence of defects with great dimensions in Z KO specimens, while significant "cleaner" sections were observed in Z runout samples and XY samples (both KO and runout). This could be one of the reasons behind the better fatigue behavior in XY direction. Moreover, it was confirmed the effectiveness of considering $2000\mu m^2$ as a threshold defect dimension for printed part quality evaluation, since only few defects with areas greater than this value were observed in runout specimens (regardless the printing direction).

CHAPTER 5
PROCESS PARAMETERS OPTIMIZATION FOR MECHANICAL CHARACTERISTICS AND PRODUCTIVITY IMPROVEMENT

This study, object of publication [91]was carried out to look for the process parameters optimization in terms of finding the best compromise between high mechanical characteristics and technology productivity.

In fact, given the necessity of introducing additive manufacturing not only for prototyping, but also with the goal of components production, the built part costs assume as much importance as the part quality. Therefore, a large campaign was set up to find the best parameters that could guarantee good quality, proper mechanical characteristics and a drop in building times.

Reducing JOB duration has not a great impact on the single component production. Douglas S. et al. [92] examined costs related to additive manufacturing technology, considering different cost items, as graphed in figure 64.

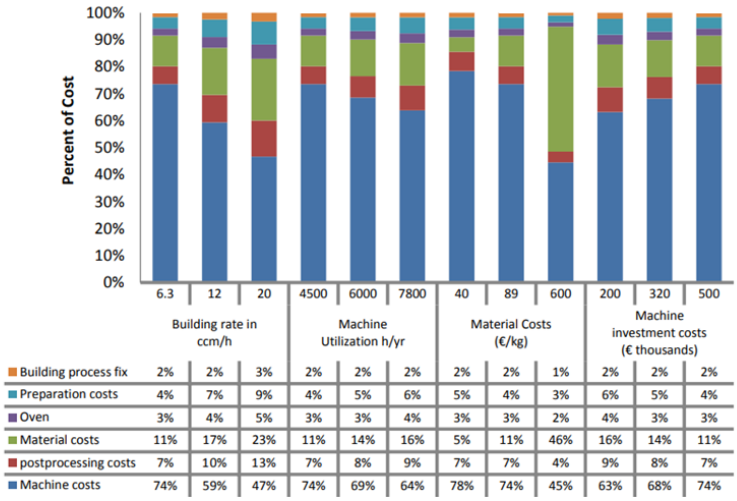

	6.3	12	20	4500	6000	7800	40	89	600	200	320	500
	Building rate in ccm/h			Machine Utilization h/yr			Material Costs (€/kg)			Machine investment costs (€ thousands)		
Building process fix	2%	2%	3%	2%	2%	2%	2%	2%	1%	2%	2%	2%
Preparation costs	4%	7%	9%	4%	5%	6%	5%	4%	3%	6%	5%	4%
Oven	3%	4%	5%	3%	3%	4%	3%	3%	2%	4%	3%	3%
Material costs	11%	17%	23%	11%	14%	16%	5%	11%	46%	16%	14%	11%
postprocessing costs	7%	10%	13%	7%	8%	9%	7%	7%	4%	9%	8%	7%
Machine costs	74%	59%	47%	74%	69%	64%	78%	74%	45%	63%	68%	74%

***Figure 64**: Costs distribution in percentage, related to part production with AM* [93]

The graph shows the cost impact in percentage on the part production. According to the first three columns, the costs vary with the increase of the building rate. In detail, machine costs influence on total costs decrease with build rate growth. At the same time, building process becomes more relevant. This means that, though job printing is not the main cost item, it assumes more importance by decreasing the building time. Moreover, considering printing the same component, the amount of metallic powder remains unvaried, while the machine costs decrease. Therefore, build rate increase leads to a general cost diminution that is one of the main goals to be achieved.

5.1 Mechanical characterization and influence on density and metallurgical quality

As explained in paragraph 3.4, a large DOE was set up by defining a matrix in which hatch distance and scanning speed varied by constant steps while keeping constant the laser power.

In the first step of this study, parameter combinations in the proximity of the standard ones were considered, with volumetric energy densities (VED) in the range of 30-45 J/mm^3.

The graphics in figure 65 show the results obtained from the tensile tests on specimens built with the different parameter combinations. Generally, it can be noticed that the worst results are related to the application of high hatch distances and low scan speeds. On the opposite, higher mechanical properties can be achieved by using medium/low hatch distances and high scan speeds (greater than 1300 mm/s).

Figure 66 shows how the tensile properties relate to the VED.

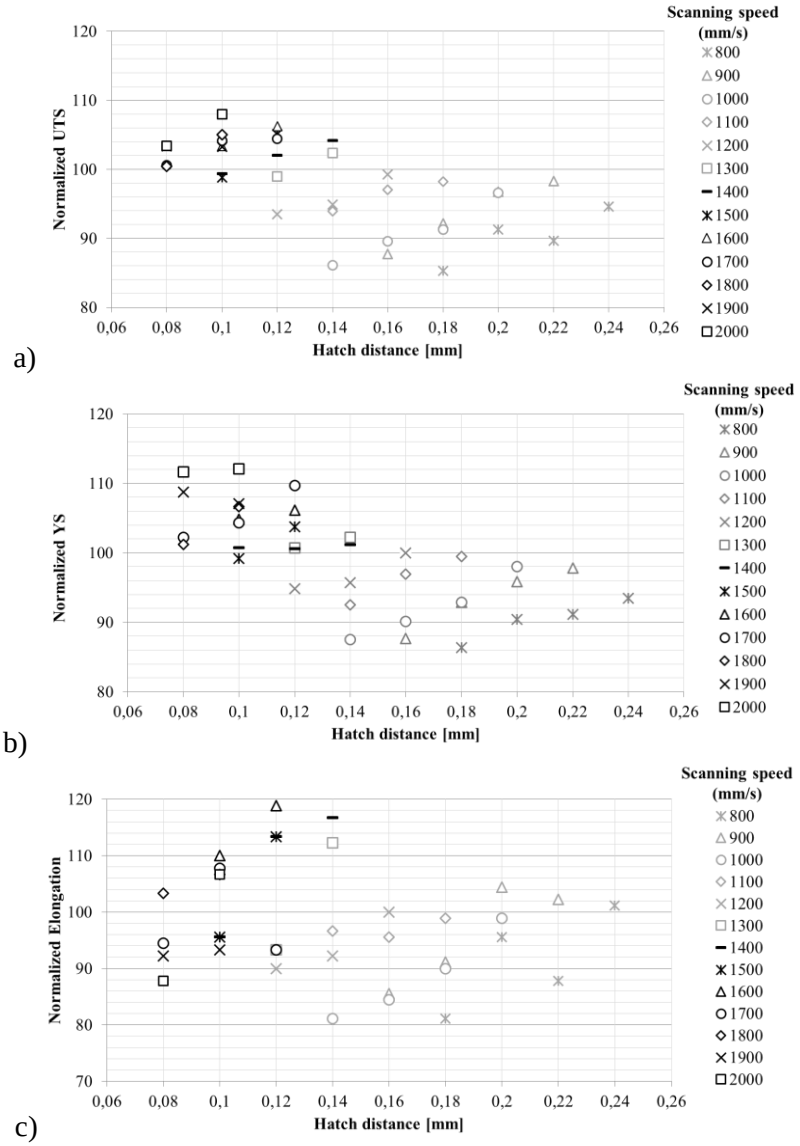

***Figure 65**: Mechanical properties of parts built with the setups considered in step 1 of the analysis.*

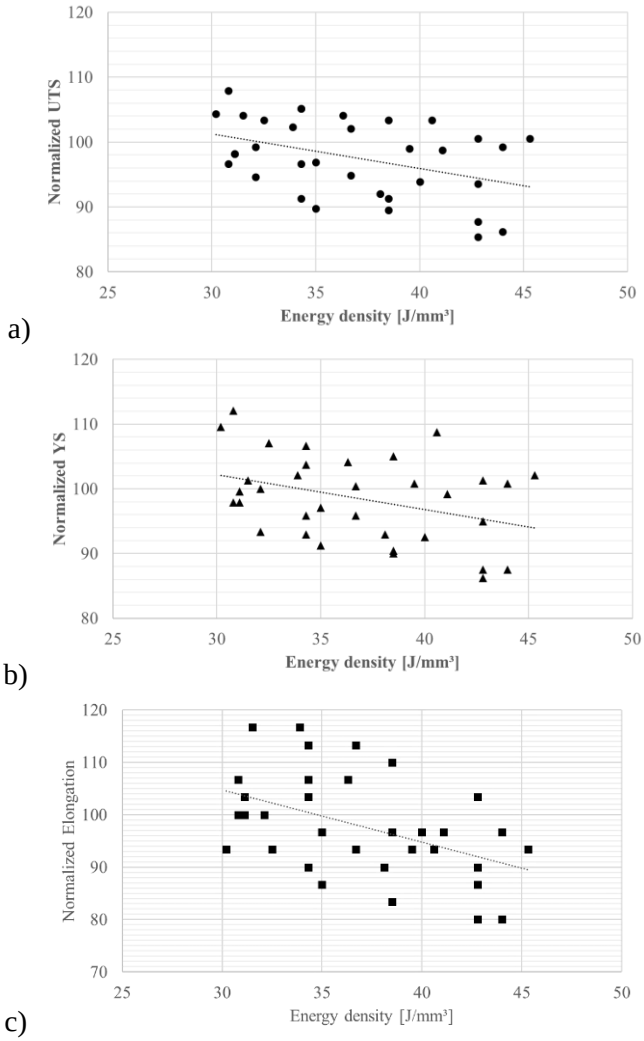

***Figure 66**:Variation of tensile properties versus energy density. Results refer to the step 1 of the analysis.*

A slight decrease of the mechanical properties with the increase of VED can be seen. This is represented by the trend lines in each graph.

As a general result, the best mechanical properties were generally obtained with the application of an energy density between 30 and 40 J/mm³ and a hatch distance between 0,08 and 0,12 mm. With the use of parameter combinations within this range it was possible to achieve UTS and YS higher than nominal reference values.

For each pair of parameters, the density was measured with Archimede's method, as described in paragraph 3.2. This analysis had the aim to have a first glance on the inner quality of the printed parts and to evaluate eventual correlations between density and the process parameters.

The graph in figure 67 shows a trend similar to the one observed for the tensile properties, with best results corresponding to the combinations of high scanning speed (1700-1800 mm/s) and low hatch distance (0,08-0,10 mm). Moreover, the results become more scattered if the parameters corresponding to scanning speed between 800 and 1000 mm/s are considered. Furthermore, the density values measured are completely independent on the energy density. In this regard, the graph in figure 68 shows the density in relation to VED. The results have a great dispersion and a horizontal trend that underlines the lack of influence of VED applied on the part density.

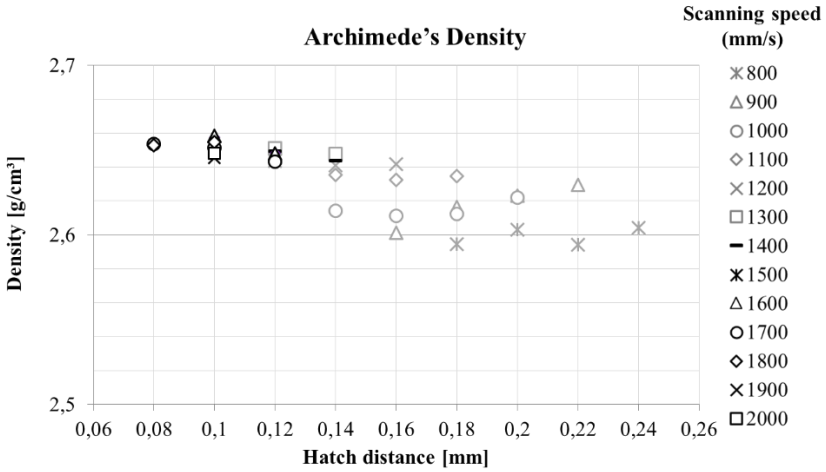

***Figure 67**: densities measured with Archimede's method in relation to the different parameters applied in step 1 of the analysis.*

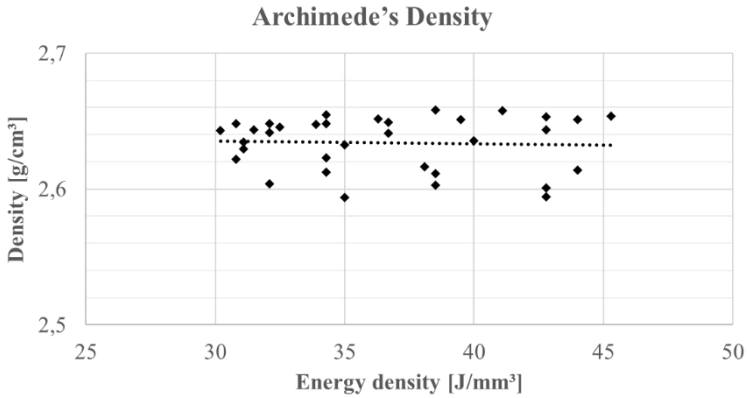

***Figure 68**: Density measurements with Archimede's method in relation to the energy density incident on the powder bed.*

The inner quality was better evaluated by image analysis. Sections of cubes printed with parameter combinations corresponding to the extremes of the matrix were made to analyse the internal porosity and the presence of defects.

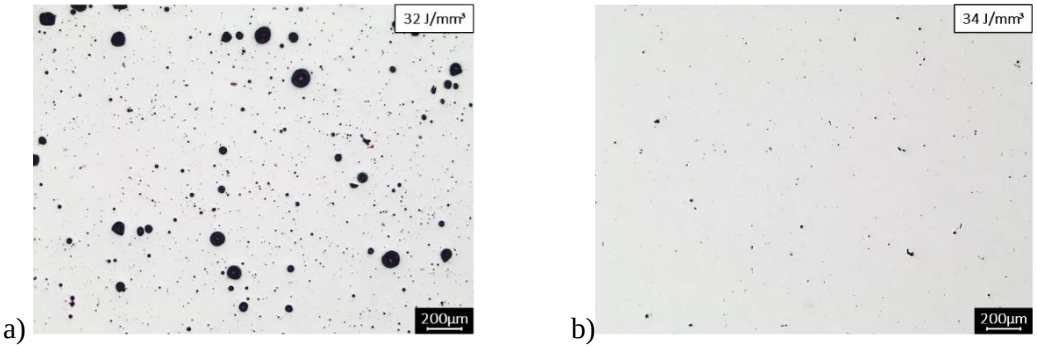

***Figure 69**: optical microscope images of sections of cubes printed with the following parameters combinations. a) h= 0,24mm; v=800mm/s; b)h=0,1mm; v= 1800 mm/s.*

Figure 69 shows the difference in terms of internal porosity between samples built with 800mm/s of scanning speed and 0,24mm of hatch distance (Figure 69a) and 1800mm/s of scanning speed and 0,1mm of hatch distance (Figure 69b). To these combinations correspond almost the same energy density (32 and 34 J/mm³ respectively). That means that even in the case of porosity

analysis, VED has a low impact on the results. Once again, hatch distance and scanning speed are the main factors that affect the quality of the printed part.

In fact, as shown in Figure 69a, when high hatch distance and low scanning speed are applied, spherical porosity with significant dimensions are obtained. In detail, for specimen in Figure 69a, a relative density of 98,9% was measured with an average defect dimension of 143µm². On the other hand, the sample in Figure 69b appears free from defects with a relative density of 99,7% and an average porosity dimension of just 20 µm². The difference noticed in these two cross sections may be due to the different thermal histories. In fact, though the powder bed undergoes the same energy density, the solidification mechanism differs in relation to the exposure time to high temperatures. When the laser moves on the building plate with a low scanning speed, the powder sees high temperature for a sufficient time for gas porosity to generate, with dimensions and shape typical of a keyhole melting mode [94]–[96]. On the other hand, the hatch distance (0,24mm), is not low enough to guarantee a correct re-melting of the adjacent tracks. Therefore, the bubbles generated during the previous laser scanning, have no possibility to escape and remain entrapped in the already solidified metal.

The application of a high scanning speed and a low hatch distance solves this problem, since no keyhole melting mode occurs, while correct densification is guaranteed by an appropriate re-melting of the adjacent laser tracks. Moreover, it is worth emphasizing that in neither case printing defects as lack of fusion occur.

The results from density and image analysis confirm what formerly stated about mechanical properties. Therefore, the process setups that generally lead to the best production in terms of both mechanical characteristics and inner quality are those referring to the bottom left part of the matrix, corresponding to the application of a high scanning speed and a low hatch distance.

On the other side, this area is mostly characterized by long build times. As a consequence, the production times and costs are generally higher. That is the main reason why, in the second step of the analysis, a greater number of parameter combinations was considered (corresponding to the yellow cells in the matrix presented in paragraph 3.4), mostly moving onto the bottom-right part of the matrix, in order to look for a compromise between build time and printing quality.

The graphs in Figure 70 show the normalized mechanical characteristics versus the incident volumetric energy density. The results of step 2 are displayed by the crosses that have been added to the circles already seen for step 1. In contrast to what previously discussed for step 1, the application of a wider range of energy densities makes its effects on the mechanical properties more visible. The trend is almost the same for UTS, YS and elongation, with an optimum corresponding to an energy density between 30 and 35 J/mm³. In detail, the mechanical properties (especially elongations and UTS) significantly decrease with the application of a VED lower than 25 J/mm³. On the contrary, over an energy density of approximately 45 J/mm³ the curves tend to stabilize. The UTS graph also reports the build time variation. It can be seen that, to be competitive from a productive point of view while maintaining good mechanical characteristics, an energy density around 30 J/mm³ should be applied. Moving towards the central range of energy density (the one corresponding to the step1), as stated before, the influence on mechanical properties decreases, with the disadvantage of more scattered results.

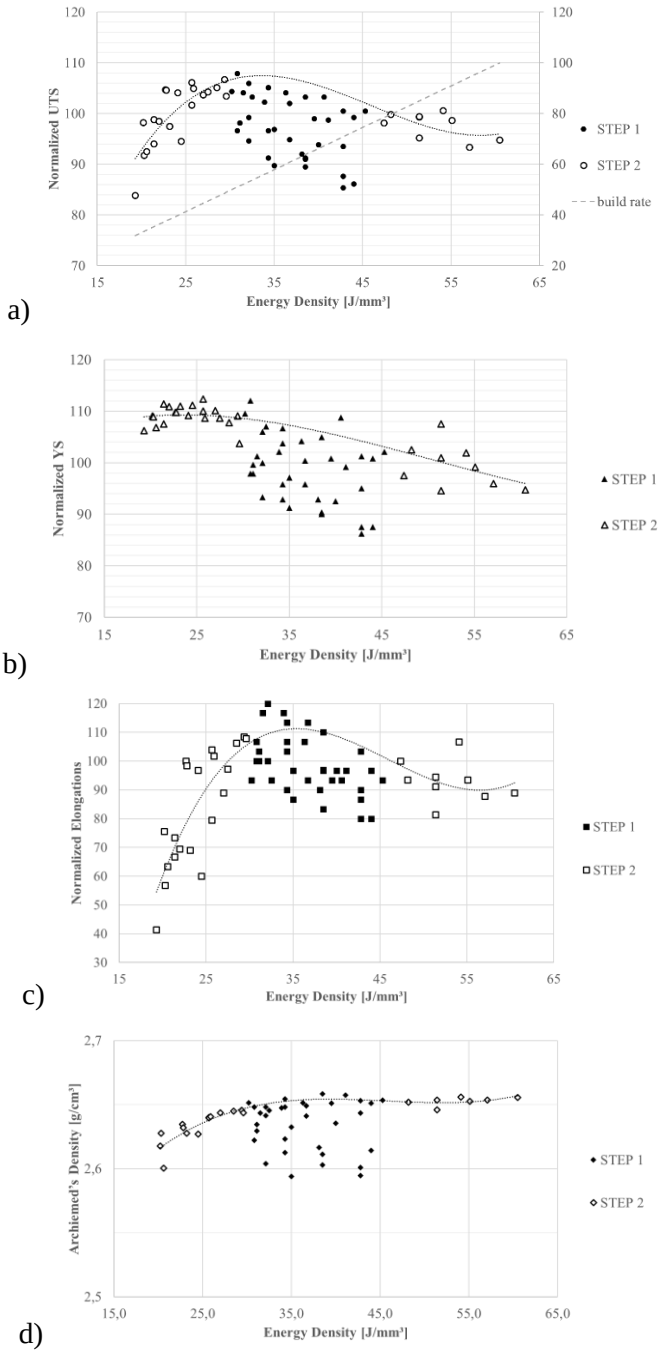

***Figure 70**: mechanical properties measured for the setups of step 2 (black dots) superimposed to those of step 1 (white dots), plotted against the energy density.*

Regarding the density (Figure 70d), even with the extension of parameter combinations considered in step2, the conclusions remain almost unchanged. Energy density still has small impact on Archimede's density, with a slight decrease tendency moving towards 20 J/mm³.

Regarding this, according to literature, the results are various and conflicting. Several studies achieved almost the same densification level while applying very different energy densities [97]–[99]. Other research are in contrast with what found in this study. Read et al. [100] studied the relationship between porosity and applied energy density. This study investigated a higher range of energy densities and claimed 60 J/mm³ as the best value for density maximization, with a steep decrease moving towards lower energy densities. Giovagnoli et al. [101] examined a VED spectrum (40-70 J/mm³) that partially intersects the one investigated in this study. They found a

clear decrease in density with the increase of the energy density applied, in stark contrast with this research, despite the adoption of almost the same VEDs. In light of the contrasting results obtained in literature with the same energy densities application, as stated also in [101], it seems that this variable is not the right discriminating factor for the parameters optimizations. Anyway, it is important to remember that the process parameters are extremely machine specific. This means that the optimized parameters found using a L-PBF machine may not fit the others.

Supporting this hypothesis, it is worth noting that the tensile results from the experiments performed in step 1, when different parameter combinations sharing the same energy density were applied, have a significant dispersion. As it can be seen in this study, if a fixed laser power is considered, the hatch distance and the scanning speed are the factors that effectively affect the mechanical properties. Tables 12 and 13 report the UTS, YS and elongation variations in relation to the percentage variation of hatch distance and scanning speed. In detail, the values were calculated by fixing one parameter at a time, corresponding respectively to 0,14mm of hatch distance and 1700mm/s of scanning speed.

It appears that, despite the greater percentage growth steps of hatch distance, this variable led to less marked mechanical properties variations in comparison to what happened by varying the scanning speed, making this latter parameter the most influencing one.

Scanning speed (mm/s)	Scanning speed percentage variation (%)	UTS percentage variation (%)	YS percentage variation (%)	Elongations percentage variation (%)
1000				
1100	+10,0	+9,1	+5,7	+19,2
1200	+9,1	+1,0	+3,5	-4,6
1300	+8,3	+7,9	+6,8	+21,7
1400	+7,7	+1,7	-1,1	+4,0
1500	+7,1	+2,5	+7,9	-7,1
1600	+6,7	-2,3	-0,4	-10,3
1700	+6,3	+0,7	0,0	+4,6
1800	+5,9	-9,9	+2,2	-41,0
1900	+5,6	+3,1	-0,1	+14,8
2000	+5,3	+1,1	-0,1	+0,8

Table 12: *Percentage variations of UTS, YS and elongation with varying scanning speed for a fixed hatch distance of 0,14mm*

Hatch distance (mm)	Scanning speed percentage variation (%)	UTS percentage variation (%)	YS percentage variation (%)	Elongations percentage variation (%)
0,06				
0,08	+33,3	+6,1	+7,9	+6,3
0,10	+25,0	+3,5	+2,0	+14,1
0,12	+20,0	+0,3	+5,2	-13,4
0,14	+16,7	+0,5	-0,9	+8,9
0,16	+14,3	-0,2	+1,0	-1,6
0,18	+12,5	-6,2	-0,7	-24,4

Table 13: *Percentage variations of UTS, YS and elongation with varying hatch distance for a fixed scanning speed of 1700mm/s*

Image analysis of cube sections printed with an energy density below 31 J/mm³ indicated that for values around 25 J/mm³ lack of fusions defects start occurring, regardless of the applied setup (Figures 71 a, b and c). On the contrary, Figure 71d shows that with an energy density of around 31 J/mm³, high scanning speed and low hatch distance, printing defects disappear, replaced by small porosity.

This phenomenon supports what stated in the first step of the analysis regarding the influence of parameters on the printed part inner quality. Moreover, it is coherent with the Archimede's density

results found in the step 2 since the low energy densities are accompanied by a slight density diminution.

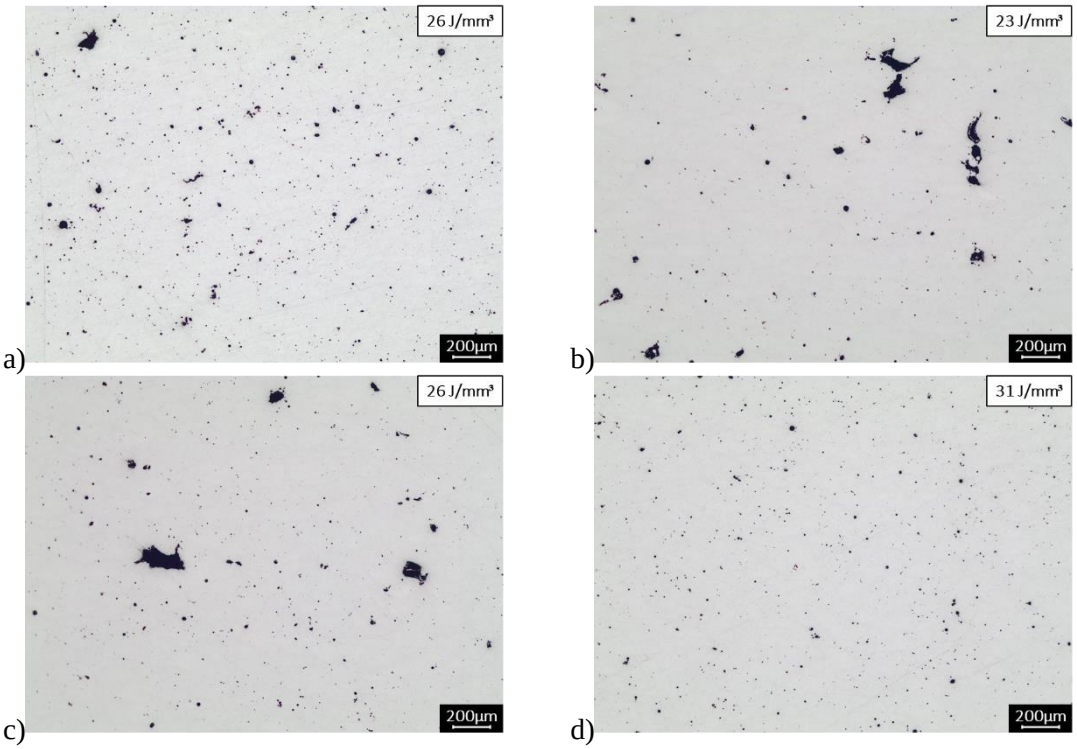

Figure 71*: optical microscope images of sections of cubes printed with the following parameter combinations. a) h= 0,16mm, v= 1500mm/s; b)h=0,18mm, v= 1500 mm/s; c) h= 0,14mm, v= 1700 mm/s; d) h= 0,1mm, v= 2000 mm/s.*

5.2 Rotating bending fatigue test

Three parameter combinations were chosen and tested on rotating bending fatigue machine, as described in paragraph 3.2.4. The aim of this study was to evaluate the effect of parameters on defect distribution and, as a consequence, on fatigue life.

For a direct comparison, standard parameters were tested in parallel, to find the precise delta with each single parameter combinations considered.

The parameter combinations selected belonged all to the same range of mechanical properties and led to a productivity increase between +5% and +20% in respect to standard parameters. 16 vertical bars were printed with each parameter combination in the same JOB, distributed in order to have one specimen for each parameter in every row of each single laser area. A scheme of the build layout is shown in Figure 72. The bars were subsequently machined to final shape geometry (Figure 28, paragraph 3.2).

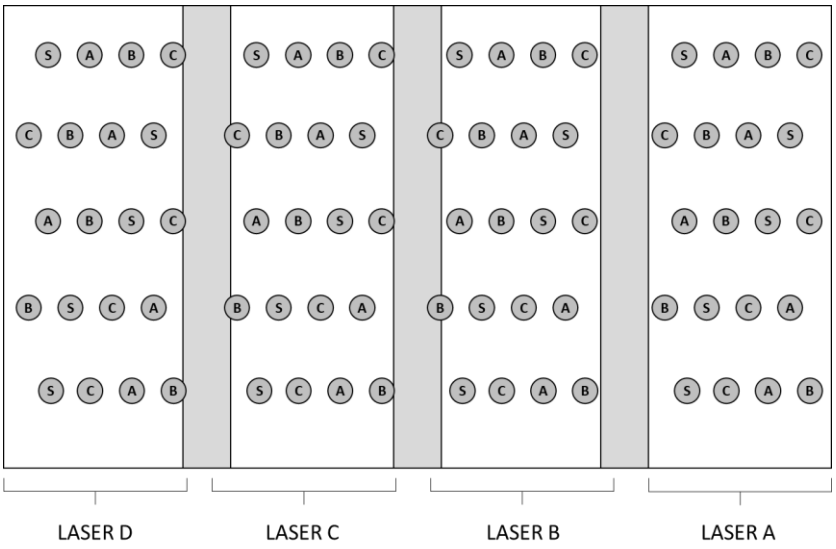

Figure 72: *JOB layout of Z cylinders bars with indication of process parameter used (STD S, A, B and C). Samples were randomly distributed all over the build plate. 5 samples per each parameter set were printed in each LASER areas.*

Table 14 shows the percentage variation of mechanical properties, productivity and fatigue limit obtained (calculated with 50 percentile) in relation to STD parameters results. All the parameters tested led to a decrease of fatigue life between 20 and 33%, while no significant variation was observed on mechanical characteristics.

To better understand this phenomenon, a deep analysis was carried out on specimen sections, looking for correlations between fatigue life and defects dimension and morphology.

PARAMETERS	UTS percentage variation (%)	YS percentage variation (%)	Elongations percentage variation (%)	Productivity percentage variation(%)	Fatigue limit percentage variation (%)
STD	-	-	-	-	-
A	+2%	+2%	-6%	+5%	-20%
B	+5%	+6%	+3%	+10%	-33%
C	+4%	+5%	-3%	+20%	-30%

Table 14: *percentage variation of mechanical properties, productivity and fatigue limit for each set of parameters.*

Even in this study attention was put on differences in terms of location of failure specimens along the build plate. In detail, the 70% of failures occurred on the build plate half corresponding to the area towards the argon flow outlet, while, on the other side, 80% of runouts were related to specimens built towards the inlet, regardless the process parameters used. This phenomenon confirmed what previously stated in chapter 4, which is the higher probability of irregular shape defects with significant dimensions that affects the fatigue life on parts printed towards the argon outlet.

Defect analysis was performed on 8 specimen sections for each parameter combination. Samples built with standard parameters were analysed for a direct comparison. For every section, all the defects detected were categorized in relation to area dimension and sphericity and divided in frequency classes.

Figure 73 shows the defect distribution in relation to sphericity. In detail, the distribution of defects found in specimens built with STD parameters is shifted towards higher sphericity, while the one corresponding to C parameters is translated towards lower sphericity values. This means that in general C parameters tend to generate defects with more irregular shape, detrimental for fatigue life, while STD parameters may help printing parts with more spherical defects. This is confirmed by fatigue results since C parameters led to a fatigue limit decrease around 30% in comparison to the standard ones.

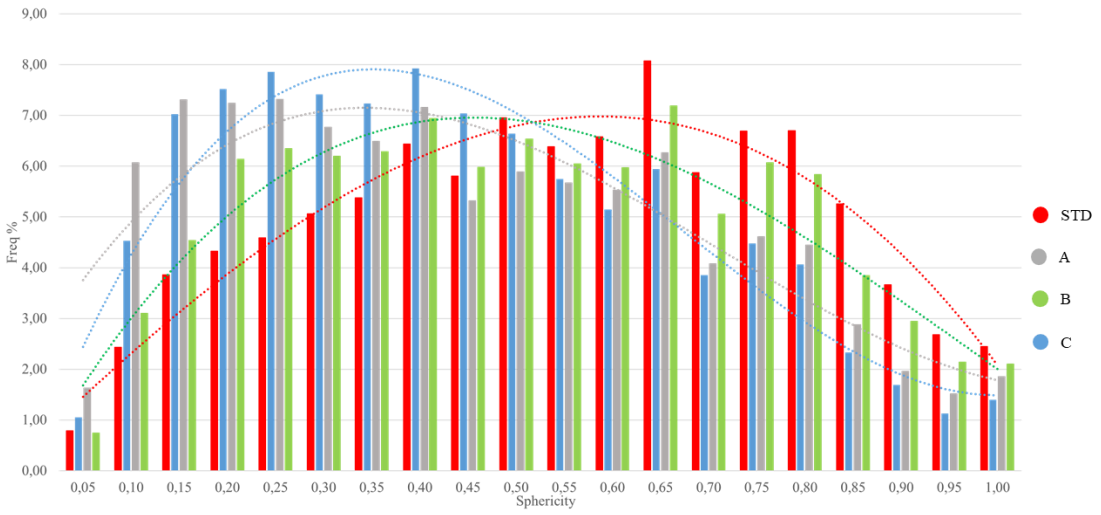

Figure 73: *Defect distribution in relation to sphericity for each set of parameters*

To evaluate the effect of defect dimensions, a Gaussian distribution was calculated for each parameter combination (Figure 74). Defect area values are not perfectly described by a normal distribution since the bell curve is not symmetrical in respect to the mean value. Anyway, this model was applied to have a clear and graphical comparison.

As can be seen in the graph, the red curve (corresponding to standard parameters) has the highest maximum, shifted towards small area values, meaning that standard parameters lead to the formation of defect not only more circular but also smaller. This once again explains the higher fatigue value obtained. On the other side, B parameters are characterized by a wider dimension curve, so by generally bigger defects.

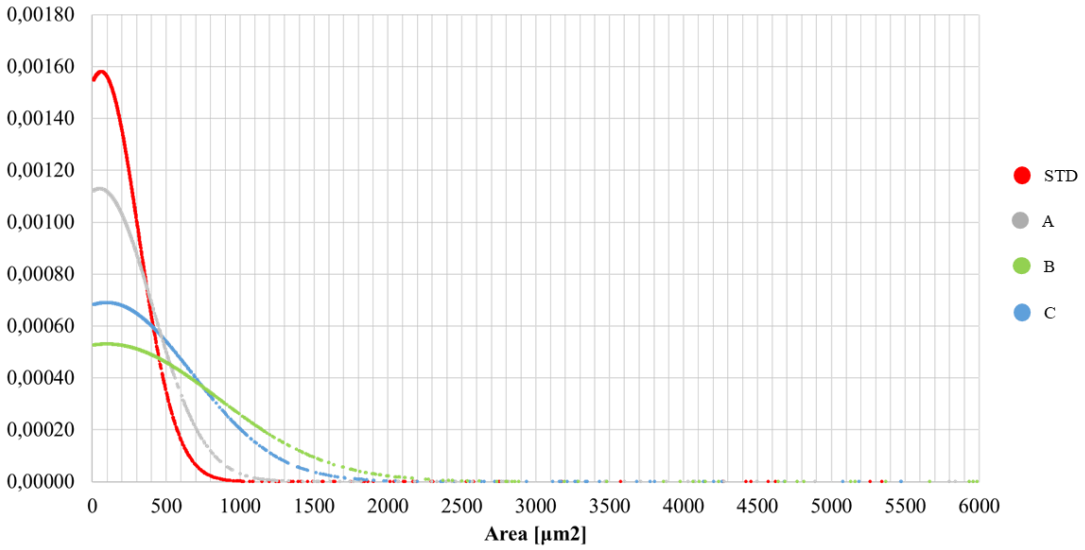

Figure 74: *Gaussian distribution of defect area for each set of parameters.*

The same "trigger" value for defect dimension discussed in chapter 4, 2000 µm^2, was considered as an evaluation method. In parallel, the frequencies of defects with low (<0,3) and high sphericity (>0,7) were calculated for each parameter combination. In detail, a sphericity below 0,3 is typical of irregular shape defects as lack of fusion, as can be seen in Figure 75.

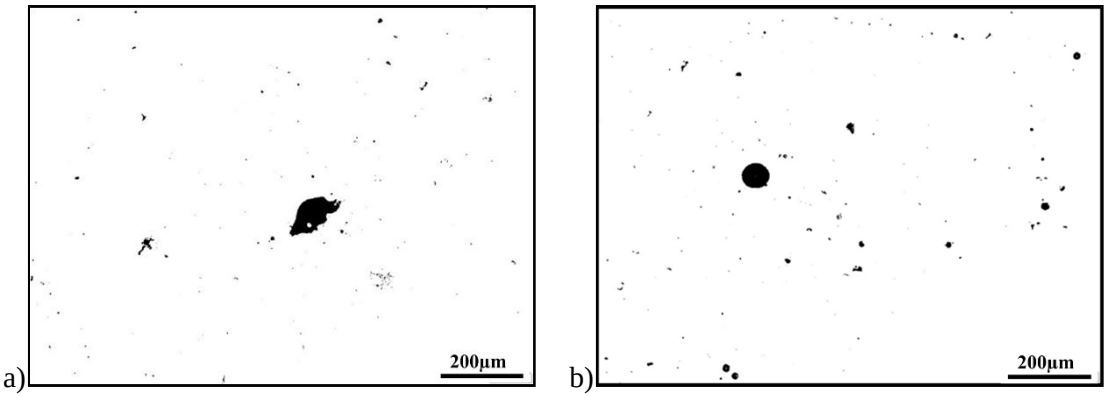

Figure 75: *Binary micrographics images with defects characterized by different sphericity values: a) lack of fusion, sphericity <0,3; b) gas porosity,sphericity >0,7*

In table 15 are listed the results. The higher is the number of defects bigger than the threshold value the lower is the fatigue limit. Such linear correlation cannot be made for sphericity, since, for example, parameters B are related to defects similar to those generated by STD parameters but led to a significant fatigue life reduction. This, on the other hand, could be explained by the high number of defects greater than 2000 µm^2.

PARAMETERS	Number of defects greater than 2000 µm2	Sphericity <0,3 (%)	Sphericity >0,8 (%)	Fatigue limit percentage variation (%)
STD	28	16%	28%	-
A	37	30%	17%	-20%
B	70	20%	23%	-33%
C	51	30%	15%	-30%

Table 15: *Summary defect morphologies results in relation to the fatigue limit*

5.3 Summary and Conclusions

For boosting productivity, several parameter combinations were evaluated by tensile tests and density measurements, within an overall VED range between 17 a 57 J/mm^3.

The results in terms of density, internal porosity and tensile properties of AlSi10Mg parts produced by L-PBF allow reckoning that the volumetric energy density is not a self-sufficient parameter for process optimization. The Archimede's density measured in this study is not significantly affected by VED variation, especially in the range of 25-55 J/mm^3. In addition, under the same VED, specimens exhibited extremely different degrees of porosity.

Despite not being a comprehensive parameter, nevertheless VED can be useful to identify ranges where the process is effective. In the present study, the best tensile properties were achieved for VED between 30 and 35J/mm^3. Within this window, for a parallel optimization of the building time, the choice of an energy density equal to 30 J/mm^3 represents a good compromise between part quality and productivity.

If the laser power is fixed, hatch distance and scanning speed truly affect the quality of the printed part, both in terms of mechanical properties and microstructure. In detail, this study demonstrated the greater mechanical characteristics sensitivity to scanning speed variation, in comparison to the smaller impact of hatch distance.

The three most promising parameter combinations were further investigated by rotating bending fatigue test, in comparison to STD parameters. The results showed a significant decrease in fatigue resistance while static mechanical properties remained almost unchanged. The reason behind this phenomenon lies once again in the type of defects detected in sections. Defect analysis, carried out also in chapter 4, was here repeated and extended by considering not only defect dimensions but also defect morphology. STD parameters, among all the four combinations considered in this study, showed defects with smallest dimensions and highest sphericity together with the greatest fatigue limit.

Anyway, defect dimension remains the main factor influencing fatigue life of the specimens since a linear correlation was found between fatigue resistance decrease and increase of defect number with area greater than 2000µm^2. Secondly, the conjunction between defect dimension and morphology has to be avoided whenever fatigue resistance is a leading design factor.

CHAPTER 6
SURFACE TREATMENTS INVESTIGATION

AM parts are characterized by an intrinsic relatively high surface roughness due to the printing process itself. The problems related to a high surface roughness are easily attributable to a poor aesthetic and to a decrease in fatigue resistance of the part (as demonstrated in paragraph 4.2.1). Here comes the need of founding surface treatments that could minimize these problems.

As described in 3.5 two kinds of surface treatments were considered, classified as mechanical and chemical. To the first class belongs barrel stone machining and shot peening with B60 ceramic beads and S110 steel shots. On the other hand, to the second type chemical milling, DryLyte®, green etching® and hirtisation® were considered.

6.1 Morphological analysis and surface roughness measurement

First of all, surface treatments were visually evaluated by comparing surface morphologies. Hence, printed cubes surfaces were analysed both at stereo microscope and SEM.

Starting from stereo microscope investigation, each surface treatment was evaluated in comparison to the as printed condition and also considering the effect on the part edge.

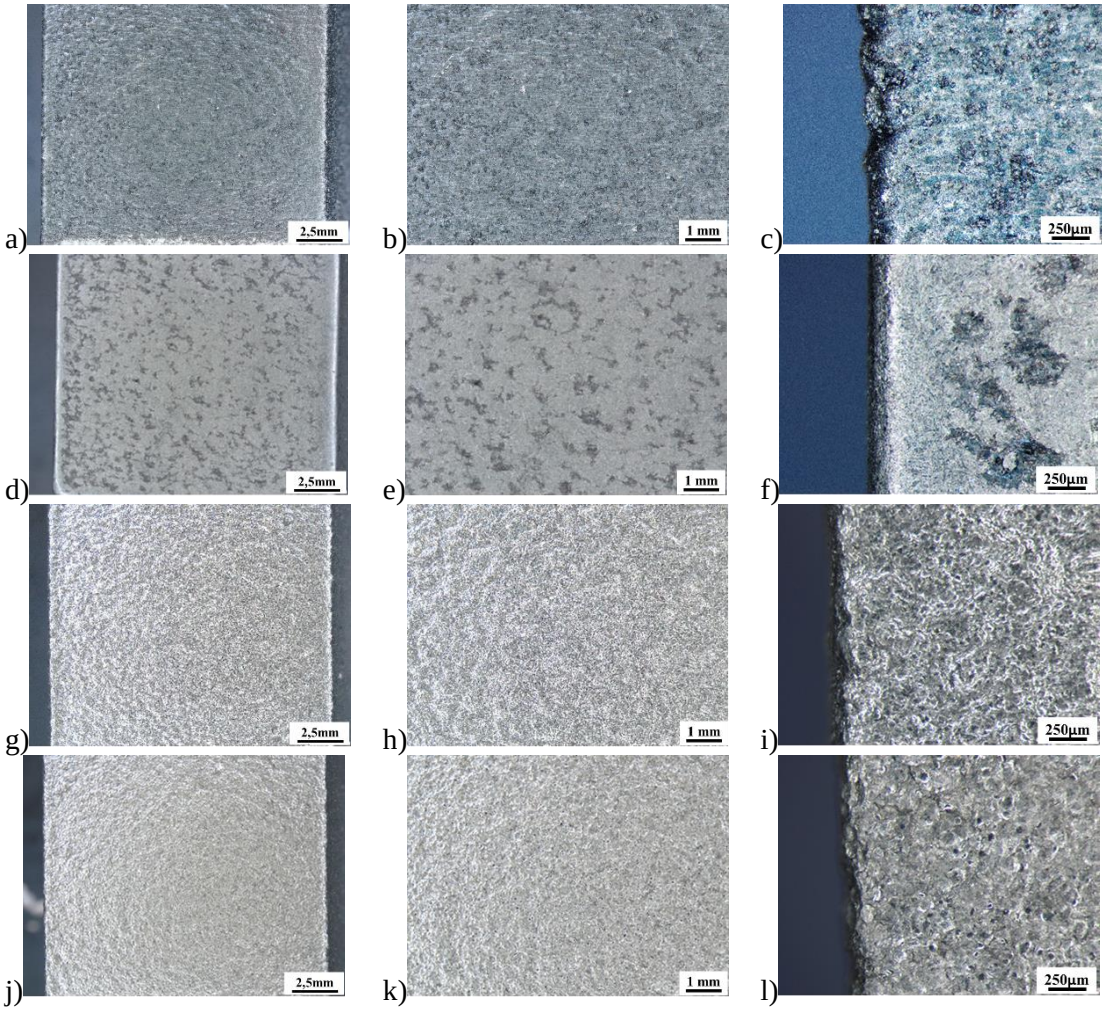

***Figure 76**: Morphological analysis of AlSi10Mg Am cube surfaces with different "mechanical" treatments: as printed (a,b,c,); barrel stone machining (d,e,f); shot peening with B60 ceramic beads (g,h,i); shot peening with S110 steel (j,k,l). In detail, pictures (a,d,g,j) and (b,e,h,k) show morphological surfaces overviews (at 7x and 12,5 x magnification respectively), while (c,f,i,l) images focus on differences in cube edges after each surface treatment.*

Looking at the “mechanical” surface treatments (figure 76) in all the treated conditions an improvement can be seen in terms of disappearance of the not melted powder present on the as printed cubes surface. Anyway, not a particular increase in smoothness was noticed, exception made for samples that underwent barrel stone machining, which led also to a significant corner smoothening (figure 76f).

Shoot peening, regardless the spheres material, caused a brighter surface, hence an increase in aesthetic perception of the printed surface.

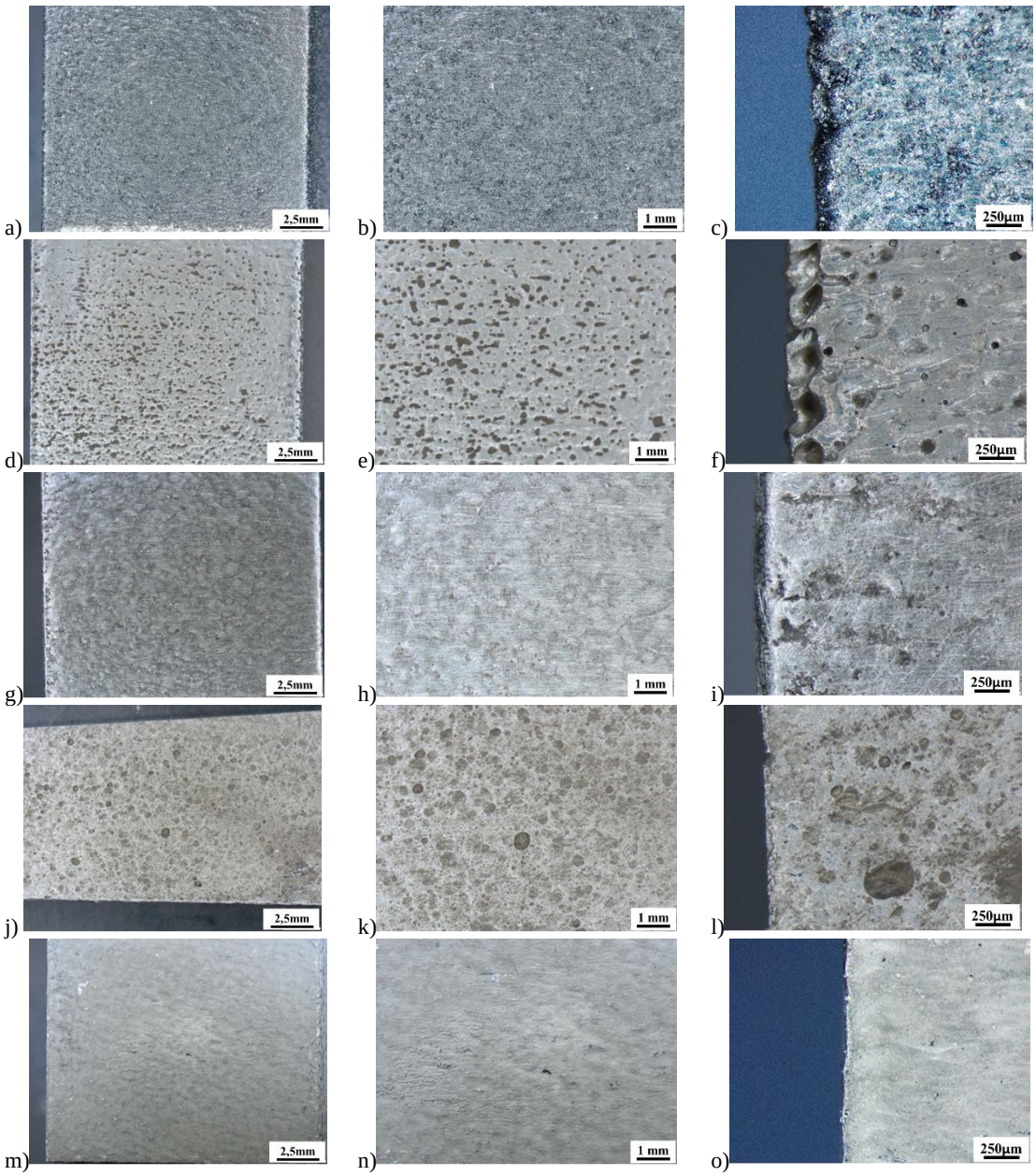

Figure 77: *Morphological analysis of AlSi10Mg Am cube surfaces with different “chemical” treatments: as printed (a,b,c,); chemical milling (d,e,f); Hirtisation®® (g,h,i); Green etching®® (j,k,l); DryLyte® (m,n,o). In detail, pictures (a,d,g,j) and (b,e,h,k) show morphological surfaces overviews (at 7x and 12,5 x magnification respectively), while (c,f,i,l) images focus on differences in cube edges after each surface treatment.*

For what concerns the stereo microscope analysis of “chemical” surface treatments (figure 77), all the surfaces looked generally smoother, especially with DryLyte®. In this case, the material

removal from the surface was homogeneous and accurate even up to the revealing of the printed layers (figures 77 i, o), sign that a particularly smooth surface was achieved.

Hirtisation® led to quite uniform surface and sharp edges but with small cavitation signs maybe due to the mutual movement between the part and the solution during the treatment.

The remaining two treatments, chemical milling (figure 77 d-f) and green etching® (figure 77 j-l) showed some defects on the surface. In detail, green etching® samples exhibited evident cavitation signs maybe due to a not correct soaking of the part in the chemical solution. On the other hand, chemical milling seemed to have attacked preferentially some points rather than others. It must be remembered that treatments as chemical milling and green etching® act uniformly on surface peaks and valleys, that means that whenever the etching liquid penetrates in a pre-existing hole (as gas porosity or printing defect), it continues to remove material in the surrounding area. Therefore, those pre-existing defects enlarge and increase in size.

Probably this is the reason behind the holes visible in chemical milled specimens. In particular, at the contour, in correspondence to the cube edge, an aggressive attack was noticed (figure 77f), since transition area between core and contour is generally characterized by a greater number of defects as gas porosities that were attacked and enlarged by the acid solution.

For a more punctual morphological comparison, SEM analysis was carried out.

The as printed surface (figure 78) is characterized by the waviness due to the nature of the process itself for which components are build layer by layer. Moreover, as already seen with stereo microscope (figure 76, b), not melted powder and balling are visible.

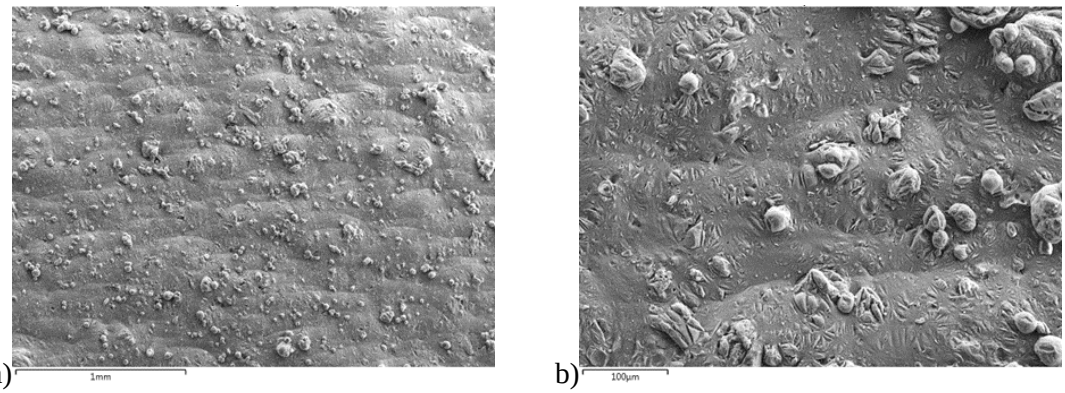

Figure 78: *Morphological analysis with SEM of as printed vertical surface of AM ALSi10Mg cube. a) 100x; b) 500x*

SEM analysis on surfaces that underwent barrel stone machining and shot peening confirmed what former stated with stereo microscope. In detail, any powder particle is visible. Barrel stone machining guarantees a generally smoother surface, while shot peened surfaces present the typical impact signs of the spheres. Obviously, these signs are smaller in figure 79c since the ceramic spheres in this case have a smaller diameter compared to the steel ones (figure 79d).

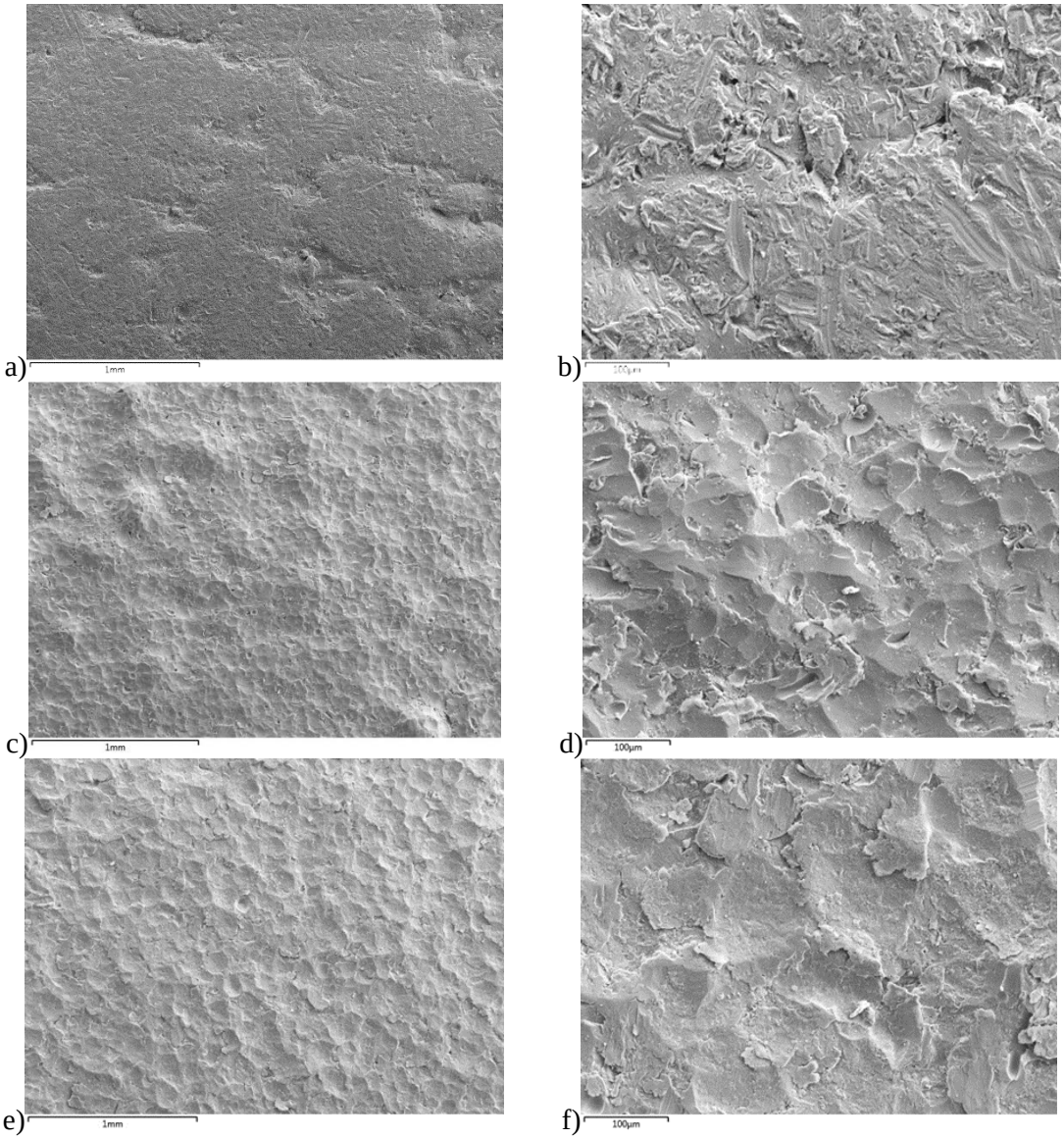

Figure 79: *Morphological analysis with SEM o of AM ALSi10Mg cube vertical surface with different treatments: barrel stone machining (a, b); shot peening with B60 ceramic beads (c, d); shot peening with S110 steel (e,f). Magnifications: 100x (a, c, e);500x (b, d, f).*

SEM morphological analysis on surface treated with "chemical" surface treatment gave some more information.

Starting from chemical milling, in addition to the holes seen at stereo microscope, selective removal of material was noticed in particular at melt pool boundaries. As shown in figure 80b, acid solution penetrated in correspondence to this region following the melt pool boundary. This phenomenon suggests a preferred attack to the aluminium phase instead of silicon. The reason behind this hypothesis is related to the melt pool microstructure. As described in paragraph 2.6.1, melt pool microstructure can be divided in three area:

- the core, characterized by an extremely fine microstructure of α–Al islands surrounded by inter-dendritic Si
- melt pool boundary, characterized by a wider microstructure (wider α–Al islands) due to the re-melting of the adjacent laser scan
- heat affected zone in which the inter-dendritic Si network is partially desegregated

In chemical milling, the solution preferentially removes material in the proximity of melt pool boundaries, where aluminium islands are wider and silicon network is interrupted, facilitating the reaction between acid solution and aluminium. This hypothesis was confirmed by SEM EDS analysis, which results are reported in Figure 81.

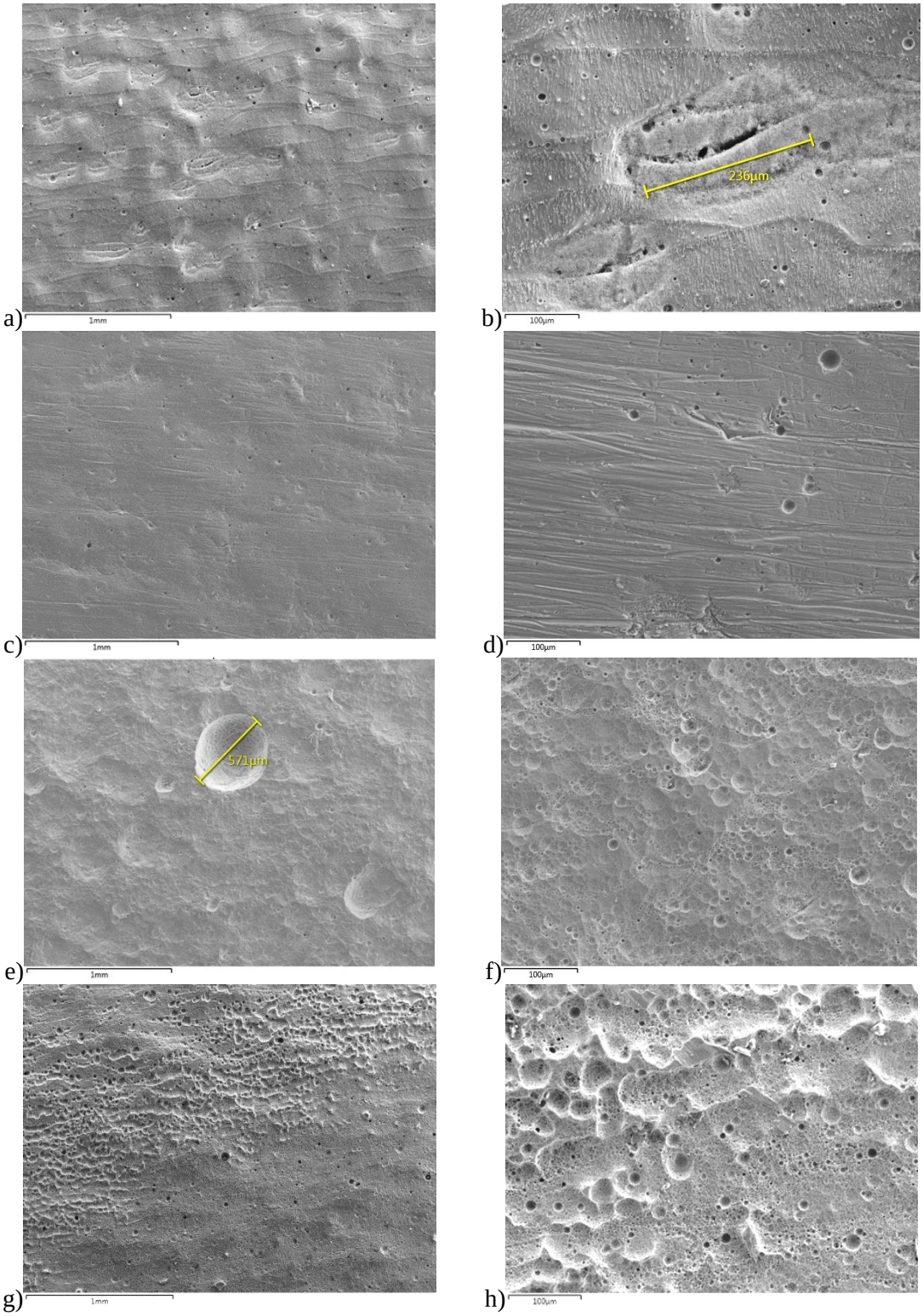

Figure 80: *Morphological analysis with SEM o of AM ALSi10Mg cube vertical surface with different "chemical" treatments: chemical milling (a, b); DryLyte® (c, d); Green etching® (e,f); Hirtisation® (g,h) . Magnifications: 100x (a, c, e, h);500x (b, d, f, h)*

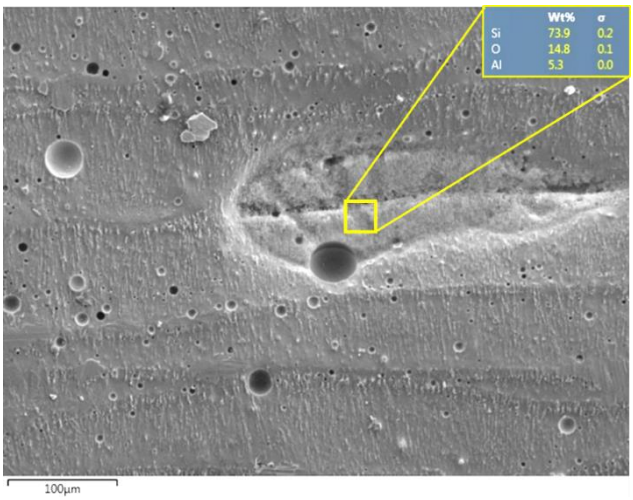

Figure 81: *SEM EDS analysis of AlSi10Mg AM vertical surface treated with chemical milling, highlighting the preferential attack on aluminium.*

SEM EDS analysis highlighted a prevalent percentage of Si than Al, which means that Al was preferentially removed by chemical reaction with acid solution.

DryLyte® was confirmed to be the "chemical" surface treatment that could lead to the smoothest surface (figure 80c, d). In this regard, porosities were seen to appear to the surface. DryLyte® works just on the peaks and not the valleys, guaranteeing a homogeneous surface. Moreover, this is the reason why, despite the surfacing of internal porosities, these defects remained confined without any increase in size (as seen in chemical milling figure 80a, b).

SEM analysis on green etching® (figure 80e, f) highlighted a non-uniform surface with cavitation signs that could reach 0,5 mm of diameter.

Same signs, but smaller in size, were noticed on Hirtisation® surface (figure 80g, h) as previously noticed also with stereo microscope. However, leaving this phenomenon aside since it could be due to a not correct treatment execution, the remaining surface portion looked homogeneous with just some small porosities.

Optical surface roughness analysis was carried out with confocal microscope to quantitatively evaluate the differences between the surface treatments and to establish the most promising ones. The measurements were made according to method described in paragraph 3.5. So, for each scanned area (2,3x2,7mm^2) the surface roughness in terms of Sa and Sz values was calculated with and without the application of a cut-off filter (of 0,8mm). Table 16 shows the results obtained. In detail, Sa micro and Sz micro values refer to the measurement with the application of the cut-off filter. Starting from as printed condition, just three surface treatments led to a roughness reduction, that were barrel stone machining, DryLyte® and Hirtisation®. The results, hence, confirmed the evaluation made after morphological analysis. With the remaining treatments, surface roughness didn't change a lot from as printed condition or even get a bit worse, as for green etching®. Same considerations can be made looking at Sa and Sz values with the application of the cut-off filter.

Treatment	Sa (µm)	Sz (µm)	Sa micro (µm)	Sz micro (µm)
As Printed	10	141	8	129
Barrel stone machining	4	109	3	109
Shot peening ceramic	10	136	7	99
Shot peening steel	11	171	8	142
Chemical Milling	11	146	8	120
DryLyte®	6	102	4	91
Green etching®	12	165	8	122
Hirtisation®	8	135	5	120

***Table 16**: Surface roughness measurements on the different surface treatments in comparison to as printed surface*

6.2 Rotating bending fatigue results

As a result of morphological analysis and surface roughness measurements, four surface treatments were chosen for a further investigation on the effects on fatigue resistance. The surface treatments considered for this study phase were:

- DryLyte®
- Hirtisation®
- Shot peening ceramic
- Shot peening steel

Despite the lower surface roughness achieved with barrel stone machining, shot peening was preferred because its industrialization was easier, having already a machine for shot peening. The eventual ceramic or steel mean was chosen with the supplier to be already applicable on the existing machine.

For each surface treatment, tensile and fatigue specimens were built in Z direction with gauge size properly over dimensioned, to achieve the correct gauge diameter after surface treatment application. Specimens underwent stress relief at 160°C for 6 hours (SR_160).

Graph in figure 82 shows the average tensile tests results for each treatment. Due to industrial policy, tensile and fatigue tests results will not be disclosed. Hence, as in previous chapters, all the results were normalized in relation to the average UTS value obtained with Z raw specimens.

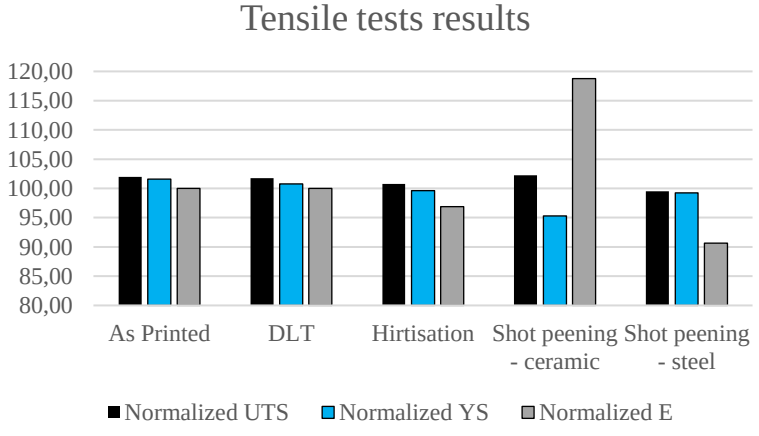

***Figure 82:** Tensile test results on vertical specimen in the different surface conditions.*

Not significant differences were observed from tensile tests results. All the specimens showed mechanical properties comparable to those relative to as printed samples. Shoot peening with ceramic led to a 20% increase in elongation. Nevertheless, this variance is included in the deviation typical of the SR_160 heat treatment, so it should not be considered as something to point out.

Rotating bending fatigue results in a double logarithmic graph are shown in figure 83. Three considerations can be made at a first look:

- Any specimen failed the test before 10^5 cycles.
- Cross signs corresponding to as printed specimens are small in number since, as happened in chapter 4, the minimum load of the rotating bending fatigue machine was reached. Anyway, fatigue limit was assumed to be around the value represented by the black arrow.
- Regardless the spheres material, shot peening treatments led to higher fatigue resistance than the one achieved with "chemical" surface treatments (DryLyte® and Hirtisation®).

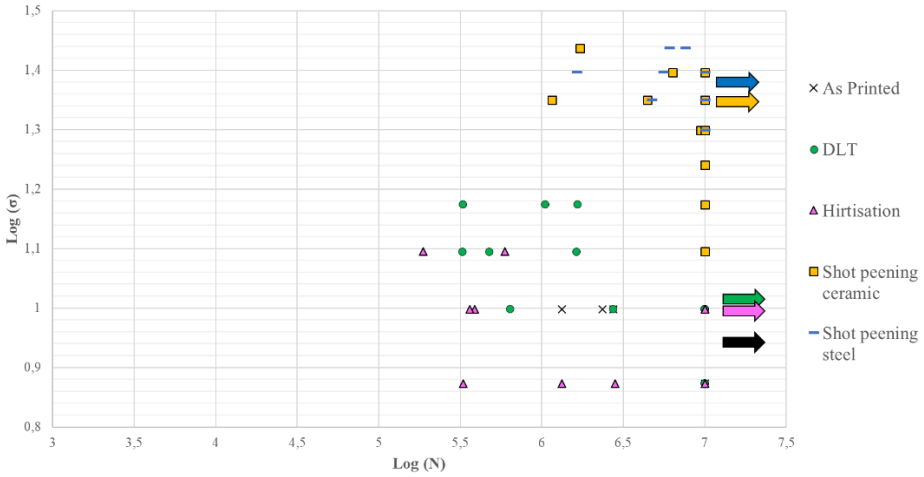

Figure 83: *Log-log graph of rotating bending fatigue results of specimens that underwent the different surface treatments.*

About the last point, a deepen consideration must be taken. Contrary to what expected, it resulted that DryLyte® and Hirtisation®, despite the lower surface roughness measured and the smoother surface morphology observed, did not improve fatigue behaviour of the part. On the contrary, shot peening almost tripled the as printed fatigue limit despite the lower surface roughness. The explanation of this phenomenon must be searched considering not only the surface quality, but also the consequence of surface treatment application to the samples.

For this reason, even in this case, fracture surfaces were analysed with both stereo microscope and SEM.

As already seen in the study at chapter 4, looking at fracture surface of as printed specimen (figure 84), fatigue crack initiates from the outer surface because of the high surface roughness.

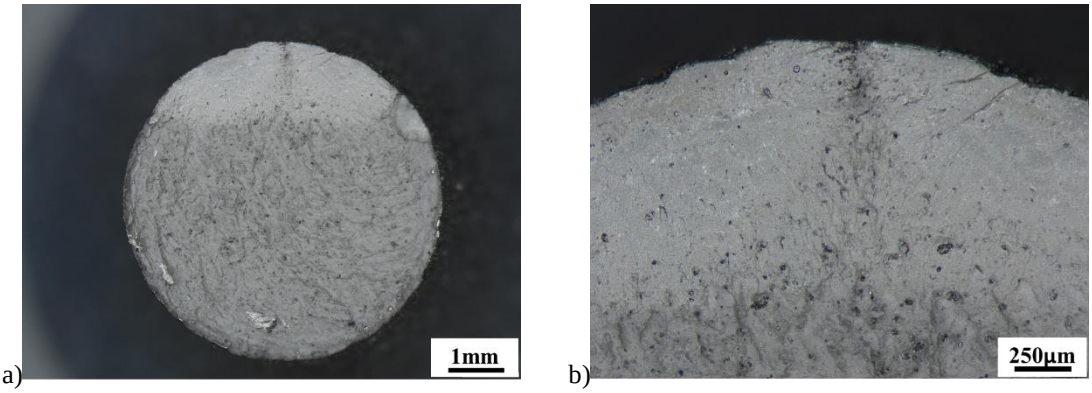

Figure 84: *Fracture surfaces pictures of as printed specimens. a) 12,5x; b)40x*

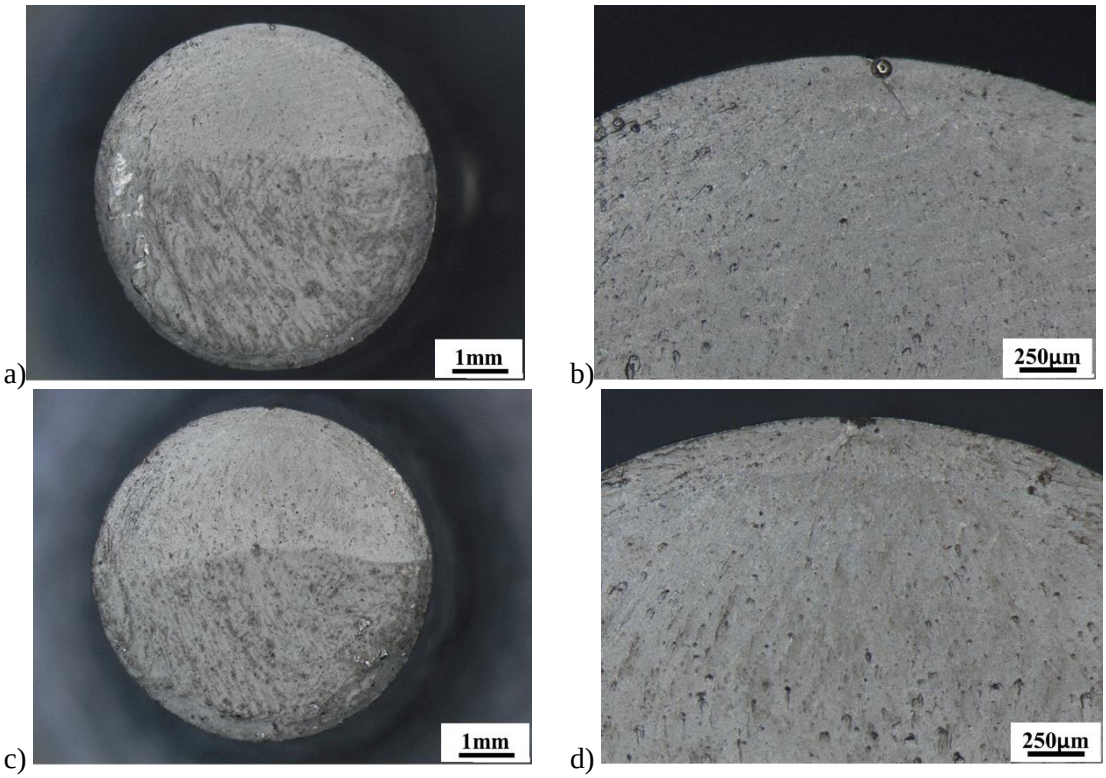

Figure 85: *Fracture surfaces pictures of DryLyte® specimens. a,c) 12,5x; b,d)40x*

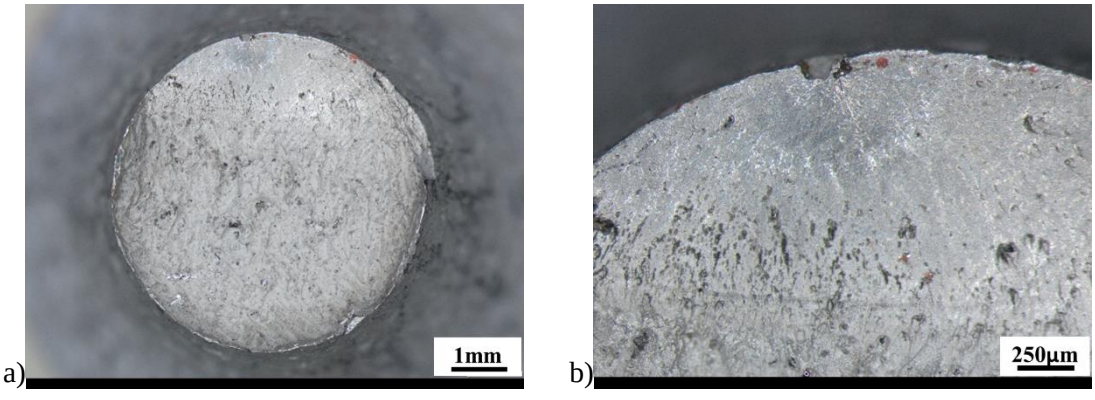

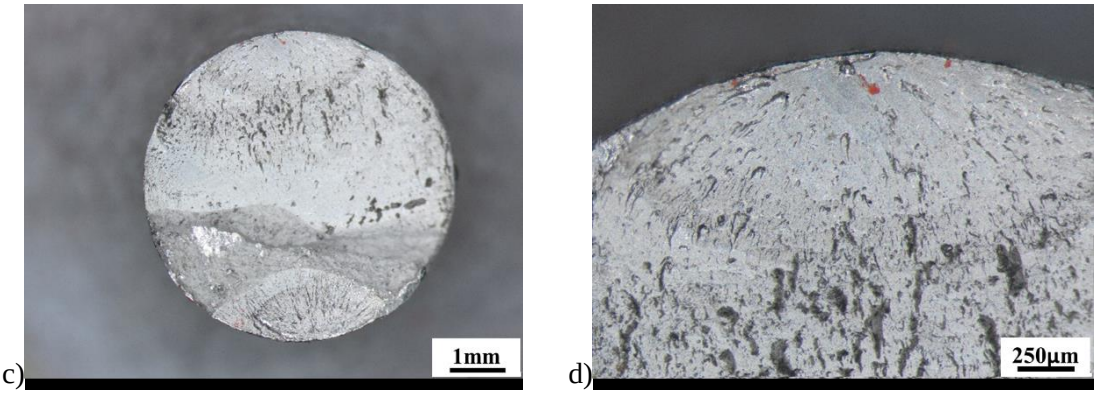

Figure 86: *Fracture surfaces pictures of Hirtisation®® specimens. a,c) 12,5x; b,d)40x*

Figures 85 and 86 show the fracture surfaces of rotating bending fatigue samples that were treated with DryLyte® and Hirtisation®. Starting from DryLyte® analysis, fatigue originates from pre-existing defects as porosities. In this case, defects are at the surface (Figure 85c, d) or just below the surface (figure 85a, b), while for Hirtisation® samples, fatigue could start both from pre-existing defects or in general from the surface due to the not homogeneous profile (figure 86).

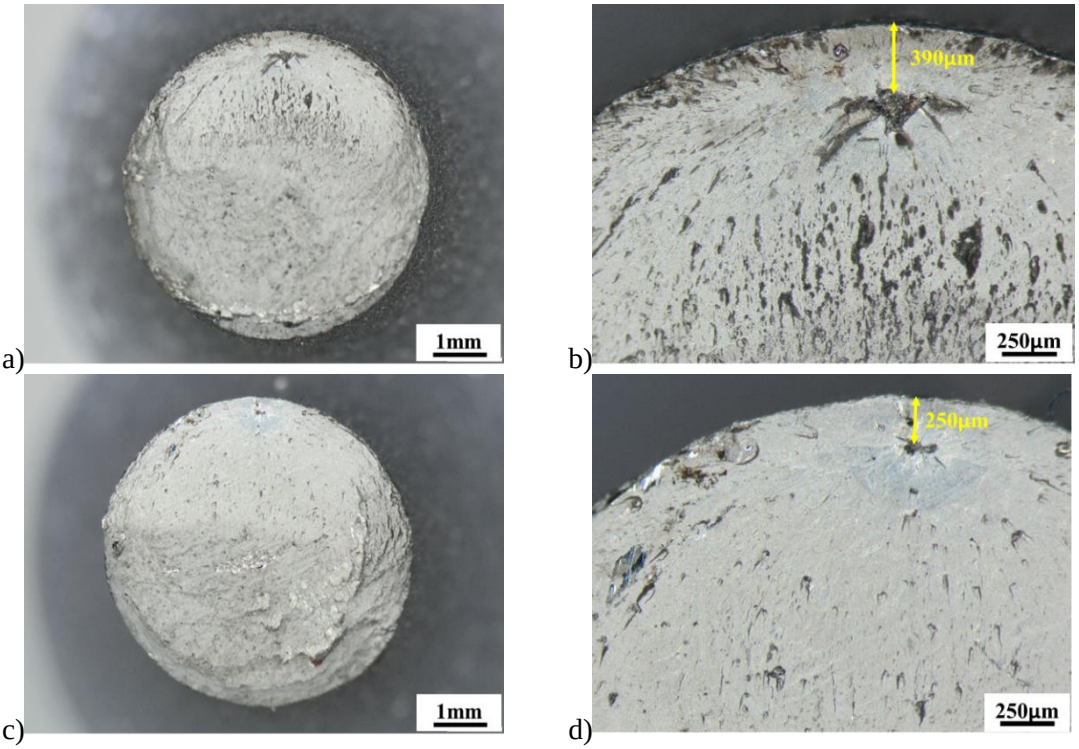

Figure 87: *Fracture surfaces pictures of specimens treated with shot peening (B60 ceramic beads) with indication of fatigue crack initiation and of its distance from the outer surface. a,c) 12,5x; b,d)40x*

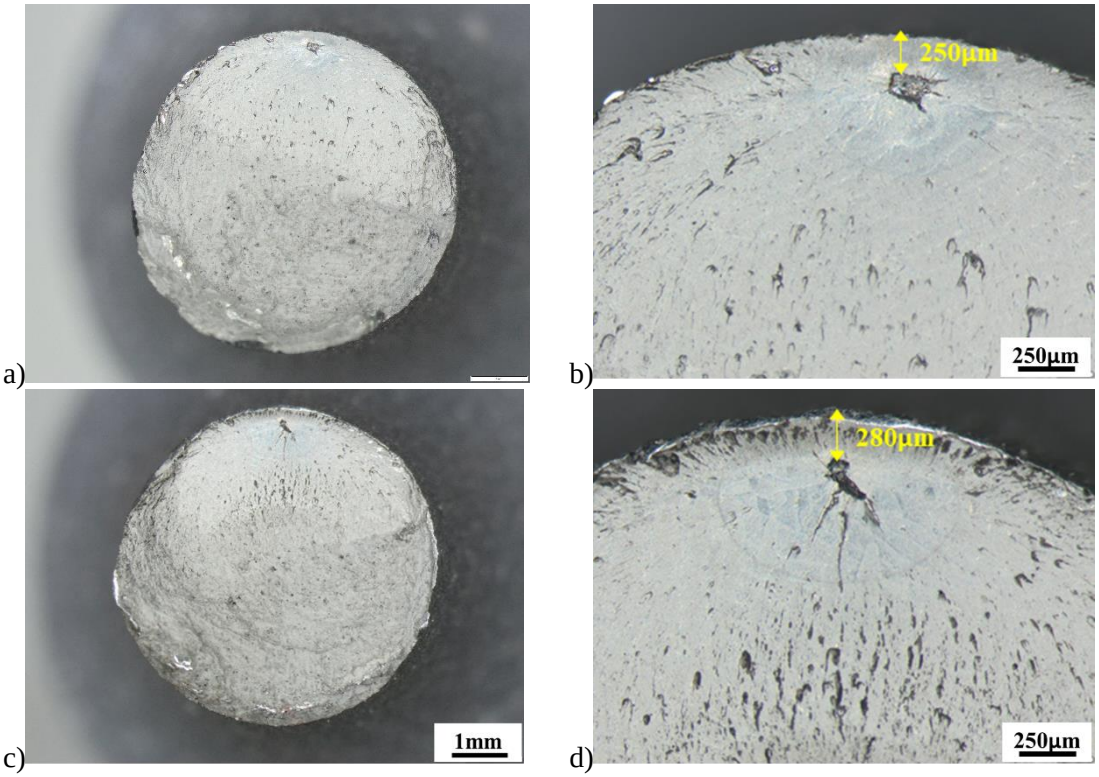

Figure 88: *Fracture surfaces pictures of specimens treated with shot peening (S110 steel) with indication of fatigue crack initiation and of its distance from the outer surface. a,c) 12,5x; b,d)40x*

Looking at fracture surface of shot peened specimens (Figures 87 and 88), regardless the mean material, it can be seen that the crack initiation shifted towards the sample core at distances around 250µm. Moreover, in almost all the cases, fatigue started from defects under the surface in the area highlighted in figure 89 by the dashed yellow circle and then it rapidly propagates on the fracture surface.

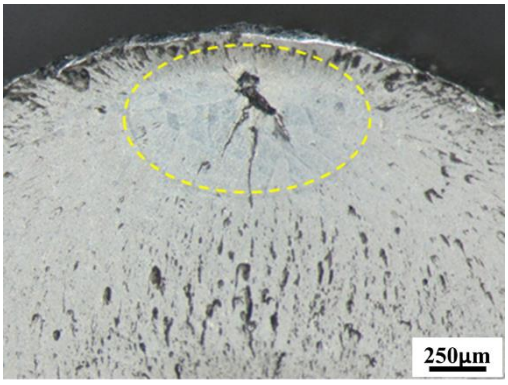

Figure 89: *indication of the fatigue propagation under the surface noticed on fracture surfaces of shot peened specimens.*

Fracture surfaces were further analysed with SEM. Figures 90 and 91 show a direct comparison between the different surface treatments.

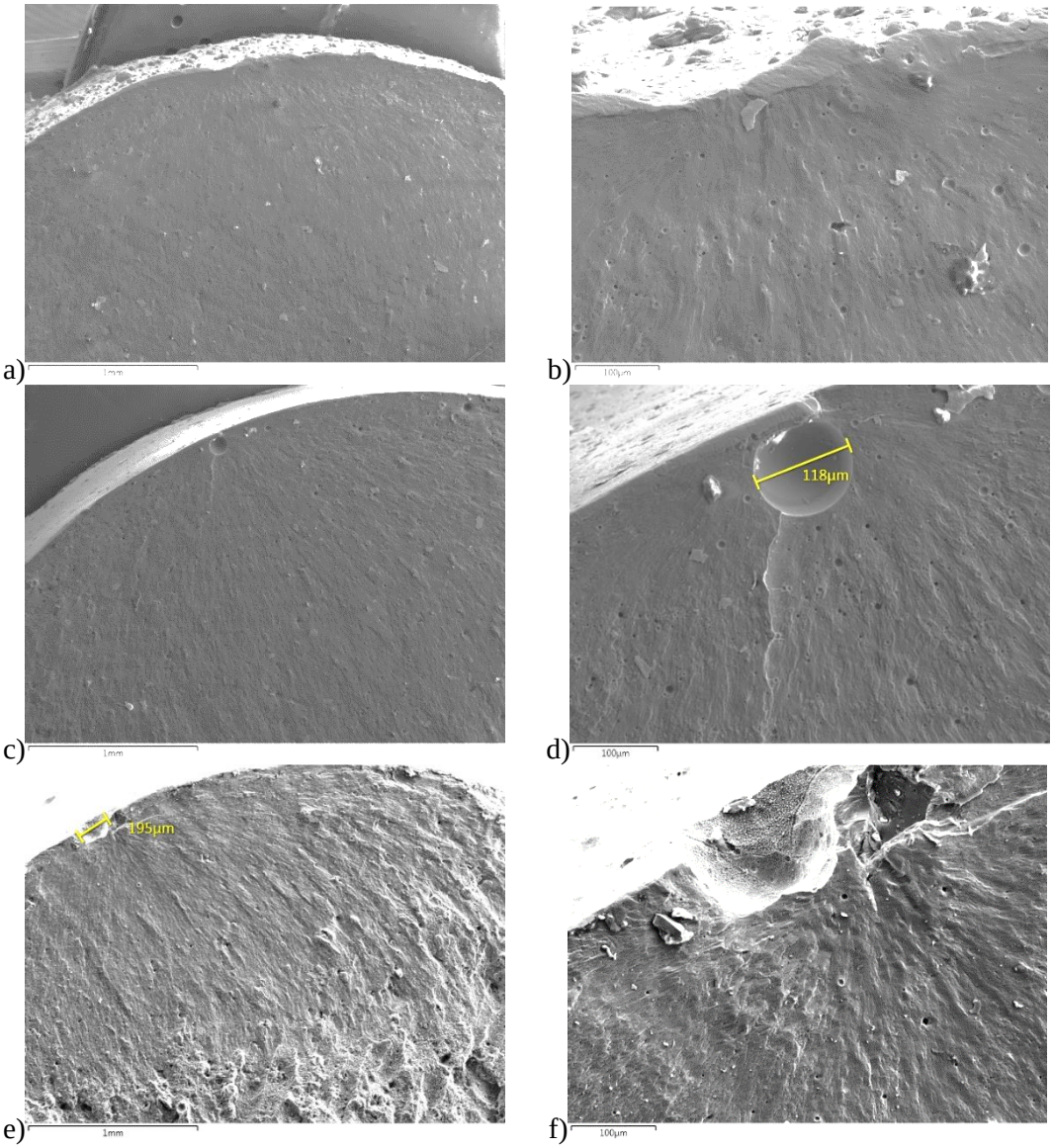

Figure 90: *SEM analysis of fracture surfaces of fatigue samples in the following conditions: as printed (a,b), DryLyte® (c,d), Hirtisation®® (e,f).*

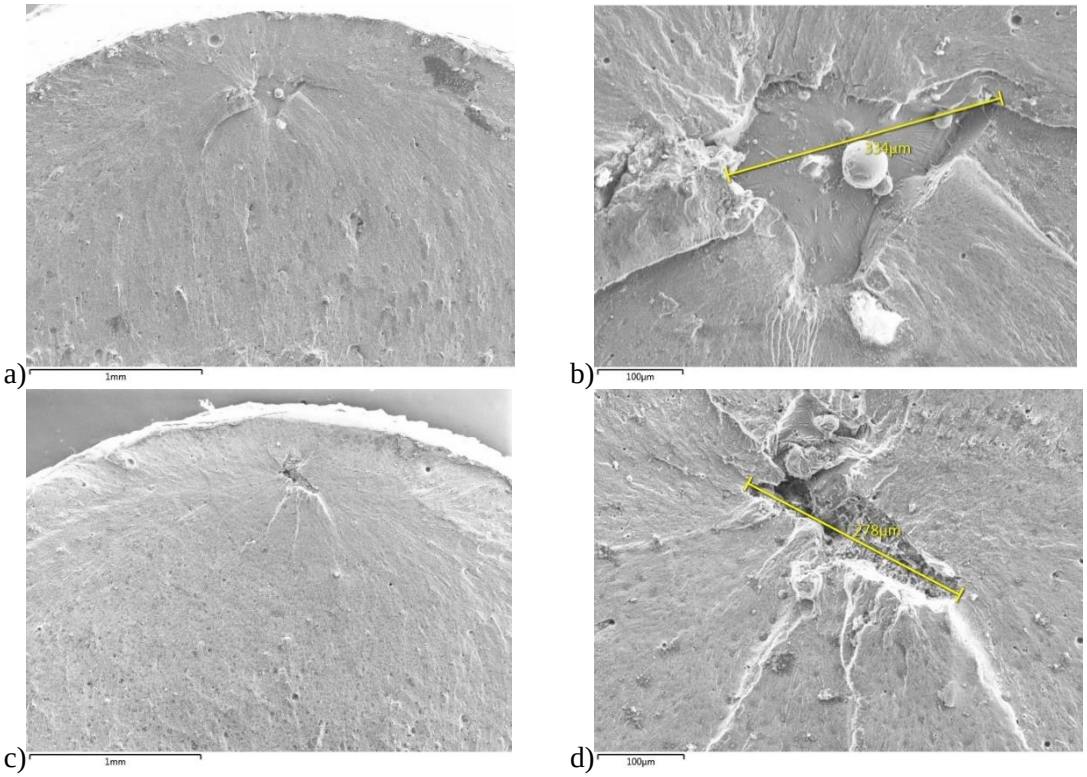

Figure 91: *SEM analysis of fracture surfaces of fatigue samples in the following conditions: shoot peened with B60 ceramic beads (a,b), shoot peened with S110 steel (c,d).*

SEM confirmed what previously seen with stereo microscope. For shot peened specimens, fatigue life was improved despite the surface roughness that was comparable to as printed specimens and definitely higher than DryLyte® samples. This enhancement, so, is not attributable to the surface finishing achieved, but to the pre-compression state given by shot peening to as printed surfaces. This pre-compression condition guaranteed a higher fatigue resistance and moved fatigue crack initiation towards the sample core. Hence, fatigue started later, and the limit measured was three times the one obtained on as printed specimens.

Another important observation can be made looking at SEM pictures. Comparing DryLyte® and shot peened fracture surfaces it can be seen that fatigue initiates from different kinds of defects. In DryLyte® sample (figure 90c, d) fatigue started from spherical porosity while in shot peened specimens (figure 91) from irregular shape defects as lack of fusion with significant dimensions (until 0,35mm). Irregular shape defects are generally detrimental to fatigue resistance because they introduce a higher stress intensification factor than the one related to a spherical porosity. Despite this, DryLyte® specimens exhibited a significantly lower fatigue resistance than the one of shot peened samples. This phenomenon is another factor that underlines the major influence of the surface pre-compression state on fatigue resistance.

6.3 Summary and Conclusions

Different surface treatments were considered in this chapter, both mechanical (barrel stone machining and shot peening with B60 ceramic beads and S110 steel shots) and chemical (chemical milling, DryLyte®, Hirtisation® and green etching®).

Firstly, surface treatments were evaluated by morphological analysis and surface roughness measurements. By morphological analysis (both at stereo microscope and SEM), barrel stone machining and DryLyte® led to the smoothest surfaces. This result was also confirmed by Sa and Sz measurements, where these two surface treatments were the only ones with a roughness significantly lower than the one measured on as printed surfaces.

Chemical milling and green etching® were not further considered due to the problems observed on surfaces. These two surface treatments exploit a solution that attacks both surface valleys and peaks, resulting in enlargement of pre-existing defect as those at core-contour interface.

The second step of the analysis was focused on effects of surface conditions on tensile test and fatigue resistance. DryLyte®, Hirtisation® and shot peening (both with ceramic and steel beads) were considered, in comparison to as printed specimens. Despite the promising results obtained with barrel stone machining, this treatment was not further investigated. Shot peening was preferred.

While no differences on static mechanical properties were observed, a significant deviation in fatigue results was achieved with the different surface treatments. In detail, DryLyte® and Hirtisation® led to similar low fatigue limits with defects towards the outer surface as driving factors in fatigue crack initiation. On the other hand, with shot peening application, fatigue limit was more than doubled if compared to as printing results. This thanks to the surface compression state given by shot peening that moves the fatigue origin towards the sample core, increasing the fatigue resistance.

CHAPTER 7
CORROSION BEHAVIOUR OF AM AlSi10Mg PARTS COMPARED TO OTHER Al ALLOYS

Considering the application in the automotive sector, also the working environment of the printed components must be taken into account during the design phase. For this reason, the corrosion resistance of the alloy in the different environments is another important aspect to evaluate. Several research have been conducted on this topic, paying particular attention to the corrosion resistance of Al-Si AM parts in salty water [102]. Yang Y. et al. stated that in the not heat treated condition micro galvanic couples establish between the small cathode, represented by the Si network in the as-printed microstructure, and the large anode (the Al matrix). These micro galvanic couples lead to the formation of a protective oxide film on the component surface, hindering the corrosion propagation and justifying the high corrosion resistance of Al-Si AM parts [103].

After the application of a T6 heat treatment, the change in the microstructure with Si particles uniformly distributed in the wide aluminum matrix promotes the corrosion spread and reduces the corrosion resistance of the part [104].

Another important factor influencing the corrosion behavior of a component is its surface condition. Generally, the higher is the surface roughness the lower is the corrosion resistance [105]. For what concerns this topic, Leon A. et al. compared the corrosion behavior between AM AlSi10Mg specimens with as-printed surface and with polished surface, proving the higher resistance of the polished samples [106].

This study has the aim of going deeper into the corrosion analysis on AM AlSi10Mg components by introducing different conditions and environments. AlSi10Mg specimens were subjected to different heat treatments and surface treatments to evaluate their effects on the corrosion resistance in comparison to other common Aluminum alloys typically used in casting or in plastic deformation processes. All the alloys were tested by immersion in several fluids directly connected to the automotive sector to evaluate their behavior in their actual working environment.

The corrosion was quantitatively estimated by the calculation of the corrosion rate, defined as microns of corroded material per year, to have a numerical and objective comparison between AM AlSi10Mg and the other Al alloys.

7.1 Immersion tests at room temperature

NaCl 5%

At first, the samples with the different materials have been partially soaked in salty water to have a direct comparison between the specimen portions in contact with the liquid and with the air. Figure 92 shows as-built AlSi10Mg samples pictures before and after the corrosion test. The yellow rectangles indicate the soaked portion.

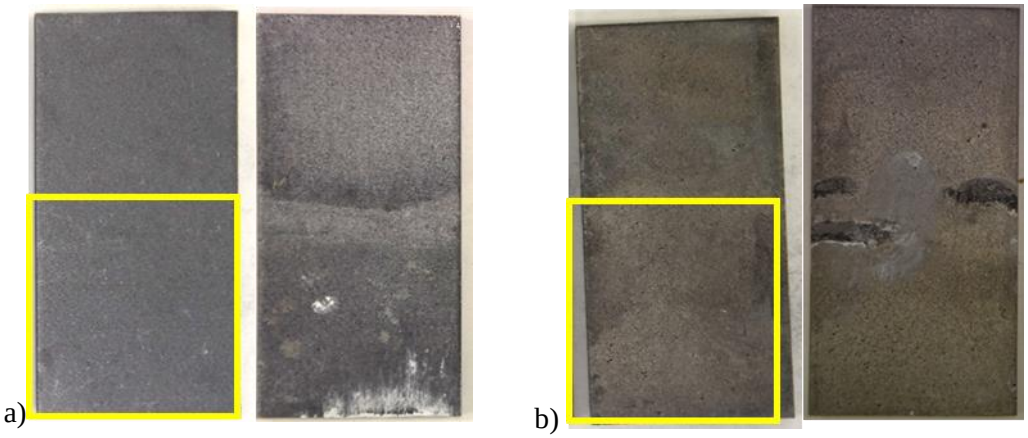

Figure 92*: surface comparison of as built AlSi10mg specimens with stress relief (a) and T6 (b) heat treatments before and after immersion in NaCl (50%)*

Stress relieved samples were characterized by deposition of corrosion products on the specimen surface. SEM analysis confirmed presence of corrosion products in the form of aluminum oxides, as demonstrated by EDS study (Figure 93).

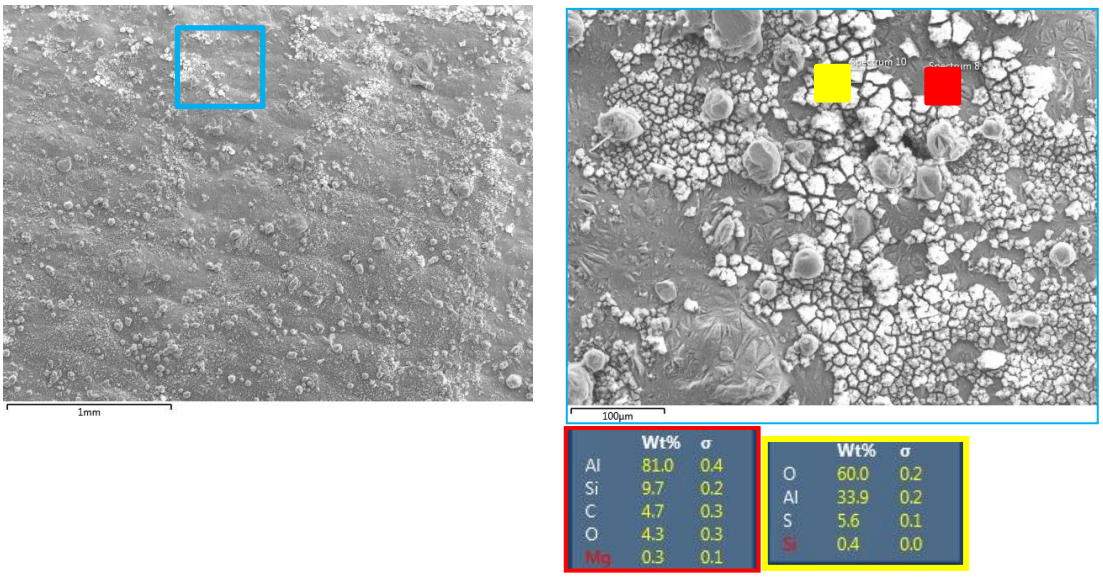

Figure 93*: SEM and EDS analysis of corrosion products found on stress relieved AlSi10Mg specimen after 30 days immersion in NaCl (5%)*

This area was further investigated by sectioning the sample end etching it to reveal the microstructure. As can be seen in Figure 94, the corrosion has infiltrated in the sample, selectively removing material in correspondence of the melt pool borders, regions more reactive as grain boundaries. Moreover, this behavior is justified by the coarser microstructure at the melt pool boundaries and by the partial dissociation of the Si network in correspondence of the heat affected

zone. In fact, being silicon the noblest element, α-Al is preferentially corroded. Therefore, the Si network interruption at the HAZ facilitates the corrosion along the melt pool boundaries. At the same time, the progression towards the single melt pool core may be hindered by the fine microstructure and by the oversaturated α-Al phase, where the enhanced presence of Si in solid solution (due to the high solidification rate achieved in L-PBF process) guarantees a higher corrosion resistance.

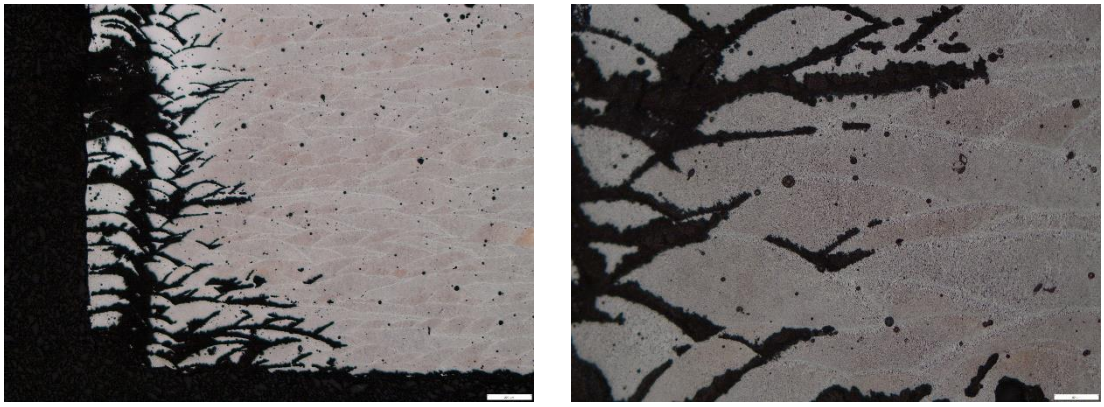

***Figure 94**: selective corrosion propagation on stress relieved as built AlSi10Mg specimens*

For what concerns as built AlSi10Mg T6 heat treated (Fig.92b) the corrosion phenomenon can be noted especially at the liquid-air interface, area that is more reactive due to the oxygen presence. This zone was characterized by the deposition of corrosion products on the sample surface and by the material removal that is associated to a more generalized corrosion. SEM and EDS analysis (figure 95) confirmed this hypothesis, detecting presence of aluminum oxide.

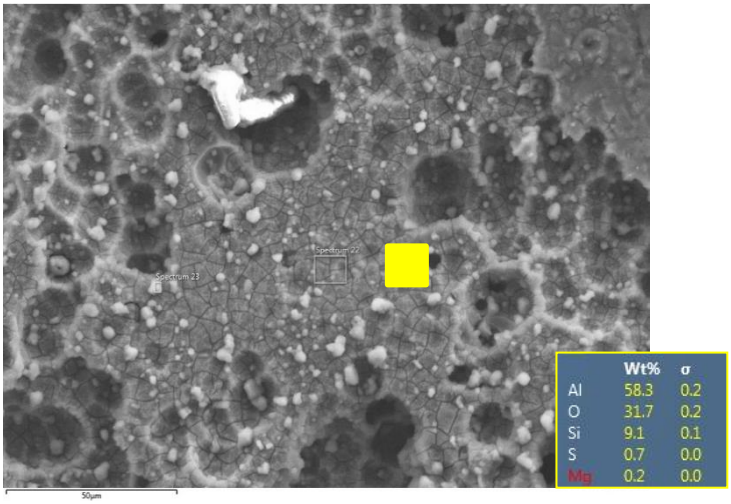

***Figure 95**:SEM and EDS analysis of the T6 as built AlSi10Mg specimen after immersion test in NaCl (5%) in correspondance of the liquid-air interface. The surface has aluminum oxide and is generally corroded.*

The sample was sectioned in correspondence of the liquid-air interface to evaluate the extent of the corrosion. Figure 96 shows the presence of generalized corrosion. This mechanism is different from the one seen in the stress relieved specimen, because of the different microstructure achieved after solution annealing. In fact, the Si particles become uniformly distributed in the Al matrix, promoting a wider and more homogeneous corrosion reaction with aluminum matrix.

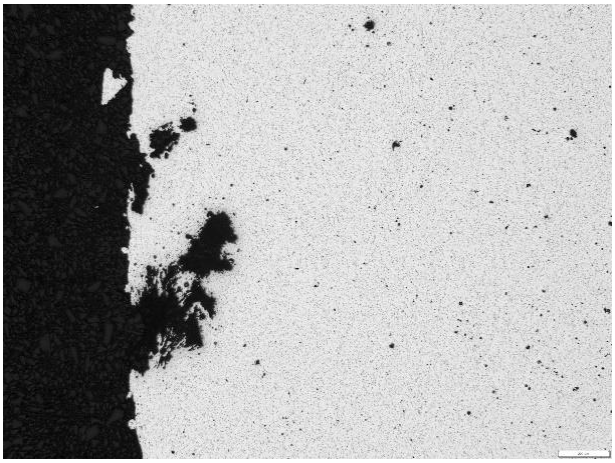

***Figure 96**: section of T6 as built AlSi10Mg specimen after immersion test in NaCl (5%). The corrosion propagated towards the inner part of the sample for 0,5mm*

Figure 97 displays the condition of the surfaces before and after the partial immersion in NaCl (5%) of AlSi10Mg specimens with DryLyte® and sand blasting surface treatment. Both present general oxidation on the soaked area with local corrosion products.

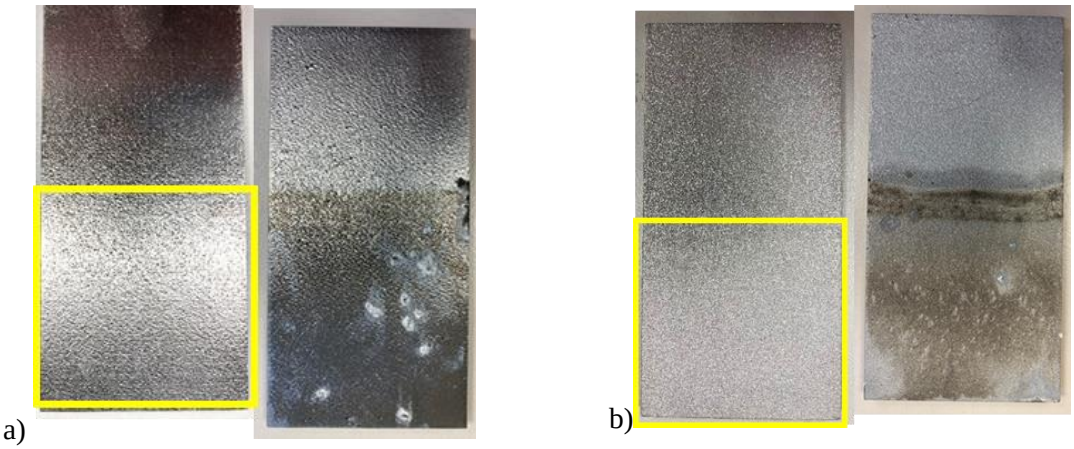

***Figure 97**: surface comparison of AlSi10mg specimens with DRYLYTE® (a) and sand blasting (b) surface tratment before and after immersion in NaCl (50%)*

For what concerns the DryLyte® specimen, the finishing process itself may foster the local corrosion. In fact, DryLyte® process may up rise porosities located under the sample skin to the surface. These may act as preferential sites for corrosion initiation.

This hypothesis was proved by SEM analysis in Figure 98 that shows the surface morphology before and after the immersion test. It can be seen that before soaking, DryLyte® led to a generally smooth surface with local circular craters corresponding to porosities. These points were replaced by corrosion products after the corrosion test in salty water.

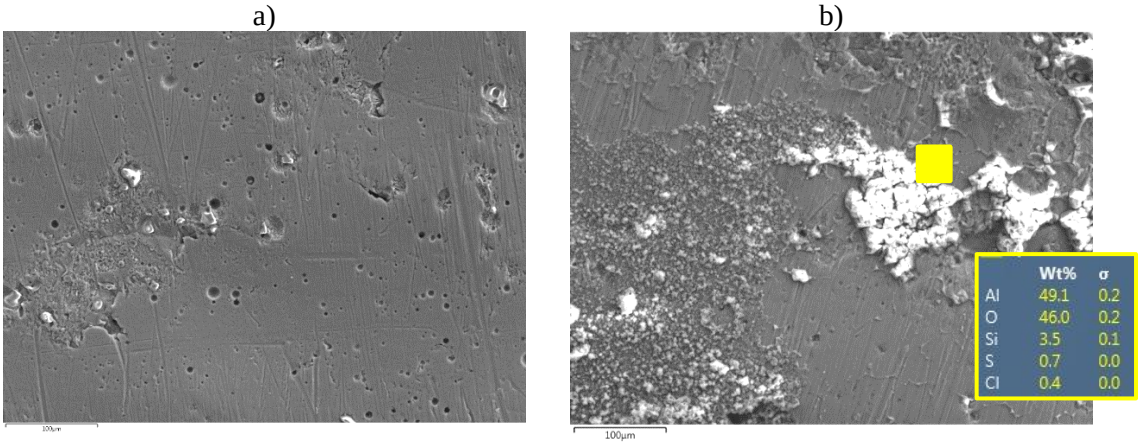

***Figure 98**: SEM and EDS analysis of corrosion products found on DryLyte® AlSi10Mg specimen before (a) and after (b9 30 days immersion in NaCl (5%)*

The metallographic analysis (Figure 99) of both the surface finished specimens displayed a mechanism of corrosion propagation comparable to the one seen in Figure 94, since they were characterized by the same heat treatment (stress relief) and, therefore, by the same microstructure.

Nevertheless, the DryLyte® specimen exhibited a wider corrosion towards the sample core, passing through the border. On the other hand, in the sand blasted ones, the corrosion stopped within the border without any further advance. This may be due to a defect modification (closure) as a result of the plastic deformation coming from the sand blasting process, that may decrease the defects on the sample surface, hence, the sites of the corrosion initiation.

Moreover, sand blasting may confer a small cold work hardening on the surface influencing the corrosion behavior.

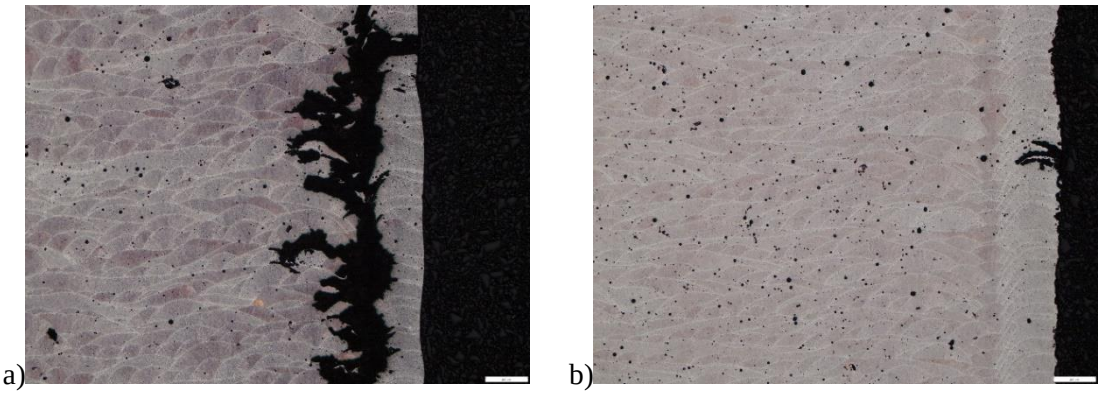

***Figure 99**: corrosion propagation on DRYLYTE® (a) and sand blasted (b) AlSi10Mg specimens. In both the specimens, corrosion selectively attacks the melt pool borders.*

Among the other aluminum alloys considered for a direct comparison with the AM AlSi10Mg parts, A356 T6 showed the worst corrosion resistance (Figure 100). While the EN AW 1050, EN AW 5083, EN AW 3003 alloys didn't show any corrosion mark in the metallographic analysis, and EN AW6082 was characterized just by slight corrosion at the air-liquid interface, A356 T6 alloy suffered by pitting corrosion. Figures 100(e, f) exhibit the propagation of corrosion along the already existing shrinkage borders with selective attack to the dendrites.

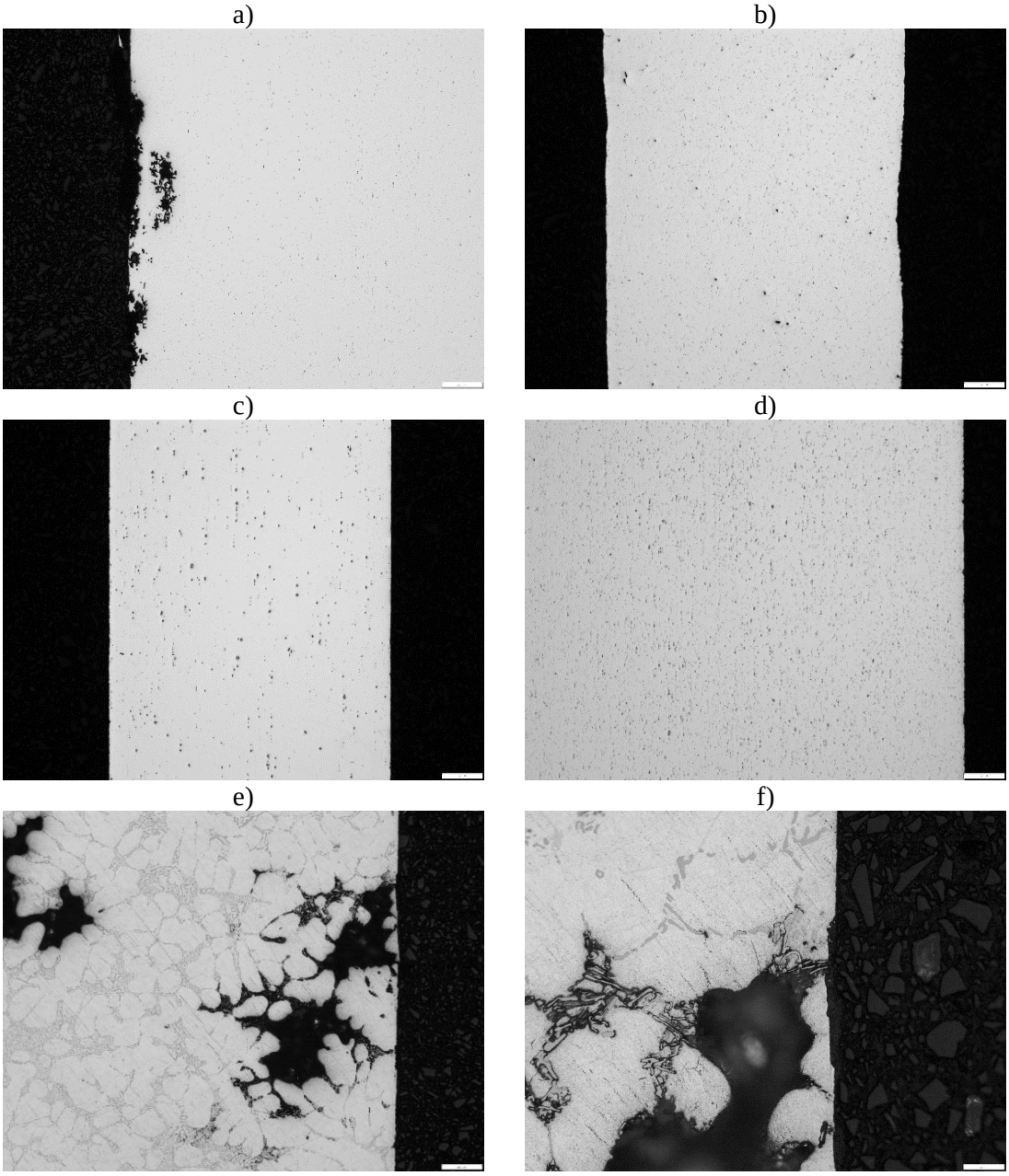

***Figure 100**: metallographic sections of EN AW6082 (a), EN AW1050 (b), EN AW5083 (c), EN AW3003 (d) and A356 T6 (e, f) specimens after immersion in NaCl (%) for 30 days.*

In addition to the visual inspection, the corrosion behavior was numerically estimated by the calculation of corrosion rate on specimens completely soaked in NaCl (5%) at room temperature.

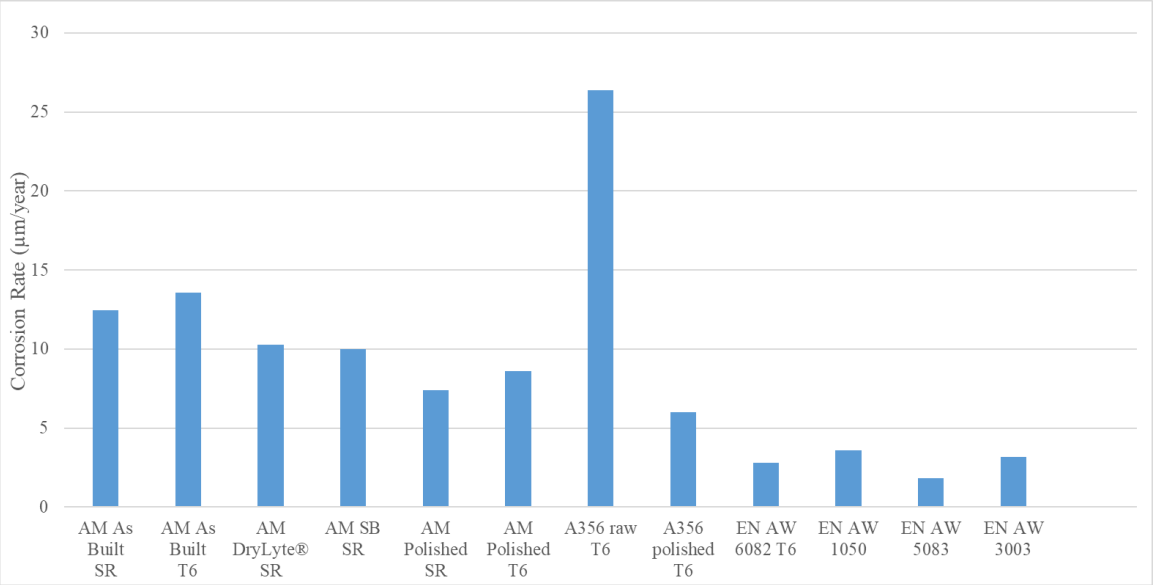

***Figure 101**: corrosion rate measurements of all the tested alloys in all the conditions after immersion test in NaCl (5%) for 30 days.*

The graph in figure 101 shows the corrosion rate measured according to ASTM G31-72. AM AlSi10Mg components, regardless of the surface condition and the heat treatment, exhibited a greater corrosion resistance than A356 T6 as cast surface specimens obtained from sand casting. On the other hand, both AM and A356 parts were characterized by a greater corrosion rate compared to the wrought aluminum alloys.

The reason behind such a worst corrosion behavior of A356 alloy may be related to several factors as, for example, the different microstructure. AlSi10Mg printed specimens have finer microstructure generated by rapid solidification, while A356 cast samples show the typical casting dendritic microstructure in which the Al matrix is generally wider, hence, the Al is more easily attacked [107].

Focusing on AlSi10Mg components, it can be noticed that the application of a surface treatment led to an enhancement of the corrosion resistance. This phenomenon could be explained by the diminution of the corrosion trigger points related to the decrease of the surface roughness, even though, as shown before, DryLyte® treatment could up rise to the surface under-skin defects as porosities that could become points for corrosion start.

In confirmation of this hypothesis, the best results were achieved on polished samples. This is consistent with what found in literature. For example, Leon et al. [108] observed a significant corrosion resistance reduction of the unpolished additively manufactured part in comparison to the polished one, justifying this fact with the higher surface roughness and with the higher amount of surface cavities of the as built specimen.

For what concerns the heat treatment, according to the results, T6 led to a slightly higher corrosion rate. This is consistent with the wider and more generalized corrosion found in the specimen section and with other studies. For example, Sander G. et al. [107]carried out immersion tests in NaCl (3,5%) and measured a greater weight loss in T6 specimen rather than stress relieved or as printed samples.

However, in general the corrosion rates measured in this study are lower than those typical of other construction materials. For example, considering a low carbon steel (C <0,3; Cr <0,6; Ni <2,25; Mn <1,75), according to "Corrosion resistance tables" [109], its corrosion rate is one order of magnitude greater (about 500 µm per year).

5W40, Oil for active suspensions, cooling mixture (glycol 50%), automotive gasoline

After the immersion test for 30 days in these different fluids, none of the specimens exhibited any morphological change on the surface, sign that no corrosion occurred on any material.

Corrosion rate measurements confirmed the outcome of the visual inspection. The different Al alloys in 5W40, oil for active suspensions, Glycol (50%) and automotive gasoline at room temperature were characterized by a corrosion rate below 5µm per year. A corrosion rate value around 5 µm/year was considered as neglectable, since the weight difference calculated was inside the measure error range. As a consequence, these immersion tests led to the conclusion that none of these fluids was corrosive to any of the specimens at room temperature.

The graph in figure 102 underlines in addition the different results obtained with total immersion in salty water (NaCl 5%). It is evident that NaCl (5%) represents a more corrosive environment especially for additive manufactured AlSi10Mg and cast A356 components, in comparison to the other fluids.

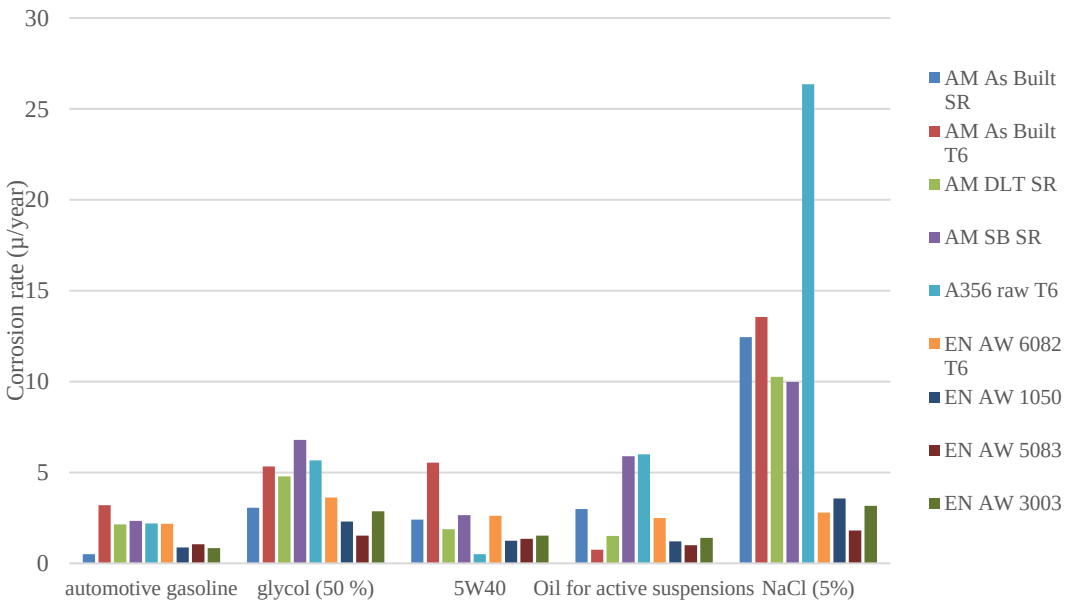

***Figure 102**: corrosion rate comparison of the alloys soaked in the different fluids at room temperature for 30 days.*

7.2 Immersion tests at T=90°C

The immersion tests of the various specimens in Glycol (50%), 5W40 and oil for active suspensions were repeated at a temperature of 90°C for 30 days, to better simulate the working temperature of these fluids in the vehicle, hence, to understand the true corrosion behavior of the alloys in their working environment.

Even in this case, no sign of corrosion was noticed on any sample surfaces, exception made for those specimens soaked in Glycol (50%). In this case, an oxide layer formed on the surfaces, regardless the alloy or the surface treatment. The reasons of this oxidation may lay on the fact that there wasn't a direct concentration control of the liquid. Despite the fluid level was checked all along the test duration, the water in the glycol solution (50% concentrated) might have evaporated a bit, causing a variation of the immersion test conditions. Another hypothesis is that, more simply, the Glycol temperature plays an important role on the corrosion behavior of Al alloys.

This phenomenon was partially confirmed by the corrosion rate calculation. In fact, as shown in Figure 103, glycol (50%) led to a generally higher corrosion rate in comparison to the other fluids at 90°C. However, almost all the values, except for as built additive manufactured T6 specimens (AM as built T6), were around or below 5µm per year, and therefore to be considered as negligible.

As built AlSi10Mg specimens with T6 heat treatment showed a surprisingly high corrosion rate value in all the three fluids tested at high temperature, despite the absence of corrosion products on the surface. The reason behind this phenomenon is not clear. Maybe the maintenance of AlSi10Mg T6 specimens at high temperature for a sufficiently long time fosters a general and uniform corrosion all over the surfaces. Corrosion may be here once again facilitated by the AlSi10Mg T6 microstructure discussed in the previous paragraph.

Graphs in figure 104 (a, b and c) compare the results obtained in the first step of the analysis (at room temperature) and at 90°C for each fluid. It is pointed out that none of these fluids represents a corrosion environment for the tested alloys (with exception of the AM As Built T6 specimens at high temperatures, which behavior is still under investigation).

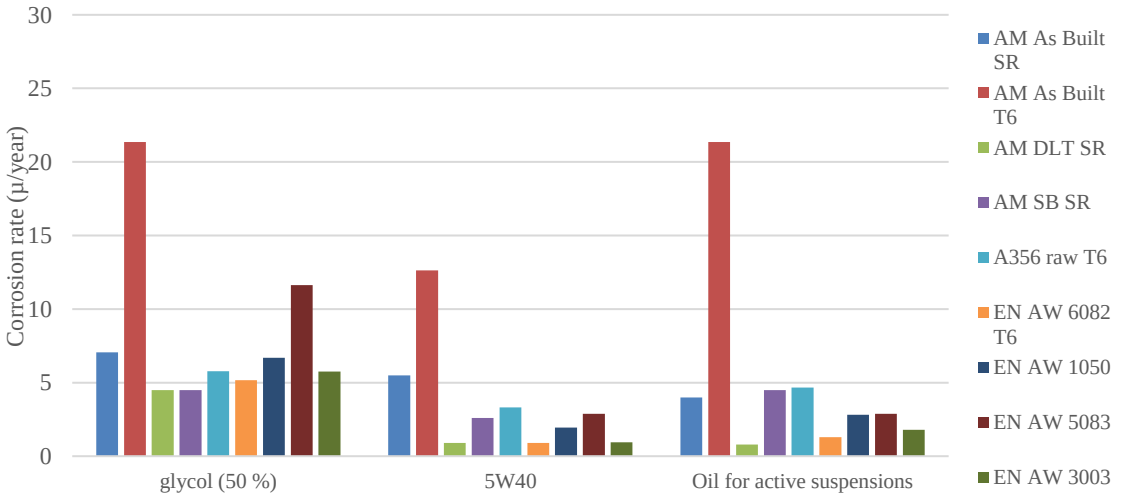

Figure 103: *corrosion rate comparison of the alloys soaked in the glycol (50%), 5W40 and oil for active suspensions at 90°C for 30 days.*

a)

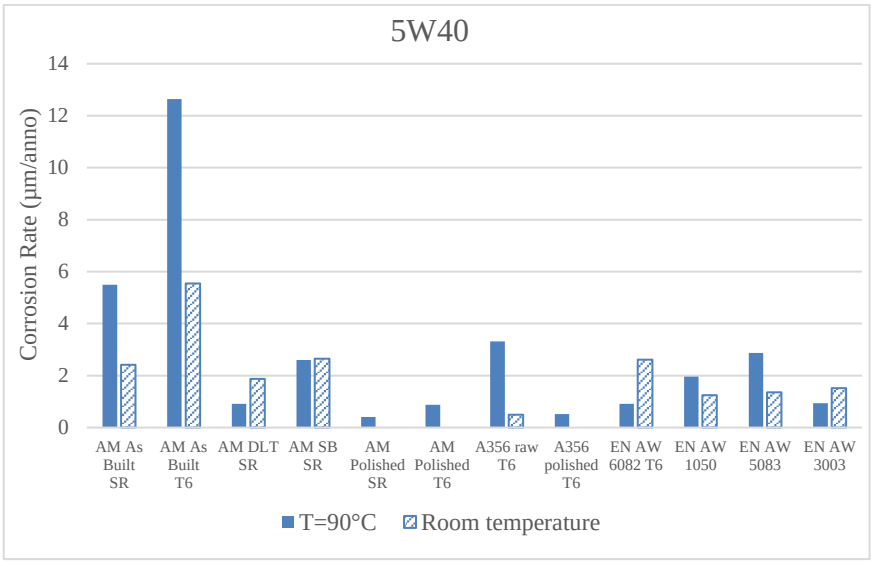

b)

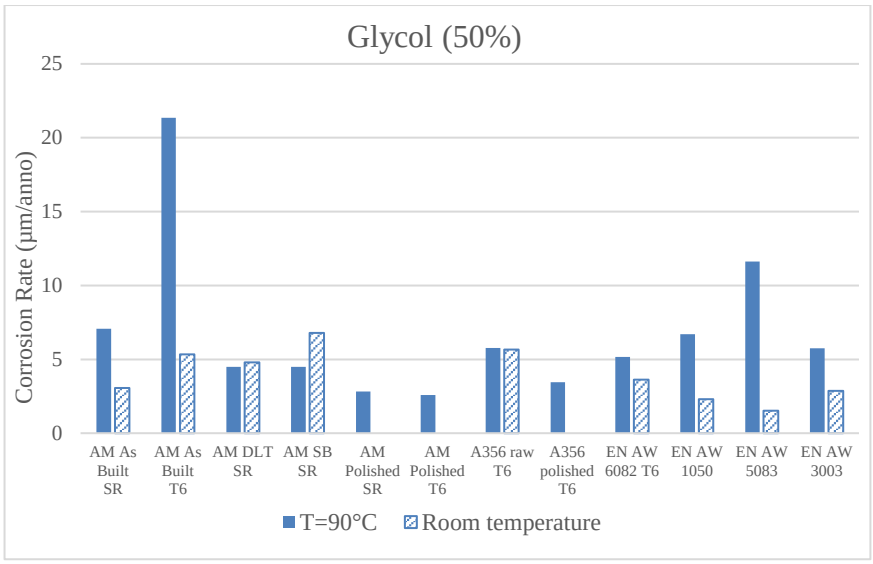

c)

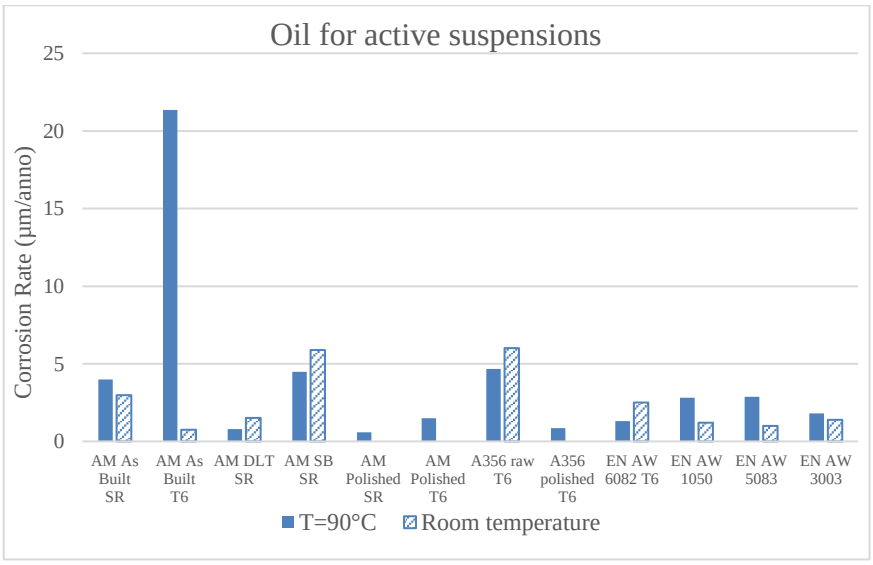

***Figure 104**: corrosion rate comparison of the alloys soaked in 5W40 (a), glycol 50% (b), oil for active suspensions (c) at 90°C and at room temperature. With the exception of AM As Built T6 specimen, all the other samples exhibit a negligible corrosion rate value in both the conditions (room and high temperature)*

7.3 Summary and Conclusions

AM AlSi10Mg alloy was in this chapter evaluated in relation to its corrosion resistance in fluids that could represent corrosive environment in automotive sector. Corrosion behavior was here numerically evaluated by calculating corrosion rate after total immersion of samples in fluids as salty water (5% NaCl), oil for active suspensions, oil 5W40, automotive gasoline (E10), glycol (50%). For a direct comparison, other aluminium alloys normally adopted in tradition technologies were tested (Cast A356 T6, EN AW6082, EN AW1050, EN AW5083 and EN AW3003). The different corrosion mechanisms were evaluated by visive inspection and by microstructural analysis of sample sections.

The immersion tests in oil for active suspensions, oil 5W40 and glycol (50%) were then repeated at a higher temperature to better simulate the working environment inside the vehicle.

Additive manufactured AlSi10Mg specimens with stress relief heat treatment soaked in NaCl (5%) showed a selective corrosion at the melt pool borders, while T6 samples were characterized by a more generalized corrosion. This was due to the different microstructures. In stress relieved parts the microstructure is very fine in the melt pool cores and becomes slightly coarser at the borders. Hence, corrosion preferentially propagates at the melt pool borders. On the other side, T6 specimen exhibits a uniform microstructure, thanks to solution annealing, with Si particles dispersed in the Al matrix. Therefore, in this case, aluminum matrix is more easily attacked, and corrosion widely spreads. This is the main reason behind the slightly greater corrosion rate measured in T6 specimens in comparison to the stress relieved ones.

Additive manufactured AlSi10Mg specimens with surface treatments (DryLyte® and sand blasting), were characterized by a corrosion rate slightly lower than the one of as built samples. DryLyte® process, although led to lower roughness, up rose to the surface porosities that acted as trigger points for corrosion initiation. Sand blasting uniformed the surface and probably modified the surface defects, reducing the probability of corrosion initiation. Anyway, the best results in terms of corrosion rate for AlSi10Mg components were obtained on polished specimens, where the smooth and passivated surface hindered the corrosion initiation and propagation.

Corrosion rate measurements showed that additive manufactured AlSi10Mg parts had a greater corrosion resistance in comparison to A356 T6 obtained from sand casting. Anyway, both the alloys (from AM and sand casting) were characterized by a higher corrosion rate than those related to the other aluminum alloys.

None of the specimens in any alloy and with any surface or heat treatment conditions soaked at room temperature in automotive gasoline, 5W40, Glycol (50%) and oil for active suspensions showed corrosion on the surface. This phenomenon was confirmed by the negligible corrosion rates measured.

The immersion tests in 5W40, Glycol (50%) and oil for active suspensions at 90°C resulted in the absence of corrosion, with corrosion rates below 5µm per year. Only AM T6 component without any surface treatment were related to a surprisingly high corrosion rate, despite no corrosion products were observed on the surfaces. This phenomenon is still under investigation.

CHAPTER 8:
FROM PROCESS INVESTIGATION TO INDUSTRIAL APPLICATION

All the previous chapters summarize the way the work was set for a thorough study of L-PBF technology, with a focus on those aspects that could be needed to answer to eventual different project requests.

In this regard, heat treatment analysis led to the choice of a HT portfolio that could cover different mechanical characteristics ranges, e.g., high UTS and low elongations and vice versa.

The material dynamic response, for some of these conditions, was evaluated through the wide rotating bending fatigue test campaign to find fatigue limits that could be needed during the design phase of a component, similarly to corrosion resistance study. Here, the main aim was to find a method to evaluate objectively the behavior of parts built with AM in comparison to those produced with traditional technologies. In this way, even the future working environment of the component is considered and studied, helping the eventual production transition to a new technology as L-PBF.

The process parameters evaluation aimed not only to find the best compromise between productivity and mechanical properties, but also to offer alternative parameters combinations that may be used according to the singular needs.

Therefore, at the end of this wide study, it was possible to furnish different "recipes" for producing components with AM. In parallel, the knowledge on this technology grew together with the awareness on advantages, limits and problems raised all over the path towards AM introduction into a productive sector.

AM, despite its global growth, nowadays still lacks numerous reference standards. This aspect becomes a problem whenever associated to a productive industry.

In this respect, it is worth remembering that today a major part of production is linked to traditional technologies (casting, extrusion, etc.) that were born with an advance that gave enough time for these process to be studied, evaluated and described with solid standards.

Therefore, the AM "youth" requires an internal definition of technical specifications inside each company, to guarantee an adequate process control.

Hence, even in Ferrari, the in-depth study presented in previous chapters was useful for a better comprehension of the process and for a delineation of standards that act at the same time as process control and study continuation.

Starting from the HT portfolio evaluation and thanks to an opportune statistic, limits to mechanical characteristics were defined. These limits have to be checked for each build JOB. Here, together with the component, also tensile and density specimens are always printed to intercept eventual problems occurred during the printing or during the HT.

At the same time, the constant check tracks the historical production trend in terms of mechanical characteristic. This is useful, for example, to highlight process drifts or machine problems, to evaluate, for example, if maintenance is required.

In parallel, some of the output machine parameters were chosen to be checked for each build JOB to verify if the process proceeded correctly.

All of these analyses are related to the process. For what concerns a component, its validation must be accompanied by more specific checks.

First of all, a sort of technical feasibility study must be set for each considered component. Starting from the mechanical characteristics for part design, a build JOB is printed. The part characteristics are then analyzed through destructive tests to verify if they meet the required specifications.

Part satisfying specifications will be then validated with specific tests on benches and vehicles.

On top of production certification some specific tests can be carried out as:

- X-ray and CT scan to evaluate defect level and part geometry
- Liquid Penetrant Inspection (LPI) to highlight eventual cracks and surface defects
- 3D measurement to evaluate deformations

Of course, being L-PBF a new technology, at the beginning great amount of information are generally collected by exploring the process to have a solid control on it. Once a sufficient familiarity is built, coherent decisions could be taken about which checks are absolutely necessary and which ones don’t give any additional information. On the other side, keeping learning from AM observation, other technical specifications may be draft, in relation to other requirements evaluated along the project.

CONCLUDING REMARKS

This thesis is focused on a deep investigation of LPBF process applied to AlSi10Mg alloy from several point of views. The aim of this work was to gain familiarity with this new technology for introducing it inside a structured automotive company not just for prototypes but also for production. Therefore, in view of printing components that should satisfy the most varied requirements, several aspects were considered and investigated, to be ready to answer to different design specifications.

The main conclusions of this work can be summarized as follows:

- By heat treatment investigation, it was possible to define a wide mechanical characteristic range that could satisfy several structural requirements. Stress relief remains the preferable heat treatment since it reduces residual stresses without having a significant impact on the component production cycle. In this regard, it has to be reminded that AM competitiveness lays also in the post process steps reduction, thanks to the possibility of printing net-shape components. Hence, decreasing heat treatments hours helps also in the part cost reduction.
  Moreover, it has been highlighted that, whenever high mechanical characteristics are required, the lower is the SR temperature, the higher are mechanical characteristics, which remain similar to as printed ones, due to the low impact on the microstructure. In this regard, SLM process itself leads to an extremely fine microstructure caused by high solidification rate, which is the main reason behind the high mechanical properties achieved on AlSi10Mg alloy. On the other side, it was demonstrated the significant responsiveness of AM AlSi10Mg alloy to SR temperature, achieving significantly different mechanical properties, thus enlarging the mechanical characteristics range to be given to CAD and CAE department for a component evaluation.

- Fatigue resistance is affected by factors as orientation (XY sample showed better behavior then Z ones), surface conditions and metallurgical quality in terms of defect presence. Regarding this last point, it was demonstrated that defects dimension plays an important role in fatigue resistance. An area threshold value, equal to 2000μm^2, was found to be a good indicator for fatigue test outcome, since almost all the not-survived specimens (KO) were characterized by a greater frequency of defects with higher dimensions. This phenomenon, eventually, could be exploited as a predictive method for component fatigue resistance, simply by printing samples in the proximity of a stressed area of the part.
  Nevertheless, whenever required, fatigue resistance can be improved by applying post processes as shot peening, since it was proven its beneficial effects thanks to the superficial compressive state.

- To boost productivity, it is possible to work on process parameters, as done in this work. Thanks to this study different parameter combinations were detected, which led to building time reduction, and consequently cost reduction, while maintaining the same mechanical properties.
  Another important concept resulted from this work is the low impact of VED variation on part density and quality. Hence, attention should be put whenever optimized parameters are researched by using this metric. Parameters with similar VED were found

to be characterized by different density and defect types, affecting subsequently fatigue resistance.
This phenomenon was highlighted by rotating bending fatigue tests, since, as stated before, they are significantly influenced by dimension and morphology of the defects generated during the printing phase. As a result, parameter combinations comparable in terms of mechanical properties were characterized by different fatigue behavior due to different defects observed by image analysis.

- In corrosion analysis, from the comparison with cast A356 (T6 condition), AM AlSi10Mg specimens exhibited a higher corrosion resistance, making AM a good candidate for re-designing automotive components normally produced with gravity casting. For a further improvement, post processing surface treatment as sand blasting could be applied whenever corrosion is defined as a design parameter, thanks to the lower corrosion rate measured.

- Despite its significant economic growth, SLM is still considered as a new technology. Hence, deep study is required to delineate process strengths and limits and to acquire the knowledge needed for its industrial application. Process expertise is necessary also to overcome problems as the lack of unified standards. Only by experience, internal technical specifications could be defined with the aim of both process and product control. The key is the continuous learning from process observation to acquire ever deeper knowledge and to enlarge AM application in productive industries.

BIBLIOGRAPHY

[1] ASTM International, ""ASTM F2792-12A, Standard Terminology for Additive Manufacturing Technologies." 2012.

[2] D. Chen, S. Heyer, S. Ibbotson, K. Salonitis, J. G. Steingrímsson, and S. Thiede, "Direct digital manufacturing: definition, evolution, and sustainability implications," *J Clean Prod*, vol. 107, Nov. 2015, doi: 10.1016/j.jclepro.2015.05.009.

[3] M. Mani, K. W. Lyons, and S. K. Gupta, "Sustainability Characterization for Additive Manufacturing," *J Res Natl Inst Stand Technol*, vol. 119, Oct. 2014, doi: 10.6028/jres.119.016.

[4] Terry Wohlers and Tim Gornet, "History of Additive Manufacturing," *https://wohlersassociates.com/wohlers-report-2016-downloads/*, 2014.

[5] https://www.3dprintingmedia.network/the-additive-manufacturing-market-2019/, "Global additive manufacturing market 2019 worth over $10 billion," Jan. 2020.

[6] S. A. M. Tofail, E. P. Koumoulos, A. Bandyopadhyay, S. Bose, L. O'Donoghue, and C. Charitidis, "Additive manufacturing: scientific and technological challenges, market uptake and opportunities," *Materials Today*, vol. 21, no. 1, Jan. 2018, doi: 10.1016/j.mattod.2017.07.001.

[7] S. Yang, W. Min, J. Ghibaudo, and Y. F. Zhao, "Understanding the sustainability potential of part consolidation design supported by additive manufacturing," *J Clean Prod*, vol. 232, Sep. 2019, doi: 10.1016/j.jclepro.2019.05.380.

[8] M. Ashour Pour, S. Zanoni, A. Bacchetti, M. Zanardini, and M. Perona, "Additive manufacturing impacts on a two-level supply chain," *International Journal of Systems Science: Operations & Logistics*, vol. 6, no. 1, Jan. 2019, doi: 10.1080/23302674.2017.1340985.

[9] A. Kirchheim, H.-J. Dennig, and L. Zumofen, "Why Education and Training in the Field of Additive Manufacturing is a Necessity," in *Industrializing Additive Manufacturing - Proceedings of Additive Manufacturing in Products and Applications - AMPA2017*, Cham: Springer International Publishing, 2018. doi: 10.1007/978-3-319-66866-6_31.

[10] https://www.twi-global.com/technical-knowledge/faqs/what-is-3d-printing/pros-and-cons, "WHAT ARE THE ADVANTAGES AND DISADVANTAGES OF 3D PRINTING?".

[11] "ASTM G31 - 72(2004) Standard Practice for Laboratory Immersion Corrosion Testing of Metals".

[12] I. Gibson, D. W. Rosen, and B. Stucker, *Additive Manufacturing Technologies*. Boston, MA: Springer US, 2010. doi: 10.1007/978-1-4419-1120-9.

[13] H. Brooks, A. Rennie, T. Abram, J. McGovern, and F. Caron, "Variable Fused Deposition Modelling – analysis of benefits, concept design and tool path generation," in *Innovative Developments in Virtual and Physical Prototyping*, CRC Press, 2011. doi: 10.1201/b11341-83.

[14] ASTM International, "Committee F42 on Additive Manufacturing Technologies," 2009.

[15] J. Fiocchi, A. Tuissi, and C. A. Biffi, "Heat treatment of aluminium alloys produced by laser powder bed fusion: A review," *Mater Des*, vol. 204, Jun. 2021, doi: 10.1016/j.matdes.2021.109651.

[16] N. T. Aboulkhair, N. M. Everitt, I. Ashcroft, and C. Tuck, "Reducing porosity in AlSi10Mg parts processed by selective laser melting," *Addit Manuf*, vol. 1–4, Oct. 2014, doi: 10.1016/j.addma.2014.08.001.

[17] M. Langelaar, "Topology optimization of 3D self-supporting structures for additive manufacturing," *Addit Manuf*, vol. 12, Oct. 2016, doi: 10.1016/j.addma.2016.06.010.

[18] N. Read, W. Wang, K. Essa, and M. M. Attallah, "Selective laser melting of AlSi10Mg alloy: Process optimisation and mechanical properties development," *Materials & Design (1980-2015)*, vol. 65, Jan. 2015, doi: 10.1016/j.matdes.2014.09.044.

[19] E. O. Olakanmi, R. F. Cochrane, and K. W. Dalgarno, "A review on selective laser sintering/melting (SLS/SLM) of aluminium alloy powders: Processing, microstructure, and properties," *Prog Mater Sci*, vol. 74, Oct. 2015, doi: 10.1016/j.pmatsci.2015.03.002.

[20] N. Read, W. Wang, K. Essa, and M. M. Attallah, "Selective laser melting of AlSi10Mg alloy: Process optimisation and mechanical properties development," *Materials & Design (1980-2015)*, vol. 65, Jan. 2015, doi: 10.1016/j.matdes.2014.09.044.

[21] F. Trevisan *et al.*, "On the Selective Laser Melting (SLM) of the AlSi10Mg Alloy: Process, Microstructure, and Mechanical Properties," *Materials*, vol. 10, no. 1, Jan. 2017, doi: 10.3390/ma10010076.

[22] S. Catchpole-Smith, N. Aboulkhair, L. Parry, C. Tuck, I. A. Ashcroft, and A. Clare, "Fractal scan strategies for selective laser melting of 'unweldable' nickel superalloys," *Addit Manuf*, vol. 15, May 2017, doi: 10.1016/j.addma.2017.02.002.

[23] J.-P. Choi *et al.*, “Densification and microstructural investigation of Inconel 718 parts fabricated by selective laser melting,” *Powder Technol*, vol. 310, Apr. 2017, doi: 10.1016/j.powtec.2017.01.030.

[24] C. Kamath, B. El-dasher, G. F. Gallegos, W. E. King, and A. Sisto, “Density of additively-manufactured, 316L SS parts using laser powder-bed fusion at powers up to 400 W,” *The International Journal of Advanced Manufacturing Technology*, vol. 74, no. 1–4, Sep. 2014, doi: 10.1007/s00170-014-5954-9.

[25] M. Simonelli, Y. Y. Tse, and C. Tuck, “Effect of the build orientation on the mechanical properties and fracture modes of SLM Ti–6Al–4V,” *Materials Science and Engineering: A*, vol. 616, Oct. 2014, doi: 10.1016/j.msea.2014.07.086.

[26] A. Popovich, V. Sufiiarov, I. Polozov, E. Borisov, D. Masaylo, and A. Orlov, “Microstructure and mechanical properties of additive manufactured copper alloy,” *Mater Lett*, vol. 179, Sep. 2016, doi: 10.1016/j.matlet.2016.05.064.

[27] T. Kurzynowski, A. Pawlak, and I. Smolina, “The potential of SLM technology for processing magnesium alloys in aerospace industry,” *Archives of Civil and Mechanical Engineering*, vol. 20, no. 1, Mar. 2020, doi: 10.1007/s43452-020-00033-1.

[28] P. Konda Gokuldoss, “Design of next-generation alloys for additive manufacturing,” *Material Design & Processing Communications*, vol. 1, no. 4, Aug. 2019, doi: 10.1002/mdp2.50.

[29] A. Bandyopadhyay and B. Heer, “Additive manufacturing of multi-material structures,” *Materials Science and Engineering: R: Reports*, vol. 129, Jul. 2018, doi: 10.1016/j.mser.2018.04.001.

[30] T. DebRoy *et al.*, “Additive manufacturing of metallic components – Process, structure and properties,” *Prog Mater Sci*, vol. 92, Mar. 2018, doi: 10.1016/j.pmatsci.2017.10.001.

[31] N. Qbau, N. D. Nam, N. T. Hien, and N. X. Ca, “Development of light weight high strength aluminum alloy for selective laser melting,” *Journal of Materials Research and Technology*, vol. 9, no. 6, Nov. 2020, doi: 10.1016/j.jmrt.2020.09.088.

[32] M. Zavala-Arredondo *et al.*, “Laser diode area melting for high speed additive manufacturing of metallic components,” *Mater Des*, vol. 117, Mar. 2017, doi: 10.1016/j.matdes.2016.12.095.

[33] N. Kang, P. Coddet, L. Dembinski, H. Liao, and C. Coddet, “Microstructure and strength analysis of eutectic Al-Si alloy in-situ manufactured using selective laser melting from

elemental powder mixture," *J Alloys Compd*, vol. 691, Jan. 2017, doi: 10.1016/j.jallcom.2016.08.249.

[34] A. K. Gupta, D. J. Lloyd, and S. A. Court, "Precipitation hardening in Al–Mg–Si alloys with and without excess Si," *Materials Science and Engineering: A*, vol. 316, no. 1–2, Nov. 2001, doi: 10.1016/S0921-5093(01)01247-3.

[35] J. Lu, H. Liu, E. S. Tok, and C.-H. Sow, "Interactions between lasers and two-dimensional transition metal dichalcogenides," *Chem Soc Rev*, vol. 45, no. 9, 2016, doi: 10.1039/C5CS00553A.

[36] N. T. Aboulkhair, M. Simonelli, L. Parry, I. Ashcroft, C. Tuck, and R. Hague, "3D printing of Aluminium alloys: Additive Manufacturing of Aluminium alloys using selective laser melting," *Prog Mater Sci*, vol. 106, Dec. 2019, doi: 10.1016/j.pmatsci.2019.100578.

[37] R. Baitimerov, P. Lykov, D. Zherebtsov, L. Radionova, A. Shultc, and K. Prashanth, "Influence of Powder Characteristics on Processability of AlSi12 Alloy Fabricated by Selective Laser Melting," *Materials*, vol. 11, no. 5, May 2018, doi: 10.3390/ma11050742.

[38] A. B. Spierings, M. Voegtlin, T. Bauer, and K. Wegener, "Powder flowability characterisation methodology for powder-bed-based metal additive manufacturing," *Progress in Additive Manufacturing*, vol. 1, no. 1–2, Jun. 2016, doi: 10.1007/s40964-015-0001-4.

[39] A. Popovich and V. Sufiiarov, "Metal Powder Additive Manufacturing," in *New Trends in 3D Printing*, InTech, 2016. doi: 10.5772/63337.

[40] K. Kassym and A. Perveen, "Atomization processes of metal powders for 3D printing," *Mater Today Proc*, vol. 26, 2020, doi: 10.1016/j.matpr.2020.02.364.

[41] J. Dawes, R. Bowerman, and R. Trepleton, "Introduction to the Additive Manufacturing Powder Metallurgy Supply Chain," *Johnson Matthey Technology Review*, vol. 59, no. 3, Jul. 2015, doi: 10.1595/205651315X688686.

[42] S. Hoeges, A. Zwiren, and C. Schade, "Additive manufacturing using water atomized steel powders," *Metal Powder Report*, vol. 72, no. 2, Mar. 2017, doi: 10.1016/j.mprp.2017.01.004.

[43] L. V. M. Antony and R. G. Reddy, "Processes for production of high-purity metal powders," *JOM*, vol. 55, no. 3, Mar. 2003, doi: 10.1007/s11837-003-0153-4.

[44] S. Vock, B. Klöden, A. Kirchner, T. Weißgärber, and B. Kieback, “Powders for powder bed fusion: a review,” *Progress in Additive Manufacturing*, vol. 4, no. 4, Dec. 2019, doi: 10.1007/s40964-019-00078-6.

[45] S. E. Brika, M. Letenneur, C. A. Dion, and V. Brailovski, “Influence of particle morphology and size distribution on the powder flowability and laser powder bed fusion manufacturability of Ti-6Al-4V alloy,” *Addit Manuf*, vol. 31, Jan. 2020, doi: 10.1016/j.addma.2019.100929.

[46] L. Cordova, T. Bor, M. de Smit, M. Campos, and T. Tinga, “Measuring the spreadability of pre-treated and moisturized powders for laser powder bed fusion,” *Addit Manuf*, vol. 32, Mar. 2020, doi: 10.1016/j.addma.2020.101082.

[47] H. H. Hausner and L. A. Polytechnic Inst. of Brooklyn. Univ. of California, “FRICTION CONDITIONS IN A MASS OF METAL POWDER,” *Int. J. Powder Met., 3: No. 4, 7-13(Oct. 1967)*, 1967.

[48] A. Saker, M.-G. Cares-Pacheco, P. Marchal, and V. Falk, “Powders flowability assessment in granular compaction: What about the consistency of Hausner ratio?,” *Powder Technol*, vol. 354, Sep. 2019, doi: 10.1016/j.powtec.2019.05.032.

[49] M. A. Kaleem, M. Z. Alam, M. Khan, S. H. I. Jaffery, and B. Rashid, “An experimental investigation on accuracy of Hausner Ratio and Carr Index of powders in additive manufacturing processes,” *Metal Powder Report*, Jul. 2020, doi: 10.1016/j.mprp.2020.06.061.

[50] I. E. Anderson *et al.*, “Fundamental Progress Toward Increased Powder Yields from Gas Atomization for Additive Manufacturing,” *Advances in Powder Metallurgy and Particulate Materials-2017, Metal Powder Industries Federation, Princeton, NJ, 2017, pp. 136–146*, 2017.

[51] N. T. Aboulkhair, M. Simonelli, L. Parry, I. Ashcroft, C. Tuck, and R. Hague, “3D printing of Aluminium alloys: Additive Manufacturing of Aluminium alloys using selective laser melting,” *Prog Mater Sci*, vol. 106, Dec. 2019, doi: 10.1016/j.pmatsci.2019.100578.

[52] M. Simonelli *et al.*, “A Study on the Laser Spatter and the Oxidation Reactions During Selective Laser Melting of 316L Stainless Steel, Al-Si10-Mg, and Ti-6Al-4V,” *Metallurgical and Materials Transactions A*, vol. 46, no. 9, Sep. 2015, doi: 10.1007/s11661-015-2882-8.

[53] M. Taheri Andani, R. Dehghani, M. R. Karamooz-Ravari, R. Mirzaeifar, and J. Ni, “Spatter formation in selective laser melting process using multi-laser technology,” *Mater Des*, vol. 131, Oct. 2017, doi: 10.1016/j.matdes.2017.06.040.

[54] H. Asgari, C. Baxter, K. Hosseinkhani, and M. Mohammadi, “On microstructure and mechanical properties of additively manufactured AlSi10Mg_200C using recycled powder,” *Materials Science and Engineering: A*, vol. 707, Nov. 2017, doi: 10.1016/j.msea.2017.09.041.

[55] A. H. Maamoun, M. Elbestawi, G. K. Dosbaeva, and S. C. Veldhuis, “Thermal post-processing of AlSi10Mg parts produced by Selective Laser Melting using recycled powder,” *Addit Manuf*, vol. 21, May 2018, doi: 10.1016/j.addma.2018.03.014.

[56] H. Lee, C. H. J. Lim, M. J. Low, N. Tham, V. M. Murukeshan, and Y.-J. Kim, “Lasers in additive manufacturing: A review,” *International Journal of Precision Engineering and Manufacturing-Green Technology*, vol. 4, no. 3, Jul. 2017, doi: 10.1007/s40684-017-0037-7.

[57] J. Bedmar, A. Riquelme, P. Rodrigo, B. Torres, and J. Rams, “Comparison of Different Additive Manufacturing Methods for 316L Stainless Steel,” *Materials*, vol. 14, no. 21, Oct. 2021, doi: 10.3390/ma14216504.

[58] S. Katayama, *Handbook of Laser Welding Technologies*. Cambridge, UK: Woodhead Publishing, 2013.

[59] C. Tang, J. L. Tan, and C. H. Wong, “A numerical investigation on the physical mechanisms of single track defects in selective laser melting,” *Int J Heat Mass Transf*, vol. 126, Nov. 2018, doi: 10.1016/j.ijheatmasstransfer.2018.06.073.

[60] J. L. Tan, C. Tang, and C. H. Wong, “A Computational Study on Porosity Evolution in Parts Produced by Selective Laser Melting,” *Metallurgical and Materials Transactions A*, vol. 49, no. 8, Aug. 2018, doi: 10.1007/s11661-018-4697-x.

[61] U. Scipioni Bertoli, A. J. Wolfer, M. J. Matthews, J.-P. R. Delplanque, and J. M. Schoenung, “On the limitations of Volumetric Energy Density as a design parameter for Selective Laser Melting,” *Mater Des*, vol. 113, Jan. 2017, doi: 10.1016/j.matdes.2016.10.037.

[62] X. Tang, S. Zhang, C. Zhang, J. Chen, J. Zhang, and Y. Liu, “Optimization of laser energy density and scanning strategy on the forming quality of 24CrNiMo low alloy steel manufactured by SLM,” *Mater Charact*, vol. 170, Dec. 2020, doi: 10.1016/j.matchar.2020.110718.

[63] K. G. Prashanth, S. Scudino, T. Maity, J. Das, and J. Eckert, “Is the energy density a reliable parameter for materials synthesis by selective laser melting?,” *Mater Res Lett*, vol. 5, no. 6, Nov. 2017, doi: 10.1080/21663831.2017.1299808.

[64] Č. Donik, J. Kraner, I. Paulin, and M. Godec, “Influence of the Energy Density for Selective Laser Melting on the Microstructure and Mechanical Properties of Stainless Steel,” *Metals (Basel)*, vol. 10, no. 7, Jul. 2020, doi: 10.3390/met10070919.

[65] M. Thomas, G. J. Baxter, and I. Todd, “Normalised model-based processing diagrams for additive layer manufacture of engineering alloys,” *Acta Mater*, vol. 108, Apr. 2016, doi: 10.1016/j.actamat.2016.02.025.

[66] X. J. Wang, L. C. Zhang, M. H. Fang, and T. B. Sercombe, “The effect of atmosphere on the structure and properties of a selective laser melted Al–12Si alloy,” *Materials Science and Engineering: A*, vol. 597, Mar. 2014, doi: 10.1016/j.msea.2014.01.012.

[67] A. bin Anwar and Q.-C. Pham, “Selective laser melting of AlSi10Mg: Effects of scan direction, part placement and inert gas flow velocity on tensile strength,” *J Mater Process Technol*, vol. 240, Feb. 2017, doi: 10.1016/j.jmatprotec.2016.10.015.

[68] C. Galy, E. le Guen, E. Lacoste, and C. Arvieu, “Main defects observed in aluminum alloy parts produced by SLM: From causes to consequences,” *Addit Manuf*, vol. 22, Aug. 2018, doi: 10.1016/j.addma.2018.05.005.

[69] A. Sola and A. Nouri, “Microstructural porosity in additive manufacturing: The formation and detection of pores in metal parts fabricated by powder bed fusion,” *J Adv Manuf Process*, vol. 1, no. 3, Jul. 2019, doi: 10.1002/amp2.10021.

[70] T. Yang *et al.*, “The influence of process parameters on vertical surface roughness of the AlSi10Mg parts fabricated by selective laser melting,” *J Mater Process Technol*, vol. 266, Apr. 2019, doi: 10.1016/j.jmatprotec.2018.10.015.

[71] A. V. Gusarov and I. Smurov, “Modeling the interaction of laser radiation with powder bed at selective laser melting,” *Phys Procedia*, vol. 5, 2010, doi: 10.1016/j.phpro.2010.08.065.

[72] S. Lee, J. Peng, D. Shin, and Y. S. Choi, “Data analytics approach for melt-pool geometries in metal additive manufacturing,” *Sci Technol Adv Mater*, vol. 20, no. 1, Dec. 2019, doi: 10.1080/14686996.2019.1671140.

[73] S. A. Khairallah, A. T. Anderson, A. Rubenchik, and W. E. King, “Laser powder-bed fusion additive manufacturing: Physics of complex melt flow and formation mechanisms

of pores, spatter, and denudation zones," *Acta Mater*, vol. 108, Apr. 2016, doi: 10.1016/j.actamat.2016.02.014.

[74] D. Wang *et al.*, "Mechanisms and characteristics of spatter generation in SLM processing and its effect on the properties," *Mater Des*, vol. 117, Mar. 2017, doi: 10.1016/j.matdes.2016.12.060.

[75] W. Li *et al.*, "Effect of heat treatment on AlSi10Mg alloy fabricated by selective laser melting: Microstructure evolution, mechanical properties and fracture mechanism," *Materials Science and Engineering: A*, vol. 663, Apr. 2016, doi: 10.1016/j.msea.2016.03.088.

[76] L. Thijs, K. Kempen, J.-P. Kruth, and J. van Humbeeck, "Fine-structured aluminium products with controllable texture by selective laser melting of pre-alloyed AlSi10Mg powder," *Acta Mater*, vol. 61, no. 5, Mar. 2013, doi: 10.1016/j.actamat.2012.11.052.

[77] L. Girelli, M. Tocci, M. Gelfi, and A. Pola, "Study of heat treatment parameters for additively manufactured AlSi10Mg in comparison with corresponding cast alloy," *Materials Science and Engineering: A*, vol. 739, Jan. 2019, doi: 10.1016/j.msea.2018.10.026.

[78] M. Fousová, D. Dvorský, A. Michalcová, and D. Vojtěch, "Changes in the microstructure and mechanical properties of additively manufactured AlSi10Mg alloy after exposure to elevated temperatures," *Mater Charact*, vol. 137, Mar. 2018, doi: 10.1016/j.matchar.2018.01.028.

[79] W. J. Sames, F. A. List, S. Pannala, R. R. Dehoff, and S. S. Babu, "The metallurgy and processing science of metal additive manufacturing," *International Materials Reviews*, vol. 61, no. 5, Jul. 2016, doi: 10.1080/09506608.2015.1116649.

[80] "ASTM G1 - 03(2017) Standard Practice for Preparing, Cleaning, and Evaluating Corrosion Test Specimens".

[81] A. H. Maamoun, M. Elbestawi, G. K. Dosbaeva, and S. C. Veldhuis, "Thermal post-processing of AlSi10Mg parts produced by Selective Laser Melting using recycled powder," *Addit Manuf*, vol. 21, May 2018, doi: 10.1016/j.addma.2018.03.014.

[82] P. Mercelis and J. Kruth, "Residual stresses in selective laser sintering and selective laser melting," *Rapid Prototyp J*, vol. 12, no. 5, Oct. 2006, doi: 10.1108/13552540610707013.

[83] A. Salmi, E. Atzeni, L. Iuliano, and M. Galati, “Experimental Analysis of Residual Stresses on AlSi10Mg Parts Produced by Means of Selective Laser Melting (SLM),” *Procedia CIRP*, vol. 62, 2017, doi: 10.1016/j.procir.2016.06.030.

[84] L. Papadakis, A. Loizou, J. Risse, and J. Schrage, “Numerical Computation of Component Shape Distortion Manufactured by Selective Laser Melting,” *Procedia CIRP*, vol. 18, 2014, doi: 10.1016/j.procir.2014.06.113.

[85] D. Buchbinder, W. Meiners, N. Pirch, K. Wissenbach, and J. Schrage, “Investigation on reducing distortion by preheating during manufacture of aluminum components using selective laser melting,” *J Laser Appl*, vol. 26, no. 1, Feb. 2014, doi: 10.2351/1.4828755.

[86] M. F. Zaeh and G. Branner, “Investigations on residual stresses and deformations in selective laser melting,” *Production Engineering*, vol. 4, no. 1, Feb. 2010, doi: 10.1007/s11740-009-0192-y.

[87] Mugwagwa, Yadroitsev, and Matope, “Effect of Process Parameters on Residual Stresses, Distortions, and Porosity in Selective Laser Melting of Maraging Steel 300,” *Metals (Basel)*, vol. 9, no. 10, Sep. 2019, doi: 10.3390/met9101042.

[88] B. Amir, E. Grinberg, Y. Gale, O. Sadot, and S. Samuha, “Influences of platform heating and post-processing stress relief treatment on the mechanical properties and microstructure of selective-laser-melted AlSi10Mg alloys,” *Materials Science and Engineering: A*, vol. 822, Aug. 2021, doi: 10.1016/j.msea.2021.141612.

[89] VDMA, Ed., *Analytical Strength Assessment of Components - FKM Guidelines*, 6th ed. 2012.

[90] S. Romano, A. Brückner-Foit, A. Brandão, J. Gumpinger, T. Ghidini, and S. Beretta, “Fatigue properties of AlSi10Mg obtained by additive manufacturing: Defect-based modelling and prediction of fatigue strength,” *Eng Fract Mech*, vol. 187, Jan. 2018, doi: 10.1016/j.engfracmech.2017.11.002.

[91] S. Defanti, C. Cappelletti, A. Gatto, E. Tognoli, and F. Fabbri, “Boosting Productivity of Laser Powder Bed Fusion for AlSi10Mg,” *Journal of Manufacturing and Materials Processing*, vol. 6, no. 5, Sep. 2022, doi: 10.3390/jmmp6050112.

[92] D. S. Thomas and S. W. Gilbert, “Costs and Cost Effectiveness of Additive Manufacturing,” Gaithersburg, MD, Dec. 2014. doi: 10.6028/NIST.SP.1176.

[93] C. Lindemann, J. Ulrich, and M. Moi, “Analyzing Product Lifecycle Costs for a Better Understanding of Cost Drivers in Additive Manufacturing,” in *Solid Freeform Fabrication Symposium - An Additive Manufacturing Conference*, 2012.

[94] W. Yu, S. L. Sing, C. K. Chua, and X. Tian, “Influence of re-melting on surface roughness and porosity of AlSi10Mg parts fabricated by selective laser melting,” *J Alloys Compd*, vol. 792, pp. 574–581, Jul. 2019, doi: 10.1016/j.jallcom.2019.04.017.

[95] E. Stugelmayer, “Digital Commons @ Montana Tech CHARACTERIZATION OF PROCESS INDUCED DEFECTS IN LASER POWDER BED FUSION PROCESSED ALSI10MG ALLOY CORE View metadata, citation and similar papers at core.ac.uk provided by Digital Commons @ Montana Tech.” [Online]. Available: https://digitalcommons.mtech.edu/grad_rsch

[96] W. E. King *et al.*, “Observation of keyhole-mode laser melting in laser powder-bed fusion additive manufacturing,” *J Mater Process Technol*, vol. 214, no. 12, pp. 2915–2925, 2014, doi: 10.1016/j.jmatprotec.2014.06.005.

[97] N. T. Aboulkhair, N. M. Everitt, I. Ashcroft, and C. Tuck, “Reducing porosity in AlSi10Mg parts processed by selective laser melting,” *Addit Manuf*, vol. 1, pp. 77–86, Oct. 2014, doi: 10.1016/j.addma.2014.08.001.

[98] L. Thijs, K. Kempen, J. P. Kruth, and J. van Humbeeck, “Fine-structured aluminium products with controllable texture by selective laser melting of pre-alloyed AlSi10Mg powder,” *Acta Mater*, vol. 61, no. 5, pp. 1809–1819, Mar. 2013, doi: 10.1016/j.actamat.2012.11.052.

[99] N. T. Aboulkhair, I. Maskery, C. Tuck, I. Ashcroft, and N. M. Everitt, “The microstructure and mechanical properties of selectively laser melted AlSi10Mg: The effect of a conventional T6-like heat treatment,” *Materials Science and Engineering A*, vol. 667, pp. 139–146, Jun. 2016, doi: 10.1016/j.msea.2016.04.092.

[100] N. Read, W. Wang, K. Essa, and M. M. Attallah, “Selective laser melting of AlSi10Mg alloy: Process optimisation and mechanical properties development,” *Mater Des*, vol. 65, pp. 417–424, Jan. 2015, doi: 10.1016/j.matdes.2014.09.044.

[101] M. Giovagnoli, G. Silvi, M. Merlin, and M. T. di Giovanni, “Optimisation of process parameters for an additively manufactured AlSi10Mg alloy: Limitations of the energy density-based approach on porosity and mechanical properties estimation,” *Materials Science and Engineering A*, vol. 802, Jan. 2021, doi: 10.1016/j.msea.2020.140613.

[102] X. Gu, J. Zhang, X. Fan, N. Dai, Y. Xiao, and L.-C. Zhang, “Abnormal corrosion behavior of selective laser melted AlSi10Mg alloy induced by heat treatment at 300 °C,” *J Alloys Compd*, vol. 803, Sep. 2019, doi: 10.1016/j.jallcom.2019.06.274.

[103] Y. Yang *et al.*, “Improved corrosion behavior of ultrafine-grained eutectic Al-12Si alloy produced by selective laser melting,” *Mater Des*, vol. 146, May 2018, doi: 10.1016/j.matdes.2018.03.025.

[104] K. G. Prashanth *et al.*, “Tribological and corrosion properties of Al–12Si produced by selective laser melting,” *J Mater Res*, vol. 29, no. 17, Sep. 2014, doi: 10.1557/jmr.2014.133.

[105] P. Fathi, M. Mohammadi, X. Duan, and A. M. Nasiri, “A comparative study on corrosion and microstructure of direct metal laser sintered AlSi10Mg_200C and die cast A360.1 aluminum,” *J Mater Process Technol*, vol. 259, Sep. 2018, doi: 10.1016/j.jmatprotec.2018.04.013.

[106] A. Leon and E. Aghion, “Effect of surface roughness on corrosion fatigue performance of AlSi10Mg alloy produced by Selective Laser Melting (SLM),” *Mater Charact*, vol. 131, Sep. 2017, doi: 10.1016/j.matchar.2017.06.029.

[107] G. Sander *et al.*, “Corrosion of Additively Manufactured Alloys: A Review,” *CORROSION*, vol. 74, no. 12, Dec. 2018, doi: 10.5006/2926.

[108] A. Leon and E. Aghion, “Effect of surface roughness on corrosion fatigue performance of AlSi10Mg alloy produced by Selective Laser Melting (SLM),” *Mater Charact*, vol. 131, Sep. 2017, doi: 10.1016/j.matchar.2017.06.029.

[109] “Corrosion resistance tables, metald, plastic, nonmetallics, and rubber / Philip A. Schweitzer / Marcel Decker Inc. / 1976”.